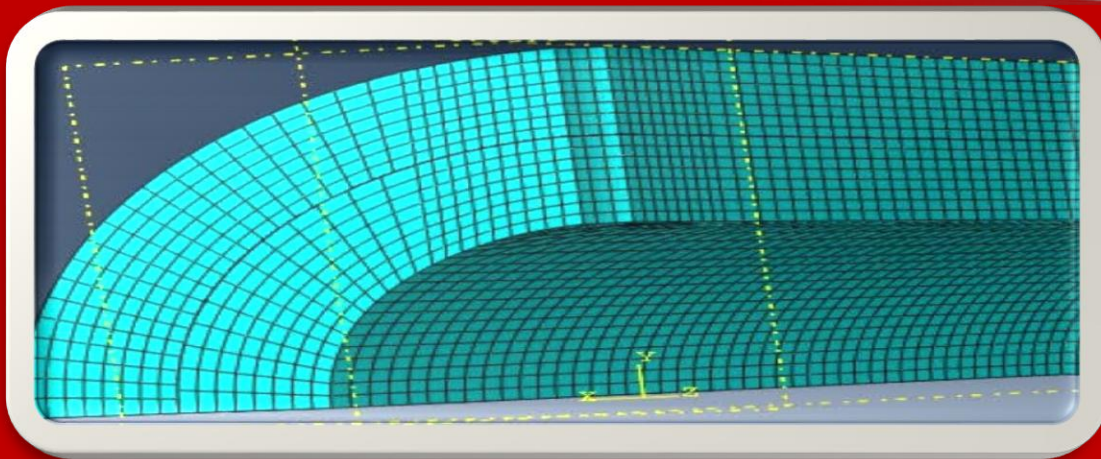
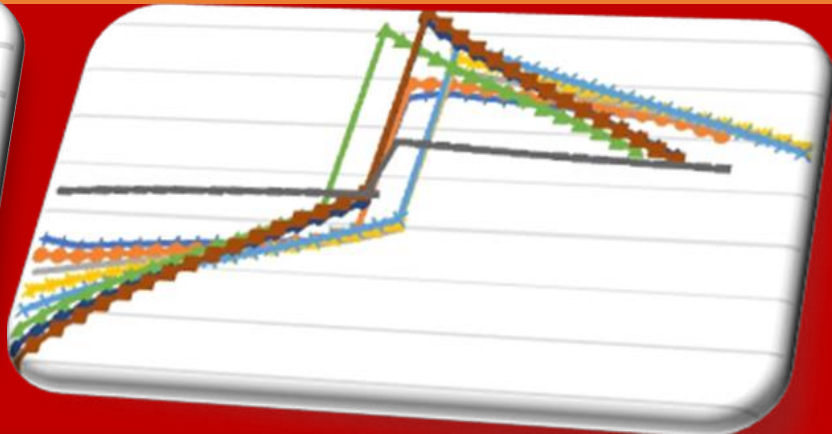
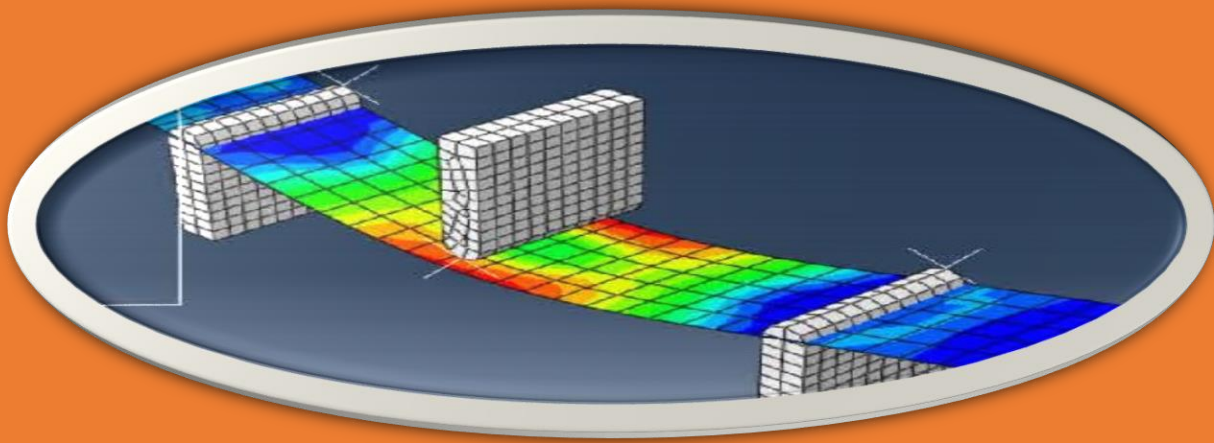




African Journal of Engineering Research and Innovation

AJERI Vol 1. No. 3. 2023



The Institution of Engineers of Kenya

ISSN: 2957- 7780

In partnership with



AJERI

African Journal of Engineering in Research and Innovation

ISSN: 2957- 7780

Volume 1. No 3. 2023

IEK

Published by:

The Institution of Engineers of Kenya

P.O Box 41346- 00100

City Square Nairobi Kenya

Tel: +254 (20) 2729326, 0721 729363, (020) 2716922

Email: editor@iekenya.org

Website: www.iekenya.org

African Journal of Engineering Research and Innovation (AJERI), is published by **The Institution of Engineers of Kenya, IEK**, as an international forum for publication of high-quality papers in all areas of Engineering

CONTENTS

Pages

Cost-Effective Telecommunication Technologies for Rural Areas in Developing Countries: A Case Study of South Africa	6
---	---

Marcel Ohanga Odhiambo, Weston Mwashita

Optimal Angel and Shell Layers of Overwrapped Composite High-Pressure Vessels: A review of previous studies on composite pressure influenced by angle and shell thickness	16
---	----

Nathan Numbi Mukala, Leonard M Masu, Patrick K Nziu

Investigating Effects of Preparation Parameters on Mechanical Performance of PBAC2-co-PM52 Copolyoxamide/Carbon Fiber Reinforced Composites	39
---	----

Fredrick Nzioka Mutua, and Yong He

Optimal shell thickness for Overwrapped Composite High-Pressure Vessels	54
---	----

Nathan Numbi Mukala, Leonard M Masu, Patrick K Nziu

Hybrid Modulation Scheme for System Performance Evaluation and Energy Efficiency Measurement in 5G Technology.....	81
--	----

Bertille Auyane Ngouessy ep Ovono, Temidayo Otunniyi , Marcel O Odhiambo

Cost-Effective Telecommunication Technologies for Rural Areas in Developing Countries: A Case Study of South Africa

Marcel Ohanga Odhiambo

Mangosuthu University of Technology, Durban, South Africa, ohanga.marcel@mut.ac.za

Weston Mwashita

*International University of Management, Windhoek, Namibia,
westonmwashita@gmail.com*

Abstract

Rural South Africa has always been underserved in terms of telecommunications services. For numerous reasons, this condition has persisted into the era of broadband connectivity. Market failure, the slow pace of implementing SA Connect (the national broadband policy adopted by Cabinet in 2013), the splitting of the old Department of Communications, and a period of political leadership changes may all be blamed for the problem, despite the National Development Plan's vision of a "dynamic and connected vibrant information society and a knowledge economy that is more inclusive, equitable, and prosperous." Poverty, inequality, and unemployment continue to be a harsh reality for the rural poor. To address all aspects of the digital ecosystem, not only access, decisive and holistic initiatives are required. The scenario necessitates stakeholders rethinking how the digital divide might be bridged. From a policy and regulatory standpoint, it necessitates novel approaches and creative thinking. Despite persistent policy efforts to address these obstacles, South African rural areas remain excluded from the digital communication podia, resulting in digital inequality. This report attempts to address telecommunication system penetration in South African rural areas by utilising 5G and infrastructure sharing. This paper aims at reviewing appropriate and cost-effective telecommunication technologies for rural areas in developing countries with particular emphasis on South Africa. Nevertheless, the identified technologies are applicable to rural areas in the developing countries.

Keywords: digital divide, telecommunications infrastructure, telecommunications deployment, online education, 5G rural area deployment.

1. Introduction

South Africa's government recently reaffirmed its commitment to economic black empowerment. Given that the majority of black South Africans live in rural areas that are more often remote from the country's economic centers, one of the first steps toward black empowerment is the establishment of the necessary technological infrastructure that can be used to facilitate technological and economic development. This, in turn, will lead to opportunities for black empowerment in rural areas. This technology foundation, in the form of telecommunications and energy, will also serve the education sector in remote rural areas. [1]. Significant in isolated rural areas, on the other hand, may cause congestion in the available telecommunications infrastructure. As a result, it is critical that telecommunications and computer networks be properly built and capable of supporting rapid future technological progress in these fields. [2] states that even some of the world's wealthiest and most technologically advanced countries were unprepared and ill-equipped for a true crisis, as demonstrated by the recent Covid-19 outbreak. In Somalia, for example, Somalia with limited fixed line telecommunications infrastructure and an increasingly cashless economic, mobile telecommunications services enabled the society to function essentially, as it did prior to the pandemic. Market vendors, for example, have had no trouble completing their tasks via the Internet. Other African countries can learn from Somalia's example. Indeed, once the crisis is over,

telecommunications can play an important role in assisting and rebuilding African economies. Small businesses that use mobile money services save money, are less vulnerable to theft and fraud, and have easier access to new markets. Other developing countries could leverage mobile telecommunication services to run and manage business. Mobile telecommunications services have made it possible for far-flung rural areas of the developing countries like South Africa, Kenya etc. to be reachable and meaningful communications to take place. From the comfort anywhere in the world, I can reach folks in my rural area/home and talk to my mum, a feat that was not possible prior to the 1980s. All this is due to mobile telecommunication technologies.

2. TELECOMS IN SA RURAL AREA

It is always difficult to provide rapid development of telecommunication networks in remote rural areas due to the current reliance on legacy fixed telecommunications facilities and older generation of mobile services due to the high cost of infrastructure and deployment. Alternative technologies should be investigated. Wireless networks could be an alternative technology for supporting rapid network expansion in rural areas. The use of new technologies such as wireless networks raises new issues in network analysis, modelling, routing, and scheduling for the purpose of Quality of Service (QoS) provisioning. This study aims at developing a selection criteria for telecommunication networks aimed at rural populations, with a particular emphasis on network quality of service. Wireless networks have the advantage of not necessitating the large infrastructure investments required by wired networks, making the market more accessible to smaller businesses. Because of this, large organizations and customers will find it easier to transition to wireless items. Wireless technologies also make it easier to connect to the Internet in places where wired technology was previously unavailable. Facebook, Google, and SpaceX have all begun efforts toward this goal. Facebook is experimenting with high-altitude drones to provide Internet access to people on the ground below. Similarly, Google used weather balloons, and SpaceX is developing small, low-orbiting satellites that could be used to provide Internet in rural areas. Space Exploration Technologies Corp., doing business as SpaceX, is an American spacecraft manufacturer, launch service provider and satellite communications company headquartered in Hawthorne, California. The company was founded in 2002 by Elon Musk with the goal of reducing space transportation costs and to colonize Mars. The company manufactures the Falcon 9, Falcon Heavy and Starship heavy-lift launch vehicles, the Cargo Dragon and Crew Dragon spacecraft, the Starlink mega-constellation satellite and rocket engines [3].

The company offers commercial satellite-based internet service via its constellation of Starlink satellites, which became the largest-ever satellite constellation in January 2020 and as of June 2023 comprised more than 4,300 small satellites in orbit.

3. NETWORK TECHNOLOGIES

The two primary groups of communications technologies are fixed wired networks and wireless networks. A copper, coaxial, or fibre cable is a communication medium that is strung between communicative parties and supports information exchange in fixed wired networks. Wireless networks, on the other hand, use radio waves as a communication medium to allow communicating parties to exchange data. The radio waves as specified by the radio spectrum is the part of the electromagnetic spectrum with frequencies from 3 Hz to 3,000 GHz (3 THz). Electromagnetic waves in this frequency range, called radio waves, are widely used in modern technology, particularly in telecommunication. To prevent interference between different users, the generation and transmission of radio waves is strictly regulated by national laws, coordinated by an international body, the International Telecommunication Union (ITU [4]. Radio waves are a type of electromagnetic radiation with the longest wavelengths in the electromagnetic spectrum, typically with

frequencies of 300 gigahertz (GHz) and below.[citation needed] At 300 GHz, the corresponding wavelength is 1mm, which is shorter than the diameter of a grain of rice. At 30 Hz the corresponding wavelength is ~10,000 kilometres (6,200 miles), which is longer than the radius of the Earth. Wavelength of a radio wave is inversely proportional to its frequency, because its velocity is constant. Like all electromagnetic waves, radio waves in a vacuum travel at the speed of light, and in the Earth's atmosphere at a slightly slower speed [5]. Wireless networks are classified into three types: radio (cellular), satellite, and infrared systems. [6] Historically, radio waves (microwaves) were used to connect distant locations for information exchange. Radio waves enable direct point-to-point communication. Satellites act as a communication link between parties on the ground. There is no direct communication between communication parties; instead, an indirect link exists between the earth station and the satellite, and then to another earth station in another part of the world. Infrared technology is used in a wide range of household and entertainment products. Nonetheless, infrared and WiFi are emerging as communication mediums for transferring data over short distances between devices.

Fixed cable technology, while providing superior performance (transmission rates, error rates, capacity, and so on) to wireless technology, is not appropriate for rapid expansion of communications networks in remote rural areas due to the high deployment costs. Ad Hoc networks, on the other hand, may be incapable of providing all of the communication services required in a specific rural location. A strong combination of fixed wired and wireless technologies could provide an alternative solution for rapid telecommunication network expansion in remote rural areas for developing countries.

4. WIRELESS NETWORKS

Wireless networks are computer networks that communicate using radio frequency as the physical channel. Each node in the network transmits data that all nodes within its immediate transmission range can receive. Nodes do not need to be physically attached to any network because they broadcast and receive data over the air. As a result, such networks provide data connectivity as well as user mobility. Both portable and mobile terminals are used for communication in wireless networks, and while mobile terminals can move from one location to another, portable terminals can only be accessed while they are stationary. When mobile terminals are in motion, they can be accessed. Wireless networks are characterized by the following differences from the wired networks:

- Address is not equivalent to physical location – in a wireless network, the address refers to a particular station and this station need not be stationary. Therefore, address may not refer to a particular geographical location.
- Dynamic topology and restricted connectivity – the mobile nodes may often go out of range of each other. This means that network connectivity is partial at times.
- Medium boundaries are not well defined – the exact reach of wireless signals cannot be determined accurately. It depends on various factors such as signal strength and noise levels. This means that the precise boundaries of the medium cannot be determined easily.
- Error prone medium – transmission by nodes in the wireless channel are affected by simultaneous transmission of neighbouring nodes that are located within the direct transmission range of the transmitting node. This means that the error rates are significantly higher in the wireless medium. Typical bit error rates (fractions of bits that are received in error) are of the order of 10^{-4} in a wireless channel as against 10^{-9} in fibre optic cables.

Wireless networks, considering network formation and architecture, can broadly be classified into two types, infrastructure, and Ad Hoc networks (infrastructure less) [7].

A. Infrastructure Networks

Access Points (APs) are special nodes in infrastructure-based networks that are connected via existing wired networks. In the sense that they can communicate with both wireless nodes and existing wired networks, APs are unique. APs are used to communicate with the other wireless nodes, also known as Mobile Stations (STAs). The APs can also connect to other networks. Infrastructure-based networking is a network with pre-built infrastructure consisting of fixed and wired network nodes and gateways, with network services typically offered through these pre-built infrastructures. Cellular networks, for example, are infrastructure-based networks made up of backbone switches from the Public Switched Telephone Network (PSTN), Mobile Switching Centres, base stations, and mobile hosts. Each node in the network has a specified role to play, and connections follow a rigorous signalling sequence among the nodes.

B. Infrastructureless (Ad Hoc) Networks

There is no fixed infrastructure required for ad hoc networks. These networks can be activated at any time and in any location. Nodes connect with one another directly or send messages to other nodes that are directly accessible. A network is built dynamically in this situation by the cooperation of an arbitrary number of independent nodes. The role that each node should play is not predetermined. Rather than relying on pre-existing network architecture, each node makes its own decisions based on the network condition. Two PCs with wireless adapter cards, for example, can create their own network whenever they are in range of one another. Nodes in mobile ad hoc networks are expected to act as routers, participating in the discovery and maintenance of routes to other nodes.

The communications systems designer needs to understand the different technologies before making an informed choice of the most suitable technology for deployment in rural areas.

5. RADIO PROPAGATION MECHANISMS

In wireless propagation, radio waves are used as the transmission medium. Radio waves suffer varying forms of interference. The interferences may at times cause degradation or total loss of signal/message carried by the transmission medium. It is therefore incumbent upon the radio communication systems designer to ensure that the radio waves are not adversely affected by the interferences thus, creating a poor communication path between transmitter and receiver. The three radio wave propagation interferences that are mostly experienced in a communication path as are:

A. Reflection

Reflection occurs when a propagation radio wave collides with an object much larger than its wavelength (such as the earth's surface or tall structures), causing the wave to be reflected back to the source. The incident and reflected waves have a 180-degree phase shift as a result of reflection.

B. Diffraction

This propagation occurs when a wave collides with an impenetrable object. The wave bends along the boundaries of the object, causing it to propagate in various directions. The wavelength of the diffracted wave is comparable to the diameter of the diffraction-causing item. The bending allows the wave to reach regions behind the object that would otherwise be inaccessible via line-of-sight transmission. The amount of diffraction is proportional to the frequency, with lower frequencies diffracting more.

C. Scattering

Scattering occurs when a wave travels through a medium containing several objects with dimensions smaller than the wavelength. The wave breaks up into several weaker outgoing signals. In practice, objects such as street signs, lampposts, and greenery cause scattering.

Figure 1 depicts the various propagation mechanisms that radio waves encounter during propagation [8]. At the receiver, the received power is generally less than the transmitted power. The loss of the signal power is known as attenuation. The three forms interferences hereabove reviewed may cause interference with the main beam thus causing signal degradation at the receiver.

The interferences are caused by physical structures such as tall trees, buildings etc. the communication path be designed to as much as possible to avoid these structures. The communication path should be selected to at least avoid these obstacles.

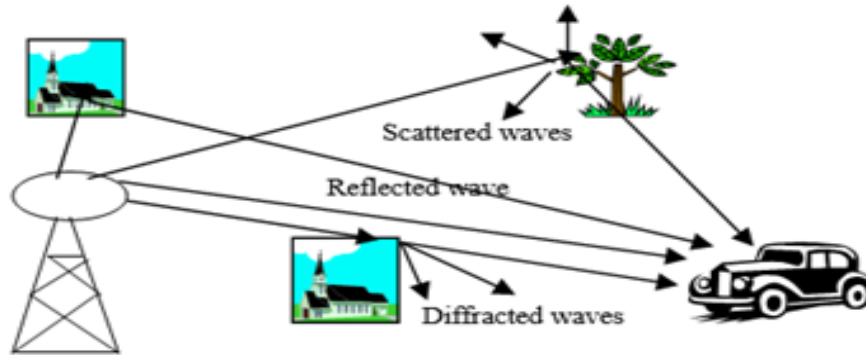


Figure 1: Radio wave propagation mechanisms

6. CHARACTERISTICS OF THE WIRELESS CHANNEL

The wireless channel (transmission medium) is vulnerable to a wide range of transmission impediments, including path loss, interference, and blockage. These factors limit the wireless transmission's range, data rate, and reliability. The extent to which these factors influence transmission is determined by environmental conditions as well as the mobility of the transmitter and receiver [9]. The transmitted signal typically contains a direct-path component between the transmitter and receiver. Other components of the transmitted signal, known as multipath components, are reflected, diffracted, and scattered by the environment, arriving at the receiver with shifted amplitude, frequency, and phase in comparison to the direct-path component. The communication systems designer should be aware of these wireless channel characteristics so as to be able to mitigate for them by introducing line amplifiers, filters, etc. along the communication path to ensure appropriate signal levels reach the receiver. These characteristics are as follows:

A. Path loss

Path loss is defined as the ratio of the power of the transmitted signal to the power of the same signal received at the receiver. It is determined by the propagation distance. Path loss estimation is critical for designing and deploying wireless communication networks. Path loss is also affected by several factors, including the radio frequency used and the terrain. Because several of these factors (particularly terrain) cannot be the same everywhere, a single model may be insufficient to describe the characteristics of every transmission. As a result, several models are required when designing a network to describe the various transmission environments.

The free space propagation model is the most basic path loss model, with a direct-path signal between the transmitter and receiver and no atmospheric attenuation or multipath components. The relationship between the transmitted power P_t and the received power P_r in this model is given by:

$$P_r = P_t G_t G_r \left(\frac{\lambda}{4\pi d} \right)^2 \quad [1]$$

Where G_t and G_r are the transmitter and receiver antenna gains, respectively, in the direction from transmitter to the receiver, d is the distance between the transmitter and receiver,

$$\lambda = c / f \quad [2]$$

and is the wavelength of the signal. Realistic path loss models that consider the propagation effects in specific environments can be obtained by solving Maxwell's equations.

The two-ray or two-path model is another popular path loss model. The free space model assumes a single path from transmitter to receiver. However, the signal travels through several channels before reaching the receiver (because of reflection, diffraction or refraction and scattering). This phenomenon is attempted to be captured by the two-way path model. The model assumes that the signal arrives at the receiver via two paths, one direct and the other through which a reflected, refracted, or scattered wave is received.

B. Fading

The fluctuation of signal strength when received at the receiver is referred to as fading. Fast fading/small-scale fading and slow fading/large-scale fading are the two types of fading. Fast fading describes the rapid changes in the amplitude, phase, or multi-path delays of a received signal caused by interference between multiple versions (copies) of the same transmitted signal arriving at the receiver at slightly different times. The time between receiving the first version of the signal and receiving the last echoed signal is referred to as delay spread. The propagation mechanisms, namely reflection, diffraction, and scattering, cause multipath propagation of the transmitted signal, which causes fast fading. Slow fading occurs when objects between the transmitter and receiver partially absorb the transmission. Slow fading is so named because the duration of the fade can range from seconds to minutes. Slow fading can happen when the receiver is inside a building and the radio waves must pass through the walls, or when the receiver is temporarily shielded from the transmitter by a building. The obstructing objects cause a random variation in the power of the received signal. Slow fading can cause the received signal power to fluctuate even when the distance between the transmitter and receiver remains constant.

C. Interference

Wireless transmissions mitigate interference from a wide range of sources. There are two types of interference: adjacent channel interference and co-channel interference. In the case of adjacent channel interference, signals in nearby frequencies have components that are outside their allocated ranges, and these components may interfere with ongoing transmissions in the adjacent frequencies. It can be avoided by carefully introducing guard bands between allocated frequency ranges. Co-channel interference, also known as narrow-band interference, is caused by other nearby systems (such as AM/FM broadcasts) using the same frequency.

Inter-symbol interference is another type of interference in which the received signal is distorted due to temporal spreading and the overlapping of individual pulses in the signal. When the temporal spreading of individual pulses (delay spread) exceeds a certain limit (symbol detection time), the receiver is unable to reliably distinguish between changes in state in the signal, i.e. the bit pattern interpreted by the receiver differs from that sent by the sender. The most commonly used technique for dealing with inter-symbol interference is adaptive equalization. Adaptive equalization entails mechanisms that collect dispersed symbol energy and return it to its original time interval.

D. Doppler shift

The Doppler shift is defined as a change/shift in the frequency of the received signal when the transmitter and receiver are mobile with respect to each other. If they are moving in the same direction, the frequency of the received signal will be higher than the frequency of the transmitted signal, and if they are moving in opposite directions, the frequency of the signal at the receiver will be lower than the frequency of the signal at the transmitter. The Doppler shift's f_d is given by:

$$f_d = \frac{v}{\lambda} \quad [3]$$

Where v is the relative velocity between the transmitter and receiver and λ is the wavelength of the signal.

7. COMMUNICATION-BASED APPLICATIONS

A wide range of actors, including public telecommunications operators, are designing and implementing communication-based applications in rural South Africa (PTOs). Professional, academic, business, and agricultural sectors, among others, provide a significant portion of the expertise required to develop sustainable, connectivity-enabled applications for rural areas. Schools, universities, government departments, international organizations, and non-governmental organizations (NGOs) not only routinely design and implement customized applications, but they also independently purchase and set up information technology (IT) equipment. As a result, public telecommunications operators are increasingly being asked to support a diverse set of networks, protocols, and bandwidth requirements outside of urban areas.

Basic literacy, computer skills, and training in the use of ICT applications continue to be significant challenges in rural areas. Language barriers and the complexity of PC operation have been shown to impede Internet adoption. Many novel schemes have been developed in rural areas to overcome these obstacles. Although they are not widely used, techniques such as voice mail, content translation, and icon-based telephones show that foreign languages and illiteracy are not necessarily barriers to using communications services if the end user's needs are understood and addressed. The importance of relevant content in any rural application cannot be overstated.

8. TECHNOLOGIES FOR THE RURAL SOUTH AFRICA

Problems with wire plant installation and maintenance have led to the widespread use of wireless systems in rural areas. Through case studies and ITU activities, nine types of wireless access systems were identified, illustrating existing and emerging access options for reaching rural communities. Given the trend toward shared facilities such as tele centers, university extension centers, post office kiosks, and so on, as well as the variety of revenue models associated with social services in the health, educational, and e-commerce fields, the focus group looked at technologies that increased the number of supportable applications while also demonstrating lower per-line costs.

9. BRIDGING THE DIGITAL DIVIDE

The rural connectivity divide was highlighted when schools were forced to close due to the pandemic. When teaching went virtual, many children from underserved neighbourhoods across the country had no access to broadband at home. Even though both urban and rural districts adopted at-home learning, city officials were more likely to provide students with Wi-Fi hotspots and equipment so they could continue their studies. According to one study, such initiatives were less widespread in rural areas. A lack of digital

infrastructure is at least part of the cause. Because of COVID-19, President Ramaphosa declared South Africa to be in an alert level 4 in March 2020. As a result, schools and tertiary institutions were closed for most of the year, thus halting all teaching and learning for many youngsters. However, traditionally white, and private schools swiftly moved their teaching and learning to an online platform, where pupils learned using cell phones, tablets, and computers connected to the internet. This was simple because they had access to the necessary technology as well as the cash to put it to use. According to [6], online learning is nearly impossible for rural and underprivileged pupils, and it surely does not achieve educational equality. The impact of COVID-19 on education, as well as the inability of poor and rural pupils to access online learning, has just confirmed the adage that the poor get poorer while the wealthy grow [10]

10. 5G COMING TO THE RESCUE OF SOUTH AFRICAN RURAL AREAS

Because 5G uses more radio spectrum than previous generations, it will be able to deliver broadband to individuals living in sparsely populated areas. At the upper end of that spectrum, users will be able to download at least 1 gigabit per second, which is fast enough to transport a 500-megabyte video in a matter of seconds. However, because that high-end signal can only reach short distances, users will need to be less than a mile away. Carriers would not be able to make such a large investment in locations where people live far apart. However, 5G networks can utilise radio waves in the low band, which were formerly used by TV channels. Customers can connect to towers thousands of kilometres away using low-band 5G, which can't transfer data at the same pace as high-band airwaves. Data can travel at speeds up to several times faster than 4G in this frequency range, but it also means that people in remote areas who previously couldn't get 4G may suddenly have access to reliable, fast mobile broadband. The low band has the extra benefit of being able to penetrate windows and walls, allowing it to reach deeper into structures than ever before.

Investing in 5G technology for both wireless and fixed networks is necessary to effectively develop a rural network that allows all individuals to participate in the digital economy. With faster speeds, greater coverage regions, and improved security over prior 4G networks, the 5G standard enables a broader range of use cases than ever before.

However, it is pointless to construct this new network if people cannot afford it. That's when the clever edge comes into play. It brings real-time processing capability closer to the point of generation, making deployments easier and operating costs lower. When 5G and the intelligent edge are combined, the same workload performance may be achieved with less overhead, resulting in significant cost savings. And, when it comes to constructing the intelligent rural network, keeping prices low will be critical to making it affordable to everybody.

RAN (Radio Network Access) is a network's "last mile," the visible link between the network and a mobile phone. Operators are attempting to open up RAN standards and eliminate reliance on single-vendor systems. Large operators like Orange, Vodafone, and MTN are already intending to deploy virtual (vRAN) and Open RAN to expand their coverage into new markets since it gives equipment providers more options, lowers TCO, and makes it easier to replace portions as needed.

Open RAN allows CSPs to choose the best technical solutions for the scenario rather than being confined to single-vendor options, which is important in rural networks where cost is a big factor in installing new networks or upgrading old ones. When it comes to rural connectivity, Open RAN and 5G make for a powerful combination. The costs of setting up networks over a vast geographic area have been

demonstrated in previous initiatives. To reduce costs, intelligent rural networks can take advantage of powerful new technology such as distributed clouds and edge computing.

Rural networks will also necessitate remote management and monitoring on a huge scale. As part of the network design and implementation, end-to-end automation and AI-based analytics can help to reduce ongoing expenses and keep networks up and running efficiently. Because of the enormous geographic areas involved, these management and monitoring systems must also be able to work remotely so that technical employees can respond swiftly to any difficulties that develop.

Transmission at long-range, low-bandwidth frequencies, or what are known as the low and mid bands, will be a more practical 5G deployment for rural areas (when it happens) (600 MHz to 900 MHz and 2.5 GHz to 4.2 GHz, respectively). Because transmissions can travel a few miles, fewer cell towers will be required. Of course, this will result in lesser data speeds (usually around 250+ Mbps) than the gigabit rates possible with mmWave in metropolitan areas. Despite this, speeds will be faster than LTE.

Precision agriculture, which uses technology on farm equipment, GPS systems, artificial intelligence, and real-time data collection to guide a variety of activities, can benefit from 5G in rural areas. Sensors monitor plant water and soil conditions, as well as crop health. Imagery can help with crop placement and decision-making. This can significantly increase crop yields while reducing water, pesticide, and fertilizer use.

These capabilities can be automated using IoT (Internet of Things) applications and mobile-edge computing, both of which occur locally and in real-time.

Telemedicine in rural areas, where access to health care is either unavailable or has declined in recent years, is another application in high demand. For example, residents with mental health issues in these communities frequently struggle to obtain treatment from qualified professionals. Broadband telehealth will assist in addressing this challenge and improving people's health and quality of life.

Education efforts will also benefit when teachers can connect with children in remote areas who do not currently have equal learning opportunities as their urban counterparts. Travelers who want seamless coverage while they work, roam, and wander have a strong appetite for connectivity. Satellite not only fills gaps in terrestrial coverage, but it is also critical for connectivity in sparsely populated rural areas—as well as for innovations like self-driving cars.

11. INFRASTRUCTURE SHARING IN THE RURAL AREAS

The government of South Africa could provide subsidies to operators who build infrastructure in rural areas. These could take the form of tax breaks to entice operators to expand their networks into marginally profitable areas. Formulating national broadband aspirations and developing a national plan is a key first step for South Africa. After the national objectives have been established, the government can create a national roadmap outlining how they plan to achieve their aim. The government has several levers at its disposal, including policy, legislation, and regulation, to influence supply and demand issues.

12. CONCLUSION

Broadband connectivity is often unavailable for persons living in rural areas of South Africa. This makes digital transformation more difficult and may have a negative influence on local communities' socioeconomic development. The South African government should make a commitment to rectifying this situation by ensuring that as many people as possible in rural areas have access to the Internet and bridging

the digital gap. 5G has the potential to revolutionize a variety of industries, but there are still a lot of difficulties to be resolved and significant investments to be required if 5G is to become widely available. Additional datacentres and Internet exchange points could be a solution, but such decisions must be made based on economic viability and customer demand for such assets.

Telecommunication systems/channels experiences several disturbances which may result in the degradation of the services. Section IV provided a brief overview of wireless networks as an attempt to help the user to understanding the technology being proposed for rapid deployment of telecommunication services in rural areas of South Africa or developing countries. Based on cost implications, wireless networks present a better option as proven by the wide distribution of mobile communication networks in many developing countries.

Sections V and VI presented technical issues that the telecommunication systems designer should consider when installing telecommunication networks. The technical issues may adversely affect the smooth operations of the network thus, requires planning and ways/means of mitigating them.

This work was not carried out in a typical research format of 1. Identify a problem, 2. Carry out literature review and propose a solution, 3. Implement and test the solution, 4. Collect and analyse the results, 5. Make a conclusion. It was conducted as a review of available technologies and to come up with a cost-effective telecommunication technology for rapid deployment of telecommunication services in rural areas of South Africa to address the low penetration of telecommunications services.

REFERENCES

- [1] S. Pather and C. Rey-Moreno, "Advancing rural connectivity in South Africa A case for community-owned networks," Department of Science and Technology, South Africa, pp. 1-25, Jun. 2019.
- [2] Capacity Daily, "Telecoms is the key to growing African economies post-Covid, Aug. 2020.
- [3] <https://en.wikipedia.org/wiki/SpaceX>
- [4] ITU Radio Regulations – Article 1, Definitions of Radio Services, <https://life.itu.int/radioclub/rr/art1.pdf>
- [5] https://en.wikipedia.org/wiki/Radio_wave
- [6] Rantec Microwave Systems, 'The Different Types of Wireless Communication', Jan. 2020.
- [7] C. Siva Ram Murthy and B. S Manoj. Ad Hoc Wireless Networks, Architectures.
- [8] J. Clerk Maxwell, A Treatise on Electricity and Magnetism, 3rd ed., vol. 2. Oxford: Clarendon, 1892, pp.68-73.
- [9] I. Pillay, "The impact of inequality and COVID-19 on education and career planning for South African children of rural and low-socioeconomic backgrounds." African Journal of Career Development, 3(1), a36. May 2021. <https://doi.org/10.4102/ajcd.v3i1.36>
- [10] Dube, B. (2020). Rural Online Learning in the Context of COVID-19 in South Africa: Evoking an Inclusive Education Approach. Multidisciplinary Journal of Educational Research, 10(2), 135-157. Jun. 2020. doi: 10.4471/remie.2020.5607

Optimal Angel and Shell Layers of Overwrapped Composite High-Pressure Vessels: A review of previous studies on composite pressure influenced by angle and shell thickness

Nathan Numbi Mukala¹

Leonard M Masu²

Patrick K Nziu¹

ORCID: 0000-0002-9900-5295 ORCID: 0000-0002-8544-6321 ORCID: 0000-0002-5899-0700

¹Vaal University of Technology, Faculty of Engineering and Technology, Department of Industrial Engineering & Operational Management and Mechanical Engineering, Vanderbijpark, Andries Potgieter Blvd, 1911, South Africa

² Technical University of Kenya, Faculty of Engineering and the Built Environment, School of Mechanical and Manufacturing Engineering, Department of Mechanical and Mechatronic Engineering, Haile Selassie Avenue, P.O. Box 52428, 00200 Nairobi

Abstract

The purpose of this article was to review previous studies on the effects of composite angle and shell layer number, on bursting strength in overwrapped pressure vessels. This investigation revealed optimal fibre angle and shell layers determined to achieve improved sustainable composite pressure vessel.

With aim of burst pressure determination, emphasis was made on studies analyzing number of layers carried out using different fibre material. The developed analyses were done with T700s Carbon, Basalt, E-glass and flax. With a variation of material used, a total of 100 experiment were created out with the purpose of generation of a vessel resistant to bursting failure. With the angle as variable, the analysis was performed numerically for shell of 14, 19 and 25 layers overwrapping the liner, being as well an influential factor to the optimization. The symmetrical and asymmetrical lamination patterns was performed analytically and validated experimentally in the determination of optimal angle influencing the bursting pressure.

For this review, the investigated studies on the determination of layer revealed on a threshold of 1400 MPa a weakness at layer 5 on T700s Carbon, E-glass and flax, with the exception of Basalt which reveled weakness at the first layer making this material undesirable. The identification of ultimate angle, 55 was recorded as optimal on the deformation analysis and on the symmetrical and asymmetrical pattern

1. Introduction

To store liquids and gases at high pressure, the need for creating and implementing a reliable container has been thought of with emphasis on vessel strength to prevent bursting failure. Moreover, factors influencing

the degradation or deformation behaviors of vessels, leading to eventual failure, have been the subject of analyses to improve the specific conditions of the design.

The standard conceptual vessel design is rolled sheets formed into a cylindrical container constituting a pressurized vessel constructed to carry low-pressure liquid or gases (Change & Springer, 2017). In contrast, the structural thickness of the vessel is increased with the purpose of provision on strength capability to carry high pressure. Therefore, the need for a strong container of high capacity without increasing weight has sparked a great deal of importance in the modern engineering industries involving equipment such as ships, aircraft, and even spacecraft. For this reason, various methods have been developed to clarify the load handling capability of the cylinder.

Studies such as Mitrevski et al. (2018) analyzed the cylindrical vessel shell reinforced by multi-layers fibre having the correct orientations and yielding the best strength constraint to prevent vessel bursting. This research was done to optimize the concept of pressurized vessel capability under optimal mass. Additionally, it covers areas on axial load exerting a failure toll on the cylinder, based on laminated shell composite subjected to internal and external effects of the applied load. This stress created due to the applied pressure leads to the bursting of the cylinder as the common failure mode. Further to that, observed in global failure of the entire unit, a skin degradation with a crumbling of the stiffener occurs if incorporated in the design of the cylinder to reinforce its wall. This skin degradation and crumbling of the stiffener is a major concern studied by Mitrevski et al. (2018) to have a clear insight on the failure leading to the bursting of the vessel.

The investigation of composite with multilayer angle-ply has been thought of by Reid & Zhou (2000) under predetermined loading conditions to optimize fibre orientation and prevent the collapse of the vessel. The laminated shell layers must be accurately modelled, either symmetrically or unsymmetrically, for efficient resistance of bursting effect.

Commonly, one single analysis is not enough to structurally determine the failure mode occurring on a vessel though shelled with a composite material to reinforce its structural integrity. Hence, the designer resorts to numerous analysis tools, which may not necessarily exhibit the same result on each analysis (Hashin, 2016). Various results of each failure mode using different methodologies are reviewed to better understand the structural limitation of the shell composite properties or material composition and orientation pattern to yield an optimal safe vessel.

2. Composite material

Composites are a form of a combination of different materials blended together despite their diversity on a micro-scale level, which does not change when merged together. A typical example of composite material is the old brick fabrication, based on the combination of a mixture of straw constituting the fibre

reinforcement and clay used as a matrix to form a whole composite (Hashin, 2016). The study of composite material included with fibre date since early 1940. The fibrous polymer was first developed based on the difference between the traditional material and laminate composite driving the response of the load application, which in the case of composite is more direction dependent.

It is these benefits brought as advances, technology aim in exploiting. Due to the lack of demand met by today's metallic alloys, the composite material is given great consideration as to its advantage in decreasing the vessel weight while increasing in strength (Hashin, 2016). What is more, the reduction of composite pressure vessel failure is due to a great flexibility of fibre, bringing strength and stiffness to the material in the wanted direction. The above-mentioned benefits have been extensively exploited in the carbon fibre, mostly considered due to its high strength application.

Abrate (2015) study stated that the theoretical strength in most composites is found to be much greater than the experimentally measured strength. It is due to imperfection detected in cracks sprayed perpendicular to the application of the load direction not accounted for. This should be an area deeply investigated to have a clear and extensive understanding of the application of polymer fibre. From the common knowledge, they are materials used in the composition shell, not directly in the design application. They are submerged and blended in a binding matrix, transferring load from fibre to fibre and protecting them from environmental damage to form a strong composite but still detrimental in its strength due to flaws in the form of cracks.

All composite manufactured or rather created are mostly composed of fibre bringing strength to the composition and of a matrix material binding them together to form a fibrous composite. The fibre is embedded in a matrix of different particles composed of material. In the case of layers of fibres, it is also embedded in a matrix of other materials for protection and stress transfer.

In the entire composition shell-based of fibre and matrix, a large volume fraction is occupied by the fibre being the major constituent of the mixture. Reinforcement of the structure is achieved by using a matrix, which has a major limitation of being mostly fragile with smaller dimensions. The fibres embedded in the mixture with a matrix shared the load applied on the composite. Moreover, the composite can carry bursting load-dependent on the type of fibre being used. Glass fibre, for instance, has high strength and insulation properties and good resistance to any abrasive liquid the composite might contain (Change & Springer, 2017). On the other hand, the carbon fibre has high strength, a good modulus, and a high fatigue strength needed for the load handling capacity mentioned in the preceding paragraph. Fibres such as the Aramid exhibits a high impact resistance. It gives the advantages of reducing the limitation of a matrix whose role is to facilitate the sharing of stresses between fibres in the mixture and protect them against environmental and mechanical abrasive effects. Each of the composite materials used in the conceptual

design has its own advantages imparted in the structure. When conceiving a composite pressure vessel, one should analyze and mindfully consider the material shelling the liner for strength to be reliably imparted in the design

2.1 Characteristics and applications of composite materials for overwrapping pressure vessels.

Conventional metallic materials are of different properties varying in strength and elasticity. They can withstand critical load at a certain limit beyond which fibre polymer composite has surpassed by offering a reliable combination of rigidity and elasticity. The structure obtained from this effect has a tremendous load-carrying capacity capability. Hence, the composite is more desired due to the low specific gravity and high ratio of strength over the entire weight of the structure (Pimenta, 2015).

One other characteristic the fibre brings as an advantage is that it is directional dependent in terms of properties. Comparatively, metallic materials, such as steel and aluminum, exhibit structural composition considered isotropic. All their respective properties are equal throughout the material irrespective of the direction.

Abrate (2019) study mentioned that vibration energy absorption is another advantage the fibre composite possesses. It incorporates internal damping that allows the absorption and reduction of vibration and noise transmitted to the neighboring structure, which might be overwrapped. Hence, the mentioned properties make composite materials different and more desirable than conventional metallic materials. The study of Abrate (2019) focused more on the strength properties. It did not investigate deeply the beneficial impact of fibre vibration properties being an influential factor in the vessel structure.

Metallic materials or alloys have limited capacity beyond which fibre composite handles. For this reason, many industries have adopted the idea of using composite as the material choice for structural integrity design requiring strength for an efficient, reliable performance (Pimenta, 2015). Composite materials have many applications due to their benefits, which extend from the aircraft industry where light weight and strength are required. This integrity leads to composite in the body and mainly in the wing portion of the plane. Moreover, its applications extend in fields such as space, marine and automotive racing cars or even as little as sports goods such as tennis rackets and golf clubs. The benefits of fibre are numerous depending on the application to be used, which reside at the shell of the composite container in case of pressure vessel.

In the previous chapter on the composite shell, the mentioned fact emphasized the need to deeply analyze the material constituency of fibre overwrapping the liner as it occupies a large portion of the composite laminate volume fraction. Hence, the laminate fibre can be made of different materials such as Kevlar, carbon fibre or glass fibre, depending on the required properties. In addition to that, each type of material shares the load acting on the composite differently due to their diversity in properties.

A study by Vasiliev & Jones (2018) defined Kevlar fibre as an organic compound made of carbon, oxygen, nitrogen and hydrogen. It has the advantages of having a low density, high impact and tensile strength, created due to the high proportion of molecular chain bond oriented in the fibre axis. In addition to all these advantages, the Kevlar fibre has an intense heat resistant property with a high melting point of 500°C. The Kevlar fibre is mostly used in body armor, marine area, and even aerospace applications.

On the other hand, glass fibre is a typical example of common polymer composite material consisting of numerous extremely fine fibres of glass. It is used for its advantages of having high strength and excellent insulating properties with thermal conductivity of 0.05 W/mK. The main comparable advantage the glass fibre has over other polymers is its ability to be less brittle when used in a composite. Therefore, glass fibre is one of the materials often used as a reinforcing agent, hence creating a lightweight, solid and reliable composite structure (Jones, 2020).

Glass fibre is a lightweight material due to its composition of excellent fibre made in the manufacturing process. Although it is a very light material, it exhibits the ability to be strong. Nevertheless, this strength exhibition of the glass fibre has been surpassed by the one exhibited by carbon fibre due to its low thermal expansion coefficient, high young modulus and fatigue resistance. These mentioned properties classify carbon fibre as the most desirable fibre used as reinforcement in the manufacturing of overwrapping pressure vessels and areas requiring light but strong properties such as aircraft and spacecraft, racing car bodies (Change & Springer, 2017).

With this emphasis mentioned about the composite material properties, great importance is given to the constituent portion relative to the entire composite volume since it influences the mechanical response of the used material. With this in mind, a study by Hwang et al. (2003) analysis the effect of the volume fraction on composite pressure vessel and ultimately reach a shell volume with a realistic frame and eventually exploit the optimal space between fibre. Therefore, it is of the utmost importance to associate the shell material to the portion they occupy in their composition and reach optimization.

3. Problem statement

Pressure vessels though being of a proper structural strength integrity, are susceptible to bursting failure resulting from an increase of handled pressure. Although their structures are tolerant to damage at predetermined specific pressure range, the exposure to unsupported loads (pressure) requires an increase in structural thickness for sustainability, which ultimate lead to an increase of weight.

With this unsupported load requiring additional vessel materials (thickness) for its sustainability, the need of strength improvement without increase of weight was, therefore, achieved by the development of pressure vessel in form of composite structure.

4. Thickness of composite pressure vessel

The thickness of the composite pressure vessel is a parameter playing a major role in the vessel's structural integrity. Further reviewed literature by Gentilleau, et al. (2015) considered in their analysis thickness as a factor to determine a reliable concept with the capability of withstanding pressure without failure. In contrast, the analysis was performed with the purpose of predicting the damage of structure at its maximum stress capability, beyond its design limit. Nevertheless, this analysis was performed on the capability of the composite pressure vessel leading to the optimization of the thickness for a reliable structure.

Further to that, Gentilleau, et al. (2015) showed that the strength of composite pressure vessels also depends on the fibre layer constituting the portion of the composite pressure vessel thickness. A similar conclusion has been reached before in research by Levend and Nuran (2002), stating that the structural composition of the shell has an influential role on the thickness of the vessel, as stresses vary layer to layer with its peak value at the inner one. The procedure adopted was based on a sequence of loading and reach failure of layers which ultimately led to an adequate thickness resistance to bursting.

The approach of Gentilleau, et al. (2015) on the composite pressure vessel structure used finite element analysis (FEA) to show the fibre layers influence on the allowable thickness determination. With a 3 D CAD software, a composite pressure vessel is conceived, then translated and calculated into ANSYS with all the design dimensions. The young modulus, Poisson ratio and density of the liner are introduced in the concept. On the other hand, the shell properties are taken as independent variables from the young's modulus, Poisson ratio and the coefficient of deformation, considered in the horizontal-vertical and radial direction. With the translation displacement in all directions and the boundary condition introduced in the software, one mesh is performed per layer with an assumption of homogeneity. The end result is 366709 nodes joining the meshed elements on which boundary conditions are assigned and 123346 elements linked on liner and composite, representing the modelled area. These numbers of nodes and elements have been reached due to the accuracy level and simulation time required for this analysis to be performed. Therefore, depending on the mentioned application, the interface software adopted in this particular study was ANSYS, which, compared to other software such as Abaqus, is equally accurate in the simulation level.

Furthermore, to characterize the bursting failure in terms of layers, the vessel made of a T700s Carbon fibre is exposed to an internal pressure of 1500 bar higher than the maximum design pressure of 700 bar.

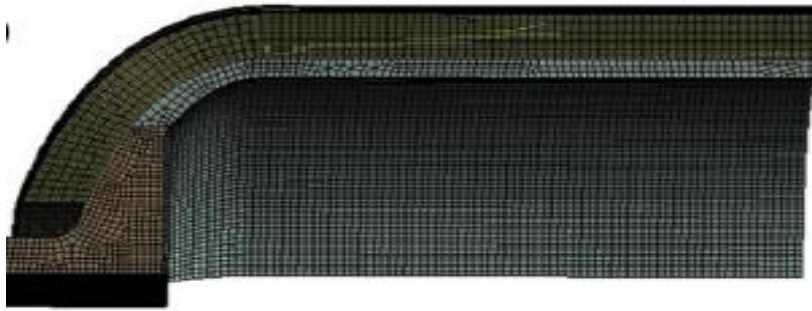


Figure 1: Meshing of cylinder (Gentileau, et al., 2015)

At 90° orientation and bursting pressure exposed at each layer as in figure 2, the simulation exhibits a pressure of 1483 bar shy representing 6% more of the required threshold minimum pressure of 1400 bar, putting layer 5 as the most critical one. Moreover, it is observed that the more the layer increase in shell thickness, the more critical the handled pressure by layer is brought to the minimum burst pressure of 1400 bar. This finding exhibited in figure 2 contradicts the statement of a decrease in bursting failure with an increase in shell thickness. A theoretical number of layer increased should aim into an increase in strength capability of pressure handling (Change & Springer, 2017). Hence, as shown in Figure 2, the assumption of an increase in mechanical strength, with an increase in shell thickness, contradicted the findings exhibited on layer 5, being 20% of the shell thickness of 11.1 mm represented by 25 layers.

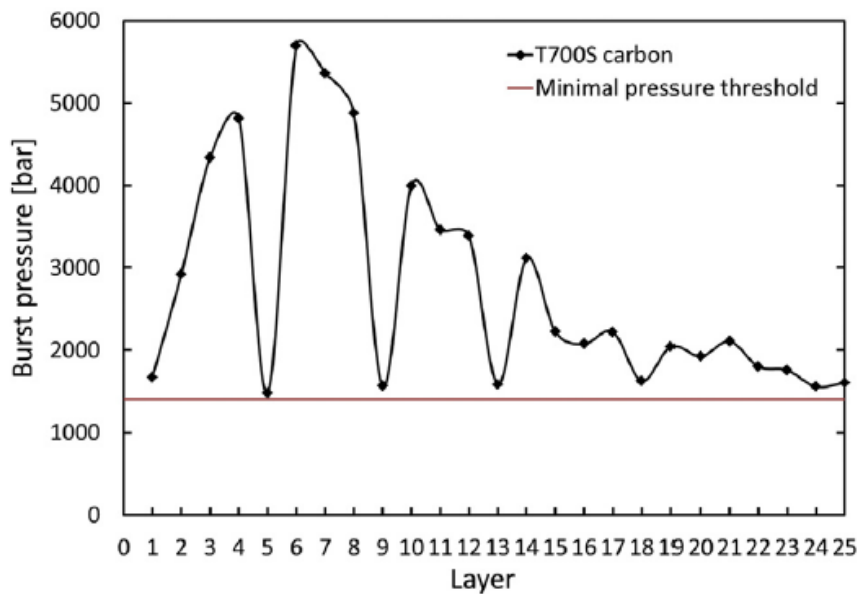


Figure 2: Variation of bursting depending of Carbon fibre layers (Gentileau, et al., 2015)

To illustrate or rather verify this finding, the result is compared on radial deformation to a simulation multilayer composite exhibited in Figure 3. Despite the slight difference in the Poisson ratio and Young's modulus values, both results showed a trend representing an increase of deformation with an increase of

pressure. The small discrepancy between the two analyses is due to the different simulation values used and the mesh and boundary conditions set upon the structure.

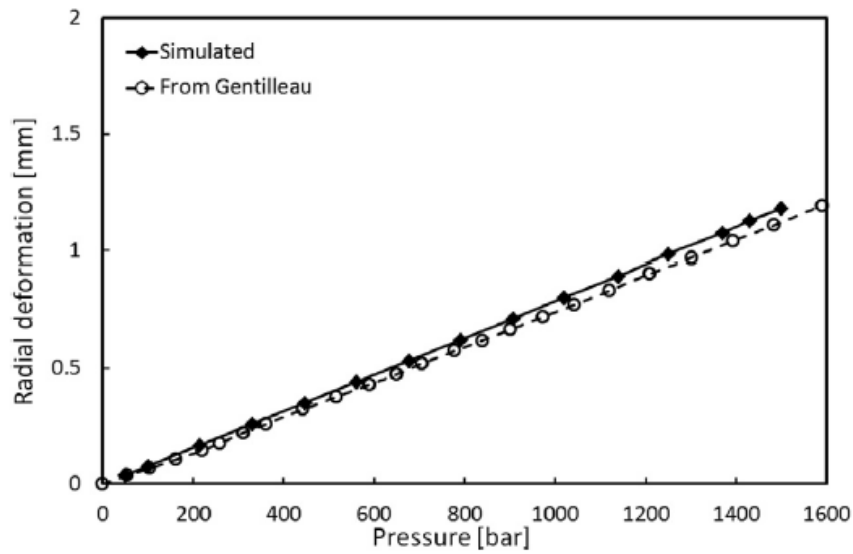


Figure 3: comparison of analysis (Gentileau, et al., 2015)

Keeping in mind the relationship between fibre layers constituting the shell and burst pressure, Bouvier, et al. (2018) had a similar approach as exhibited in figures 4, 5 and 6. A simulation was done on composite of 25 layers of alternative fibres material for comparison to determine their behavior in terms of bursting pressure and have for each case the number of a layer at which thickness can be considered optimal. This polymeric test has revealed damage again at the fifth layer with Flax or E-glass fibre used as shell material. The exception was noticed on the basalt fibre, which forms the first layer, exhibiting weakness. The burst pressure of the alternative fibre has been recorded to be considerably low with values as shown in Table 1, comparatively to the threshold minimum pressure of 1400 bar.

Table 1: Burst pressure mechanism for alternative high-pressure vessel (Bouvier, et al., 2018)

	T700s Carbon	Basalt	E-glass	Flax
Weak layer	5	1	5	5
Type of burst	Safe	Unsafe	Safe	Safe
Burst pressure (bar)	1483	873	1039	422
Radial deformation	1.10	2.04	1.97	2.44

Moreover, despite the lower burst pressure, the simulation has shown a more or less similar pattern of degradation in layer capability on the E-glass and the Flax fibre, comparatively to the carbon fibre. The burst pressure per layer has been recorded on each one of them under the threshold pressure with small fluctuation between them. When using the Basalt as shell fibre, the simulation made it an undesirable material required to have a sustainable thickness of the composite, with its deformation being higher already at the first layer.

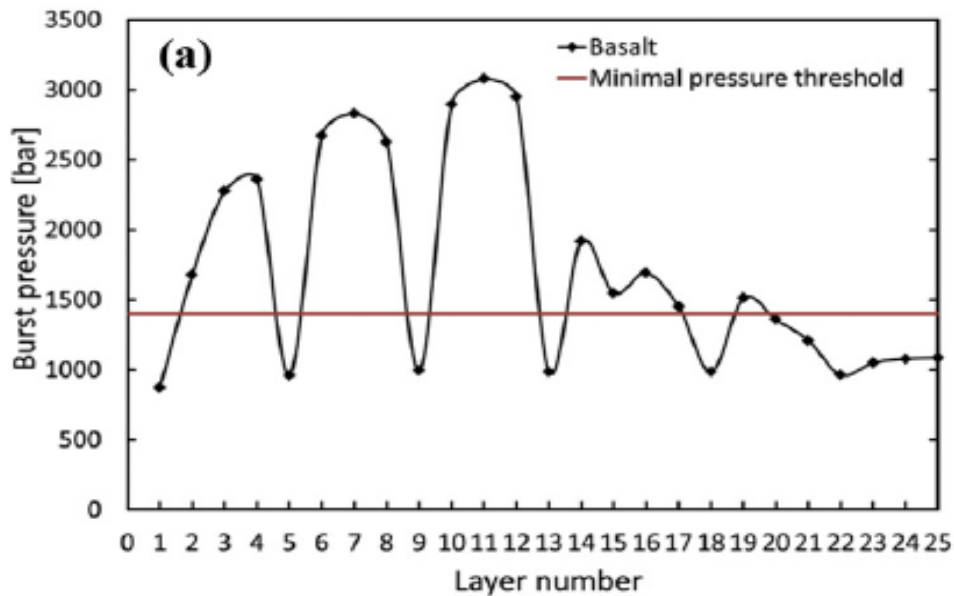


Figure 4: Variation of bursting depending of basalt fibre layers (Bouvier, et al., 2018)

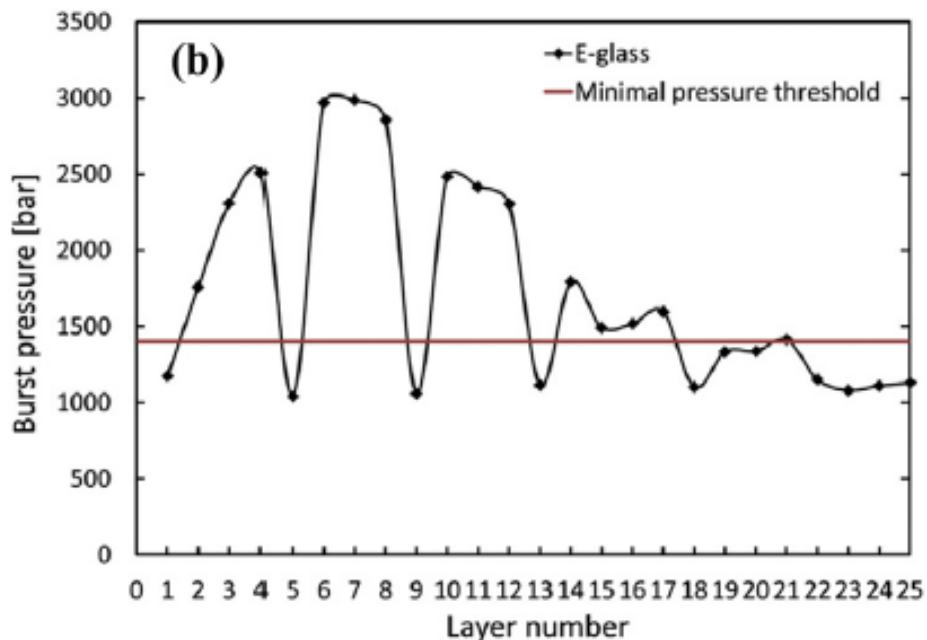


Figure 5: Variation of bursting depending of E-glass fibre layers(Bouvier, et al., 2018)

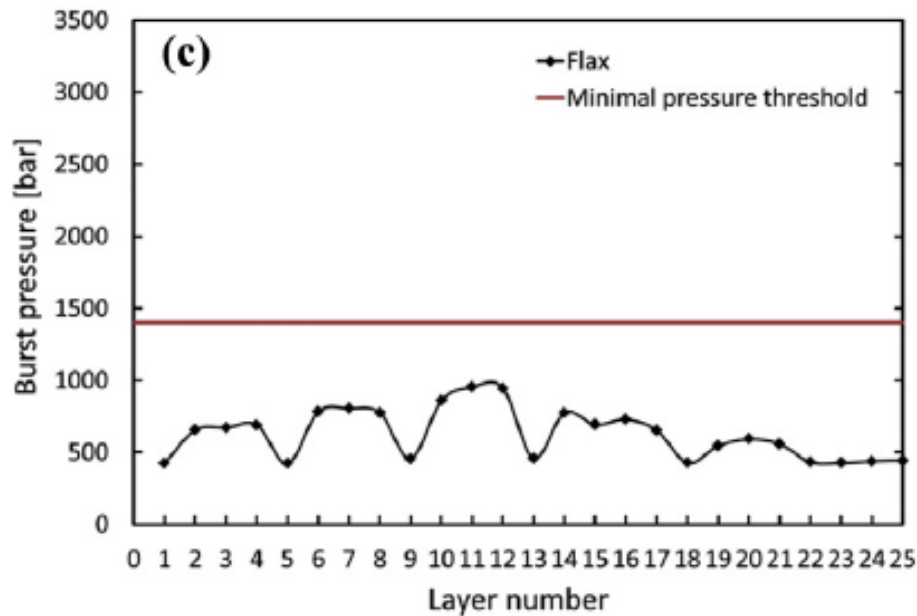


Figure 6: Variation of bursting depending of flax fibre layers (Bouvier, et al., 2018)

5. Winding angle influence on fibre thickness

Fibre dimension is the basic measurement constituting the thickness of the lamina lay of a laminate shell. In the study of fibre dimension for the determination of reliable composite pressure vessels, researchers such as Onder and Sayman (2018) and Sulaiman, et al. (2015) have not been limited to the effects of internal pressure. Further investigations have considered shell winding angles as influential factors to the structural integrity of composite pressure vessels. With that in mind, analyses are performed on the fibre orientation, either symmetrical or ant symmetrical, with a view of finding an optimal structure resistant to bursting failure.

Therefore, theoretical, numerical and experimental methods have been used for the determination of a suitable pattern of winding angle influencing the fibre dimension and leading to an optimal design of a composite pressure vessel. These methods are briefly discussed hereunder:

5.1. Theoretical approach

Upon failure, the most affected part of the composite pressure vessel is the shell material, as it is more amendable and sensitive to temperature, moisture and time, compared to the metallic counterpart of the vessel (Camanho, 2020). The environmental and life cycle impact on composites are studied objectives called for further analysis, which will drastically affect the developed principles adopted for the determination of fibre dimension leading to a reliable composite pressure vessel.

Nevertheless, bursting failure being a source of damage recorded on composite could be generated as mentioned from different factors such as wrong structural pattern angles of shell winding. Onder and Sayman (2018) study developed an analytical method to have a picture of the winding impact of the

mechanical properties and behavior of fibre. This case study considered different stacking sequences orientation symmetric and antisymmetric and generated on the multi-layered shell the required fibre dimension.

Furthermore, with the Tai-Wu method, maximum stress and strain theories, angle of orientation and the fibre dimension are determined by taking the performance of the composite pressure vessel with bursting pressure as the limiting factor. Additionally, the winding angle was chosen between 0° and 90° with the purpose of determining the angle at which the optimum winding pattern is achieved. Hence, for both symmetrical and unsymmetrical conditions, calculations are done on the cylinder of different shell orientations, and a reliable composite vessel structure is obtained.

Alternatively, to the previously mentioned study, a further review should consider besides internal pressure, the influence of hydrothermal loading on angle pattern and fibre dimension determination for an eventual reliable structure. Internal pressure and hydrothermal force have been used both in analysis based on fibre pattern and yielding of solution on the elasticity of overwrapped pressure vessel overwrapped by fibre shell. Hence, the combination of both effects on fibre dimension netting analysis would lead to a realistic concept.

5.1.1 Failure principle application

The study by Onder and Sayman (2018) did not emphasize enough the role played by winding angle in the structural integrity of the composite vessel. The required angle for each shell layer is an important portion of the optimization analysis of the composite pressure vessel.

Comparatively, a study by Sulaiman, et al. (2015) aims to determine the maximum burst pressure with its maximum deformation and optimize winding angle on the different failure modes. With this approach of winding angle considered in the analysis of maximum burst pressure, the investigation of multilayer dimension is emphasized on the composite behavior. Sulaiman, et al. (2015) used netting analysis as a technique with the assumption of fibre stiffness neglected.

This study was based on a thin cylinder, as the display on Figure 7, where t and l represent the thickness and the length respectively, under an internal pressure of P . The equation 1 was used for the hoop and axial stress determination.

$$N_{\phi} = \frac{PR}{2}, N_{\theta} = PR \quad (1)$$

Hence with a thickness depicted as in figure 1, the axial and hoop stress are as follow in Equation 2.2.

$$\sigma_{axial} = \frac{N_{\phi}}{t} = \frac{PR}{2t}, \sigma_{hoop} = \frac{N_{\theta}}{t} = \frac{PR}{t} \quad (2)$$

According to the equilibrium across the section, the axial and hoop are denoted in Equations 3 and 4 as follow.

$$PL(2R) = 2\sigma_{hoop}Lt \quad (3)$$

$$P\pi r^2 = 2\sigma_{axial}(2\pi Rt) \quad (4)$$

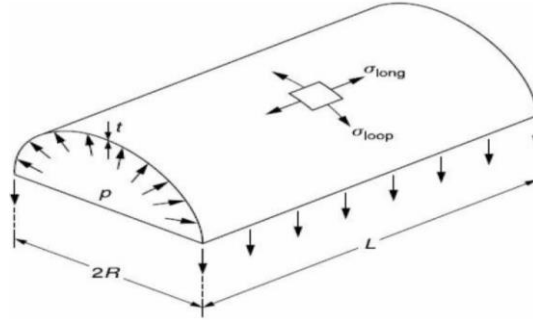


Figure 7: Cylinder Shell (Sulaiman, et al., 2015)

As shown in Figure 2.8, with the cylinder wrapped at an angle of α with fibre and on netting assumption of 2:1 ratio between the hoop and axial stress, the use of ultimate tensile strength lead to the estimation of the optimal winding angle as in Equations 5 and 6

$$N_{\phi} = \sigma_u t \sin^2 \alpha, N_{\theta} = \sigma_u t \cos^2 \alpha \quad (5)$$

$$\frac{N_{\theta}}{N_{\phi}} = \tan^2 \alpha = 2 \rightarrow \alpha = \arctan(\sqrt{2}) = 54.7^\circ \quad (6)$$

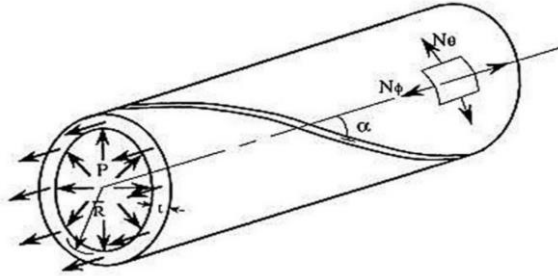


Figure 2.8: Hoop, axial and internal pressure diagram (Sulaiman, et al., 2015)

Moreover, in order to determine the strength in the composite layers, Sulaiman, et al. (2015) used the failure theorem for this evaluation. With the strength properties divided into five independent one, the denotations are as follow:

X_t = longitudinal tensile strength

Y_t = transverse tensile strength

X_c = longitudinal compressive strength

Y_c = transverse compressive strength

S= in-plane shear strength

The Tsai-Wu failure criterion Equation 7, for determination of orthotropic stress condition was the first to be used.

$$F_{11} \sigma_1^2 + F_{22} \sigma_2^2 + F_{66} \tau_{12}^2 + F_1 \sigma_1 + F_2 \sigma_2 + 2F_{12} \sigma_1 \sigma_2 \geq 1 \quad (7)$$

Where:

$$F_1 = \frac{1}{x_t} - \frac{1}{x_c}, F_2 = \frac{1}{y_t} - \frac{1}{y_c}, F_{11} = \frac{1}{x_t x_c}, F_{22} = \frac{1}{y_t y_c}, F_{66} = \frac{1}{s^2}, F_{12} = -\frac{1}{2} \sqrt{F_{11} F_{22}} \quad (8)$$

The Tsai-hill failure criterion was secondly used as well as per Equation 9

$$F_{11} \sigma_1^2 + F_{22} \sigma_2^2 + F_{66} \tau_{12}^2 + 2F_{12} \sigma_1 \sigma_2 \geq 1 \quad (9)$$

Where:

$$F_{11} = \frac{1}{x^2}, F_{22} = \frac{1}{y^2}, F_{66} = \frac{1}{s^2}, F_{12} = -\frac{1}{2} \left(\frac{1}{x^2} - \frac{1}{y^2} \right) \quad (10)$$

Through this analytical approach by Sulaiman et al. (2013), the optimal winding angle was found from Equation 6 to be of a value of 54.7°. The shortcoming of Sulaiman, et al., (2015) review was depicted on the missing portion of the sequential direction of lamina lay up in the laminate as each layer structurally influences a multidirectional shell composite. Their failure approach in the determination of the allowed shell structure was due to the fact that fibre-based laminates were considered to be orthotropic with different properties throughout the structure. Hence influencing the stress propagation on the composite materials.

5.2 Experimental approach

The study or rather an analysis of a required angle ply to optimize fibre dimension and yield a strong, reliable composite pressure vessel, have extensively progressed in the experimental area. With that being said, scientific investigation has been carefully established in the relationship of the composite shell layers direction and bursting effect of material structure.

Moreover, to determine the said relationship, a scientific test by Demir (2017) has been developed to have a hold and control over an extraneous variable to the shell winding angle. This was performed by manipulating independent variables such as temperature and mainly internal pressure and, hence, measuring the dependent variable, which was the vessel's bursting effect. Demir (2017) manufactured filament wound pipe using a computer numerical control (CNC) machine with numerous winding angles capabilities. Therefore, an E-glass fibre was used as reinforcement blended in an epoxy CY-225 resin for the matrix. Furthermore, symmetrical and unsymmetrical sequences of [45°/-45°], [55°/-55°], [60°/-60°]

[75°/-75°] and [88°/-88°] were used as lay-up of the laminate shell. This experiment led to a fibre thickness of 1.6 mm required for a reliable, strong composite material resistant to busting.

To have a better view on the conceptual structure leading to this result by Demir (2017) The design was conceived with a length and inner diameter taken as 400 and 100 mm, respectively. With a calculated volume fraction of 0.53, mechanical tests were performed to determine the specimen properties such as modulus of elasticity E and poison ratio ν under a tensile machine. In the same logic, the strain gauge was determined in the direction of 45° to 88°. With all these parameters set in place, Demir (2017) study was able to emphasize the strength factor for an optimal composite pressure vessel.

From previewed literature on winding angle orientation and determination of fibre dimension, it is evident that theoretical analysis and experimental study are mostly based on winding orientation between 0 ° and 90 °. On this experimental analysis, the discrepancy was mostly observed from 45° to 88 ° winding angle (Onder, et al., 2018). In addition, when considering the bursting pressure against angle orientation, the experimental pressure has exhibited a difference in the symmetrical and unsymmetrical orientation of the considered angles. From Figure 9, the burst pressure of the symmetrical orientation seemed lower comparatively to the unsymmetrical ones, which shows slightly higher bursting pressure values of about 35% more on average.

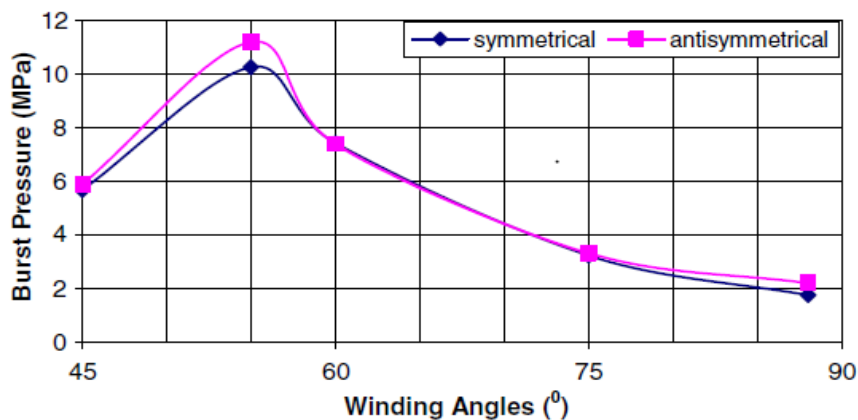


Figure 9: Variation of bursting depending on the angle (Onder, et al., 2018).

More so, in the study of fibre dimensions, analytical and experimental solutions should give approximately the same result of bursting pressure within the same range of angle orientation. However, further reviewed literature by Onder et al. (2018) has concluded that the analytical method does not give close results to the experimental on a certain chosen angle with the exception of the optimal bursting angle of 54.7 °. Experimental methods have exhibited a low bursting pressure effect at high angle orientation compared to the analytical approach, as seen in Figures 10 and 11. The discrepancy between the two methods is due to the fact that the analytical technique is more of an approximation tending to the reality of the experimental technique. Numerous influential factors were not considered in the analysis, such as the ones mentioned

in section 7 of this literature review. In addition, almost 45% and 0.5% peak value difference respectively in symmetrical and unsymmetrical was recorded, making the analytical approach closer to reality at its optimal unsymmetrical orientation.

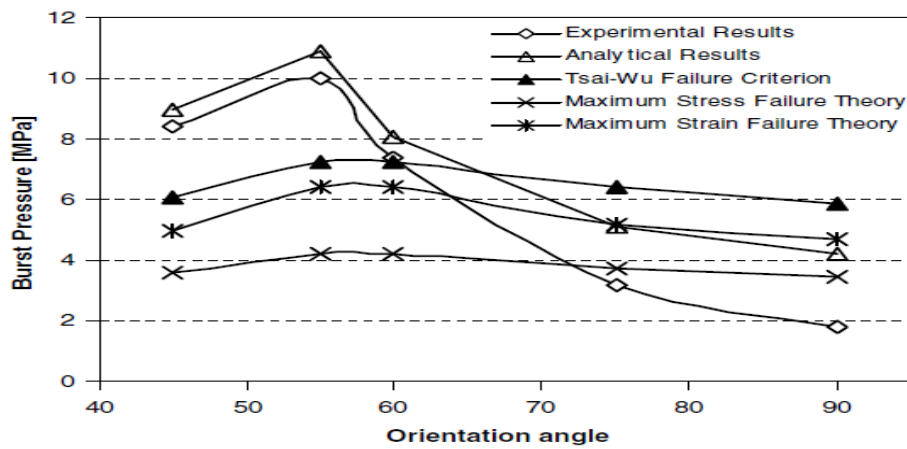


Figure 10: Comparison of analysis in symmetrical case (Onder, et al., 2018)

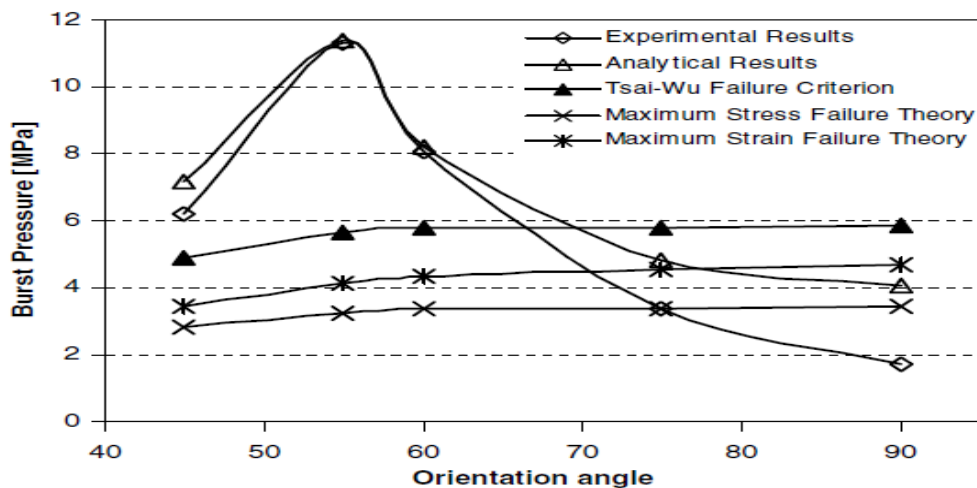


Figure 11: Comparison of analysis in unsymmetrical case (Onder, et al., 2018).

In brief, experimental studies are the most reliable when it comes to the result of scientific research, as many factors, when performed, are unconsciously considered, which might not be the case for an analytical approach. Nevertheless, when focusing on optimization of angle orientation on the overwrapped composite vessel, the two methods have shown similarities, especially on the maximum optimal angle obtained at 54.7 °, at which burst pressure is the highest for both the experimental and the analytical method.

5.3 Numerical approach

The numerical approach in the study of composite pressure vessels can be used as a technique to determine the bursting pressure when considering the shell winding angle as an influential factor. With properties of material, element type and boundaries condition predefined, structural analysis can be performed through

finite element analysis and optimize the design by interpreting the result obtained for the simulation as exhibited in Figure 12.

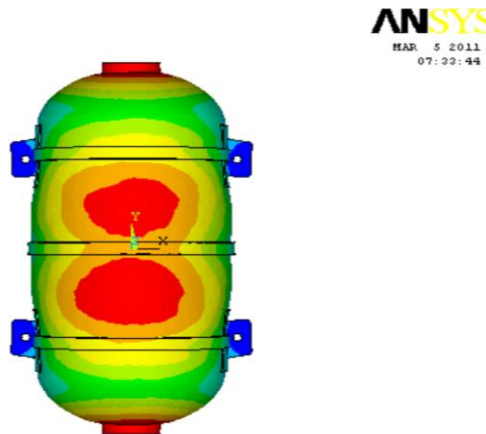


Figure 12: Pressure vessel simulation with winding angle influence (Yarrapragad, et al., 2017)

A study by Yarrapragad, et al. (2017) used the finite element analysis as a technique to perform a simulation on a shell composite pressure vessel and obtain at maximum load and optimal angle the minimum deformation of the composite vessel. This mentioned objective was extended to two different shell materials, namely the glass and the carbon. Therefore, upon analysis on composite pressure vessel oriented on a symmetrical winding angle of 45° , 55° , 65° , 75° and 85° for chosen layers of 14, 19, and 25 plies determine the influence of the fibre over the structural integrity composite shell (refer to figure 13, 14 and 15).

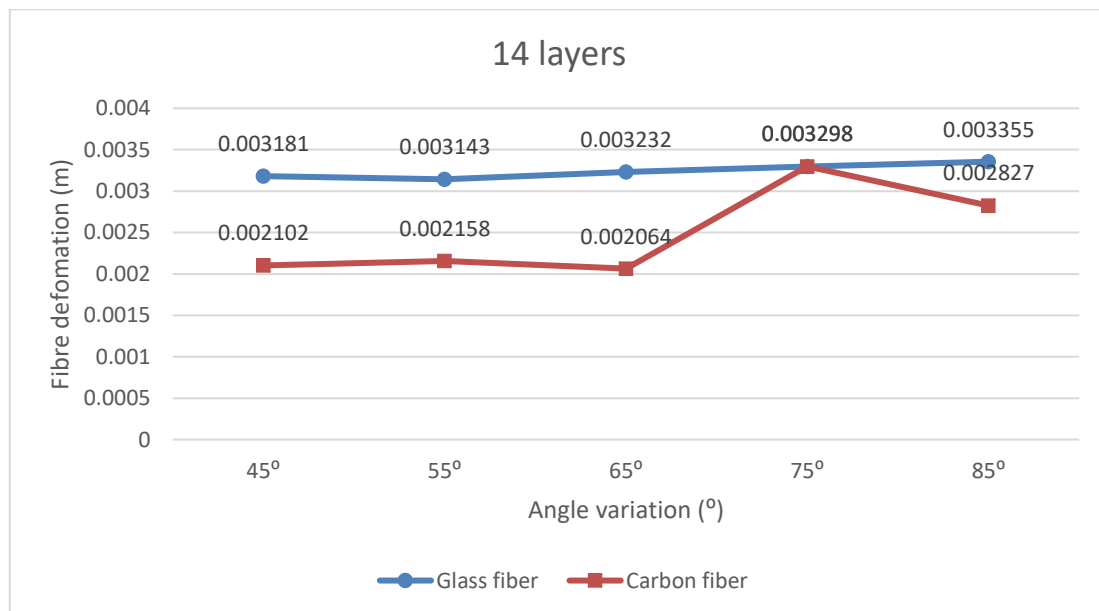


Figure 13: Deformation of Carbon and glass fibre (Yarrapragad, et al., 2017)

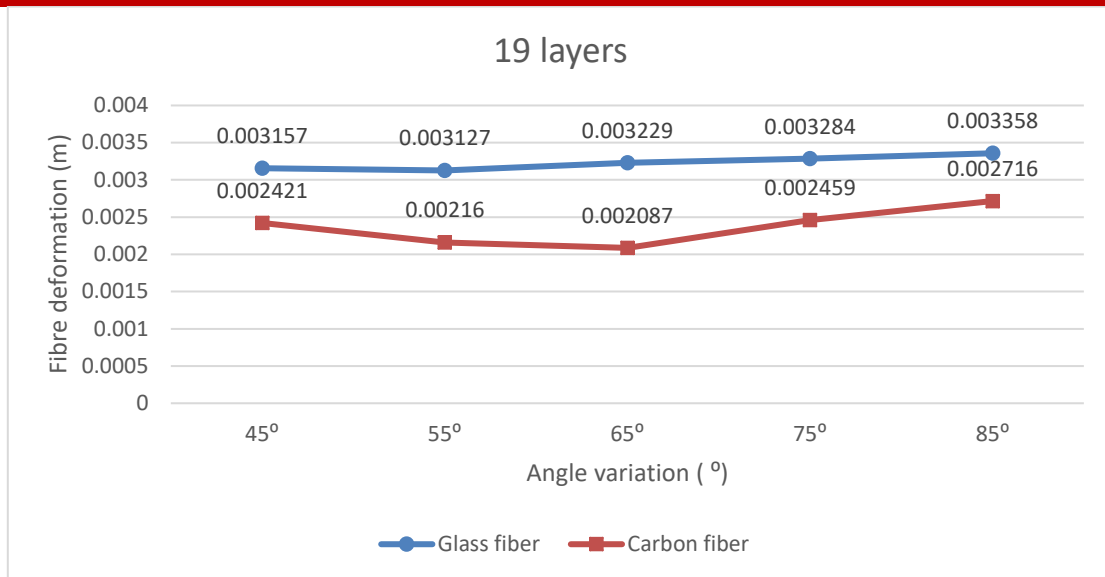


Figure 14: Deformation of Carbon and glass fibre (Yarrapragad, et al., 2017)

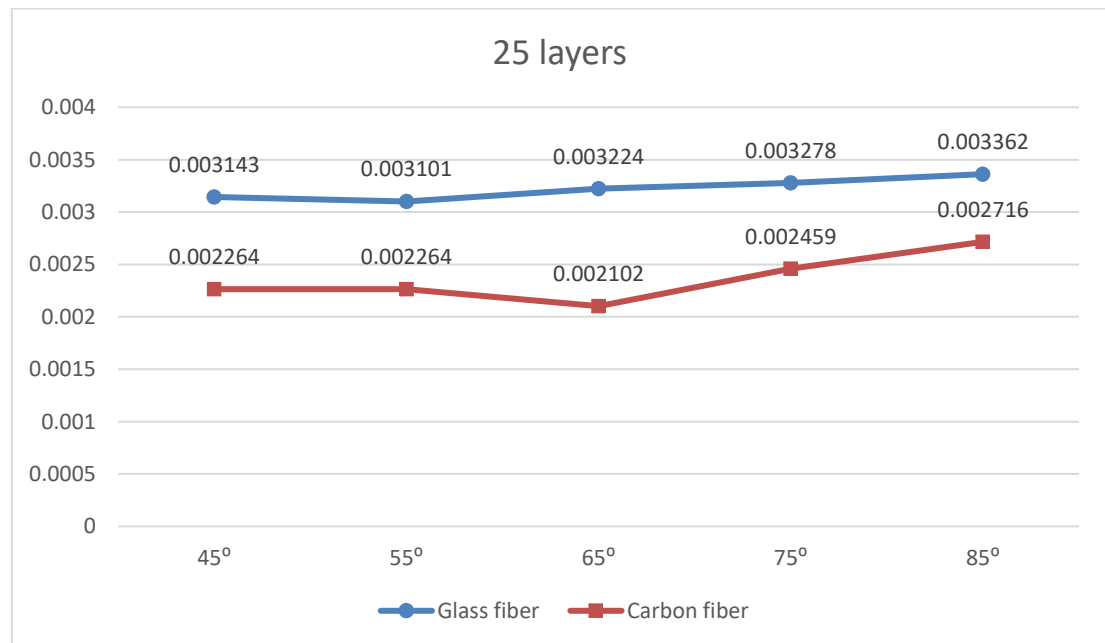


Figure 15: Deformation of Carbon and glass fibre (Yarrapragad, et al., 2017)

Through this study, layers and angles random incremented have been used to emphasize their influential effects on the deformation of the composite material. Further, the Von Mises stress (maximum stress) has been used through ANSYS and results were generated with finite element analysis. As depicted in Figures 13, 14 and 15, minimum deformations for the glass were observed through the three types of layers at an angle orientation of 55°. On the other hand, the carbon fibre registered minimum deformations at 65° winding orientation. These findings greatly emphasize the importance of winding angle over the composite pressure vessel deformation, which will ultimately lead to a structural failure if overlooked.

6. Existing knowledge gaps

Throughout this reviewed literature, areas requiring further, and deeper analysis have been depicted to better understand and design a reliable structural concept good enough to resist bursting failure. In the determination of fibre dimension, potential areas of deep analysis were identified on the type of influential load to the winding angle, which in turn influence the fibre dimension. Hence, besides the mechanical loading exerted by the internal pressure to the structure, the hydrothermal loading has been identified as an alternative load requiring further investigation. Therefore, combining both effects on the netting analysis of fibre dimension would lead to a realistic concept, calling for further study. Shortcomings as well were noticed on some mentioned studies such as Sulaiman et al. (2015), which emphasized more on the role played by winding angle in the structure integrity of the composite vessel comparatively to Onder and Sayman (2018), the only downside was on the missing portion of the sequential direction of lamina lay up in the laminate as each layer structurally influence the multidirectional shell composite. Hence, these depicted gaps aim in the contribution of the development of a more reliable optimal design as they are calling for further investigation.

7. Conclusion

Composite pressure vessels are structural integrities constituted of different parts. For that effect, factors influencing the structural integrity of the vessel have been the subject of numerous research with the purpose of determining the limit in terms of strength and relationship they have with the applied load.

The analyses on layers constituting the shell thickness have revealed despite the lower burst pressure, similar pattern degradation in layer capability on the E-glass and the Flax fibre, comparatively to the carbon fibre. With the simulation done on composite made of 25 layers in order to determine the behavior in terms of bursting pressure and ultimately generate the number of layers at which thickness can be considered optimal. The polymeric test revealed damage on the fifth layer with Flax, carbon fibre or E-glass fibre used as shell material. The exception was noticed on the basalt fibre, which forms the first layer, exhibiting weakness.

In term of angle orientation as influential factor to the structure integrity of a composite shell fibre, the theoretical, experimental and numerical approach reveal optimal value at approximal 55°.

In brief, with the need of strength improvement in order to resist bursting effect, influential factors to the structural integrity of the composite pressure vessel should be mutinously chosen to determine a reliable, optimal conceptual design of a composite pressure vessel, as each of them has a different degree of impact on the structure

References

- Abrate, S., 2019. Impact on composite structures. *Cambridge University Press*, pp. 86-89.
- Adali, S. & Verijenko, V., 2018. Optimization of multilayered composite pressure vessels using exact elasticity solution. *Composite Pressure Vessels*, pp. 203-312.
- Alexander, C. S., Key, C. T. & Schumacher, S. C., 2018. Dynamic Response and Modeling of Carbon Fibre-epoxy Composite Subject to Shock Loading. *Journal of Applied Physics*, pp. 22-114.
- Barboza, E. ., 2011. Experimental and numerical analysis of an LLDPE/HDPE liner for a composite pressure vessel. *Polymer Testing*, Volume 30, pp. 693-700.
- Bouvier, M., Guiheneuf, V. & Jean-marie, A., 2018. Modelling and simulation of a composite high-pressure vessel made of sustainable and renewable alternative fibre. *International Journal of Hydrogen Energy*, Volume 44, pp. 11970-11978.
- Camanho, S., 2020. Theory of elasticity of an anisotropic body. *Moscow: Mir Publishers*, pp. 34-56.
- Cerit, M., 2022. Corrosion pit-induced stress concentration in a spherical pressure vessel. *Thin-Walled Structures*, Volume 50, p. 29.
- Change, F. K. & Springer, G. S., 2017. The strengths of fibre-reinforced composite bends. *Journal of Composite Mater*, pp. 30-45.
- Choi, H. I., 2018. Low-velocity impact response analysis of composite pressure vessel considering stiffness change due to cylinder stress. *Composite Structures*, Volume 160, pp. 491-502..
- Daniel, I. M. & Ishai, O., 2015. Engineering mechanics of composite materials. *Second Edition Oxford University Press*, pp. 34-67.
- Delfosse, D. & Poursartip, A., 2000. Energy-based approach to impact damage in CFRP laminates. *Composites Part A*, pp. 647-655.
- Demir, I., Sayman, O., Dogan, A., Arikan, V. & Arman, Y., 2017. The effects of repeated transverse impact load on the burs pressure of composite pressure vessel. *Composites: Part B*, Volume 68, pp. 121-125.
- Dincer, I. & Cengel, Y., 2016. Pressure Vessel Strength. *Environment and Sustainable Development*, Volume 3, pp. 116 - 149.
- Farhood NH, K. S., 2017. Burst pressure investigation of filament wound type IV composite pressure vessel. *American Institute of Physics Conference Proceedings*, pp. 56-68.

Frias, C., Faria, H., Frazao, O., Viera, P. & Marques, A T., 2010. Manufacturing and testing composite overwrapped pressure vessels with embedded sensors. *Mater des*, pp. 406-421.

Fu, J., Yun, J. & Jung, Y., 2016. Filament winding path generation based on inverse process of stability analysis for non-axisymmetric mandrels. *Journal of composite matter*, pp. 78-89.

Gentileau, B., Bertin, M., Touchard, F. & Grandidier, J. C., 2011. Stress analysis in specimens made of multi-layer polymer/composite used for hydrogen storage application: comparison with experimental results. *Composite Structures*, Volume 93, pp. 2760-2767.

Gentileau, B., Villalonga, F., Nony, H. & Galiano, H., 2015. A probabilistic damage behaviour law for composite material dedicated to a composite pressure vessel. *Internal journal of hydrogen energy*, Volume 13193-13205, p. 40.

Gentilleau, B., Magneville, B. & Villalonga, S., 2019. Modelling, parameters identification and experimental validation of composite materials behaviour law used in 700 bar type IV hydrogen high-pressure storage vessel. *Internal Journal Hydrogen Energy*, pp. 456-478.

Graham, J., 1993. Preliminary Analysis Techniques for Ring and Stringer Stiffened Cylinder Shells. *NASA Report TM-108399*, p. 5.

Gruber, M. F., Aslak, U. & Helix-Nielsen, C., 2016. Open-source CFD model for optimization of forward osmosis and reverse osmosis membrane modules. *Purif Technology*, pp. 183-192.

Hannus, S. & Majak, J., 2015. Orientational design of anisotropic materials using the hill and Tsai-Wu strength criteria. *Mechanics of Composite Materials*, Volume 39, pp. 6-28.

Hashin, Z., 2016. Failure criteria for unidirectional fibre composite. *Journal of Applied Mechanic*, pp. 329-334.

Hendlmeier, A; Marinovic, L; Al-Assafi, S; Stojcevski, F; Henderson, L C, 2019. Sizing effects on the interfacial shear strength of carbon fibre reinforced two-component thermoplastic polymer. *Composite Part A: Applied Science and Manufacturing*, p. 127.

Hua, T. Q., Ahluwalia, R. k. & Peng, J.-K., 2011. Technical assessment of compressed hydrogen storage tank systems for automotive application. *International Journal Hydraulic Energy*, pp. 37-49.

Hwang, T., Hong, C. & Kim, C., 2003. Size effect on the fibre strength of composite pressure vessels. *Composite Structure*, pp. 489-498.

Jerome, M., Plassard, F., Hereil, P. L. & Thiot, P., 2015. Numerical investigations of Hypervelocity impacts on pressurized aluminium-composite vessels. *Procedia Engineering*, Volume 103, pp. 373-380.

- Jones, R. M., 2020. Mechanics of composite material. *McGraw-Hill New York*, pp. 56-78.
- Kam, T., Liu, Y. & Lee, F., 2000. First-ply failure strength of laminated composite pressure vessels. *Composite Structure*, pp. 65-70.
- Liao, B. B. & Jia, L. Y., 2018. Finite element analysis of dynamic responses of composite pressure vessels under low-velocity impact by using a three-dimension laminated media model. *Thin-walled structures*, Volume 129, pp. 488-501.
- Liu, P. C. J. H. S., 2016. Numerical simulation and optimal design for composite high-pressure hydrogen storage vessel. *Renew Sustain Energy*, pp. 37-98.
- Ma, R; Li, W; Huang, M; Liu, X; Feng, M, 2018. Enhancing strength and toughness composites with low fibre content. *Polymer Testing*, Volume 71, pp. 156-162.
- Mechael, A., Emmanuel, C., Conteh & Nsofor, 2016. A symmetric angle-ply composite flywheel for high-speed energy storage. *Journal of Engineering Materials and Technology*, Volume 138, pp. 50-62.
- Mian, H. H., Wang, G. & Dar, U. A., 2020. Optimization of composite material system and lay-up to achieve minimum weight pressure vessel. *Application of Composite Mater*, pp. 873-889.
- Mitrevski, T. et al., 2018. The effect of impactor shape on the impact response of composite laminates.. *Composite Structure*, pp. 169-177.
- Murthy, P. L., 2017. Stress Rupture Life Reliability Measures for Composite Overwrapped Pressure Vessels. *Structure Dynamics and Material Conference*, pp. 50-62.
- Onder, A., Sayman, O., Dogan, T. & Tarakcioglu, N., 2018. Burst failure load of composite pressure vessels. *Composite Structures*, pp. 159-166.
- Paepegem, V. & Dgriek, J., 2015. Calculation of damage-dependent directional failure indices from the Tsai-Wu static failure criterion. *Composites Science and Technology*, Volume 63, pp. 305-310.
- Paknahad, A. & Nourani, R., 2016. Mix model of FE method and IPSO algorithm for dome shape optimization of articulated pressure vessels considering the effect of non-geodesic trajectories. *Journal Engineering(India): Series C (Mech, Prod, Aerosp Mar Eng)*, pp. 151-158.
- Parnas, L. & Katirci, N., 2020. Design of fibre-reinforced composite pressure vessels under various loading conditions. *Composite Structure*, pp. 83-95.
- Paul, G. & Mathews, M., 2015. *Design of experiments for engineers and scientists*. s.l.:Elsevier science & Technology books.

Pedro, J., Ramirez, B., Damien, H., Grandidier, J C., Villalonga, S. & Nony, F., 2015. 700 bar type IV high-pressure hydrogen storage vessel burst simulation and experimental validation. *International journal of hydrogen energy*, Volume 40, pp. 13183-13192.

Perl, M. & Saley, T., 2017. Swage and Hydraulic Autofritage Impact on Fracture Endurance and Fatigue Life of an Internally Barrel. *Effect of Overstraining*, Volume 50, pp. 2-29.

Pimenta, S., 2015. Toughness and strength of recycled composites and their virgin precursors. *Imperial College London*; pp. 125-156.

Porter, M. C., 1990. Handbook of industrial membrane technology. *Noyes Park Ridge*, pp. 34-45.

Reid, S. & Zhou, G., 2000. impact behaviour of fibre-reinforced composite materials and structures. *Woodhead Publishing Limited*, pp. 158-160.

Rezakazemi, M., Shahverdi, M., Shirazian, S., Mohammadi, T. & Pak, A., 2017. CFD simulation of water removal from water/ethylene glycol mixtures by pervaporation. *Chemical Engineering Journal*, pp. 183-192.

Sabour, M. H. & Foghani, M. F., 2010. Design of semi-composite pressure vessel using fuzzy and FEM. *Application of Composite Mater*, pp. 175-182.

Sayman, O., 2005. Analysis of multi-layered composite cylinders under hygrothermal loading. *Composites Part A*, pp. 923-933.

Shanmugavel, M. V. T., 2014. Finite element analysis of burst pressure of composite storage vessels. *Journal Mechanical & Civil Engineering*, pp. 73-80.

Sonnen, M., Laval, C. & Seifert, A., 2004. Computerized calculation of composite laminates and structures. *Theory and Reality Material*, pp. 56-67.

Sulaiman, S., Borazjani, S. & Tang, S. H., 2015. Finite element analysis of filament-wound composite pressure vessel under internal pressure. *Material Science and Engineering*, pp. 757-899.

Sun, X., Du, S. & Wang, G., 2019. Bursting problem of filament wound composite pressure vessels. *International Journal Pressure Vessels Piping*, pp. 55-59.

Vasiliev, V. V. & Jones, R., 2018. Composite Pressure Vessels. *Analysis, Design and Manufacturing*, pp. 30-56.

Venkatesan, G., Kulasekharan, N. & Iniyan, S., 2015. Design and selection of curved vane demisters using Taguchi based CFD analysis. *Desalination*, pp. 39-52.

Yarrapragada, R. K., 2017. Composite pressure vessels. *Internal journal of research in engineering and technology*.

Investigating Effects of Preparation Parameters on Mechanical Performance of PBAC2-co-PM52 Copolyoxamide/Carbon Fiber Reinforced Composites

Fredrick Nzioka Mutua^{a*}, and Yong He^b

^a School of Mechanical and Manufacturing Engineering, Technical University of Kenya, P.O. Box 52428-00200, Nairobi, Kenya

^b Innovation Center for Textile Science and Technology; State Key Laboratory for Modification of Chemical Fibers and Polymer Materials, College of Materials Science and Engineering, Donghua University, Shanghai 201620, China

Abstract

Polyoxamides are characterized by superior mechanical, chemical, Ultra-Violet (UV) light resistance and low water absorption properties than conventional polyamides. In this study, a novel in-situ spray polycondensation is explored for impregnating poly(1,3-bis(aminomethyl) cyclohexamethylene oxamide)-co-poly(2-methyl-1,5-pentamethylene oxamide)(PBAC2-co-PM52) copolyoxamide prepolymer into Carbon Fibers (CF) for fabrication of recyclable composites. The effects of preparation parameters on the mechanical properties of PBAC2-co-PM52/CF composites are studied and reported. The composites prepared at molding temperature of 315°C, pressure of 2.5 MPa and time of 15mins exhibits good tensile strength at break, flexural strength and ILSS of 551 MPa, 482 MPa and 68 MPa, respectively. SEM results suggest good adhesion between the resin and CF, depicting the potential of in-situ spray impregnation in preparation of carbon fiber reinforced polyoxamide composites.

Key words: Polyoxamides, PBAC2-co-PM52, CF composites, impregnation, mechanical properties

1. Introduction

Polyoxamides have the shortest diacid-unit in the main chain and are characterized by a high concentration of amides. Their outstanding properties include high melting point (Gaymans, Venkatraman, & Schuijjer, 1984; Kouichiro Kurachi, 2011; Shalaby, Pearce, Fredericks, & Turi, 1973; Stamatoff & Symons, 1966), high modulus, excellent chemical resistance(Nakagawa, Maeda, Nozaki, & Yamamoto, 2014; Nakagawa, Nozaki, Maeda, & Yamamoto, 2015) and very low saturated water absorption(Kouichiro Kurachi, 2011; Vogl & Knight, 1968a). For these reasons, they have been attracting the attention of scientists for a long time(Casas, Armelin, Alemán, & Puiggali, 2002; Chatani, Ueda, Tadokoro, Deits, & Vogl, 1978; Dickstein & Vogl, 1984; Franco, Subirana, & Puiggali, 1998; Gaymans et al., 1984; Koichiro Kurachi, Hanaoka, Maeda, & Okushita, 2012; Maeda et al., 2012; Nakagawa et al., 2015; Wang, Nomura, & Endo, 1997).

* Corresponding author

E-mail address: fredrick.mutua@tukenya.ac.ke (F.Mutua)

A couple of preparation techniques for polyoxamides have previously been reported (Chang & Vogl, 1977b, 1977a; Dickstein & Vogl, 1984; Gaymans et al., 1984; Grossman & Vogl, 1980; Vogl & Knight, 1968a, 1968b). Preparation methods for conventional polyamides have been reported to result in low molecular polyoxamides (Vogl & Knight, 1968a, 1968b). For example, melt polycondensation has been found to result in thermal decomposition of both the oxalic acid and the resultant prepolymers (Vogl & Knight, 1968b). Thermal decomposition has also been reported to cause low-molecular weight polymers during ring-opening polymerization of cyclic oxamides (Vogl & Knight, 1968b). Rapid hydrolysis of oxalyl chloride during Liquid-liquid interfacial polycondensation results in low molecular weight polyoxamides. However, gas-liquid interfacial polymerization was reported to produce appreciable molecular weight polyoxamide stretchable into fibrous form (Chatani et al., 1978). A high molecular poly(nonamethylene oxamide) (PA92) (Okushita, Kurachi, & Shimokawa, 2008) was recently prepared by prepolymerizing oxalic ester and diamine in solvent followed by melt-polymerization under pressure.

Recently, spray polycondensation was successfully developed and used in preparation of high molecular weight novel polyoxamides such as poly(2-methyl-1,5-pentamethylene oxamide) (PM52) (Mutua, Gao, Yang, Zhu, & He, 2018) and poly(1,3-bis(aminomethyl) cyclohexamethylene oxamide) (PBAC2) (Mutua, Yang, Gao, Zhu, & He, 2018) which exhibited excellent crystallizability, thermal stability and very low water absorption.

General commercial polyamides have good mechanical properties, are easy to handle, and are relatively cheaper, they exhibit high water absorption which compromises their mechanical performance. Further, they are not easy to impregnate into carbon fibers and are therefore not very attractive resins for use in composite materials (Pillay, Vaidya, & Janowski, 2009; Tanaka, Mizuno, Honda, Katayama, & Enoki, 2013). Polyoxamides are a class of thermoplastic resins that exhibit good mechanical properties, chemical, UV light resistance and low water absorption properties than conventional polyamides, but there are minimal works on their use as resins in thermoplastic composite materials (Tanaka, Maehata, Katayama, & Shinohara, 2015). The primary challenge associated with thermoplastics is that they are usually in solid state at room temperature, have high melt viscosities and are thus difficult to impregnate into fibers (Manson, 2012). Though research has born many approaches to address this challenge, the potential of thermoplastic composites has not yet been fully exploited (Gibson & Manson, 1992). If polyoxamide resins could be successfully impregnated into carbon fibers, they may address the environmental challenges as well as costs associated with impossibility of re-melting and reshaping of cured thermoset, which would also provide an avenue for application of carbon fiber reinforced composites in mass-produced vehicles that increasingly require the use of recyclable materials due to environmental concerns (Offringa, 1996).

After exploring the properties of PM52 and PBAC2, it was found that PBAC2 had a high melting temperature of about 318°C (Mutua, Yang, et al., 2018) while PM52 had a low melting point of 200 °C (Mutua, Gao, et al., 2018). The two homopolymers were therefore copolymerized to synthesize a new copolymer of PBAC2-co-PM52 using BAC, M5 and DBO via spray polycondensation to develop a copolymer with appropriate properties for use as matrix for composites. In-situ spray impregnation was then proposed and used to impregnate PBAC2-co-PM52(70/30) into Carbon fibers followed by SSP and vacuum compression molding to prepare composite materials.

2. Experimental Materials

1,3-bis(aminomethyl) cyclohexane (BAC, >99.5 wt%), 2-methyl-1,5-pentanediamine (M5), dibutyl oxalate (DBO, >99.0% (GC)), were purchased from TCI Shanghai, China. Carbon fiber fabric (3K-T300 plain) was received from Toray industries, Inc. All the chemicals were used without further purification.

In most cases carbon fiber fabrics (CFs) are used in the manufacture of composite materials using thermoset resins such as epoxy. The carbon fibers used in the current work were coated with bisphenol A epoxy type sizing agent. The CFs were therefore desized to avoid the formation of voids at the consolidation temperatures (higher than 300°C in this study) due to known degradation of the sizing agents at temperatures above 250 °C.

3. Impregnation procedure

An XY stage concept was incorporated for precise movement of a determined point of the carbon fiber fabric along a straight line in the X and Y axis for uniform impregnation of the CFs via in-situ spray polycondensation.

The schematic and real presentation of the setup are shown in Figure 1.

The stage offers travel lengths from 50mm to 200mm in both X and Y directions via end of travel limit switches. The limit switch and motor cables are terminated by a 9 pin connector near the rear of the stage next to the motor. The drive system utilizes a stainless leadscrew with internally lubricated plastic drive nut. The drive nut offers zero backlash operation that automatically adjusts for wear to ensure zero backlash for the life of the stage as this is important for precise and uniform impregnation of the CFs with PBAC2-co-PM52(70/30) resin.

Prior to impregnation, the sizing agent on the carbon fiber fabric was removed by refluxing in acetone for 24 hours, rinsed three times and then dried in vacuum oven overnight at 80 °C. The dried carbon fiber fabric was cut into pieces of 200mm by 150mm in size, one piece was placed inside a sample holder on the XY stage for each impregnation cycle. The two monomers at stoichiometric molar ratio of 1/1 (flowrates of 172.4 µl/min for BAC/M5 and 232.6µl/min for DBO) were simultaneously mixed under

atomizing action of a well-controlled nitrogen flow of 3.4 L/min at room temperature ($\approx 25\text{-}30^\circ\text{C}$) at the tips of the two needles of 26G, which were tightly fastened and placed at the center of the nozzle (diameter 1.6mm).

At the same time of mixing, polycondensation of the monomers occurred and a white prepolymer powder was deposited on the carbon fiber substrate placed on the mobile XY stage with respect to the stationary needle tips (Figure 1B). The XY stage was moving at a rate of 1mm/sec in a straight line along the X axis for a distance of 200mm after which it made a 1 cm Y axis stroke at a rate of 1mm/sec, these speed rates were found to provide a uniform impregnation of the prepolymer on the carbon fiber in both directions at any given time. A complete cycle was made when the stage had covered a distance of 150mm in the Y direction after which the whole cycle was repeated until the desired amount of prepolymer was uniformly impregnated on both sides of the carbon fiber fabric. Even though the X-Y stage could travel at higher speeds, it was found that a speed of 1mm/sec led to uniform impregnation of PBAC2-co-PM52 (70/30) on CF after several trials.

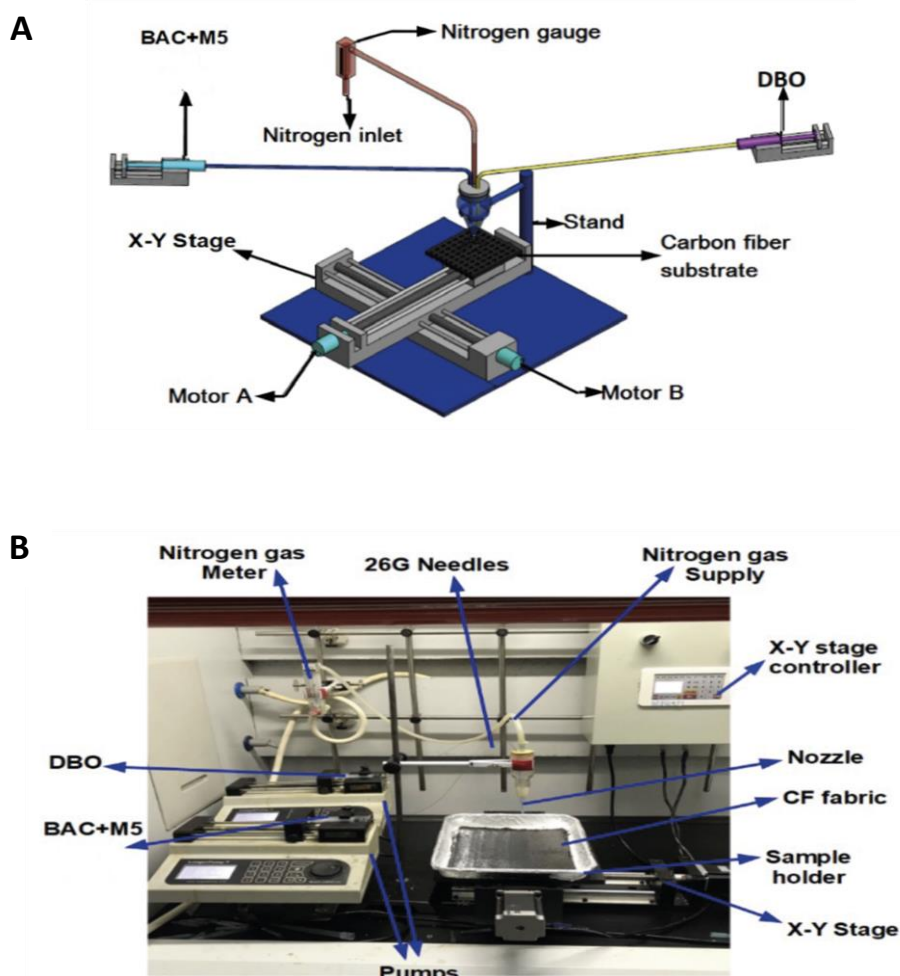


Figure 16. Impregnation setup: (a) schematic representation and (b) real set up

4. SSP and compression molding

After impregnation of CF with PBAC2-co-PM52 (70/30) prepolymer, aging was carried out in a vacuum oven overnight at a temperature of about 60 °C. Solid state polycondensation (SSP) was then carried out as shown in Figure 2 for 1.5 hours at 270 °C in vacuum to increase the molecular weight of PBAC2-co-PM52 (70/30). After SSP, the resin impregnated laminates were ready for fabrication of carbon fiber composites.



Figure 17. SSP setup after impregnation

The composite laminate consolidation process using the vacuum compression molding was carried out in a stainless steel mold with dimensions of 200 by 150 mm. Firstly, the composite laminate was heated up at 10 °C /min to the melting temperature of 297 °C for PBAC2-co-PM52(70/30) and held at this temperature for 10 minutes. Afterwards, the composite laminate was heated up to the desired processing temperature of (310 °C, 315 °C or 320 °C) at 10 °C/min and then consolidated at this temperature under pressures of 2.0 MPa, 2.5 MPa or 3.0 MPa then held for molding times of 10 minutes, 15 minutes or 20 minutes. The mold was then cooled to room temperature in air and the composites were removed from the mold. The composite fabrication cycle is summarized in Figure 3. For this study, the resin mass fraction was maintained at about 40wt% at the impregnation stage.

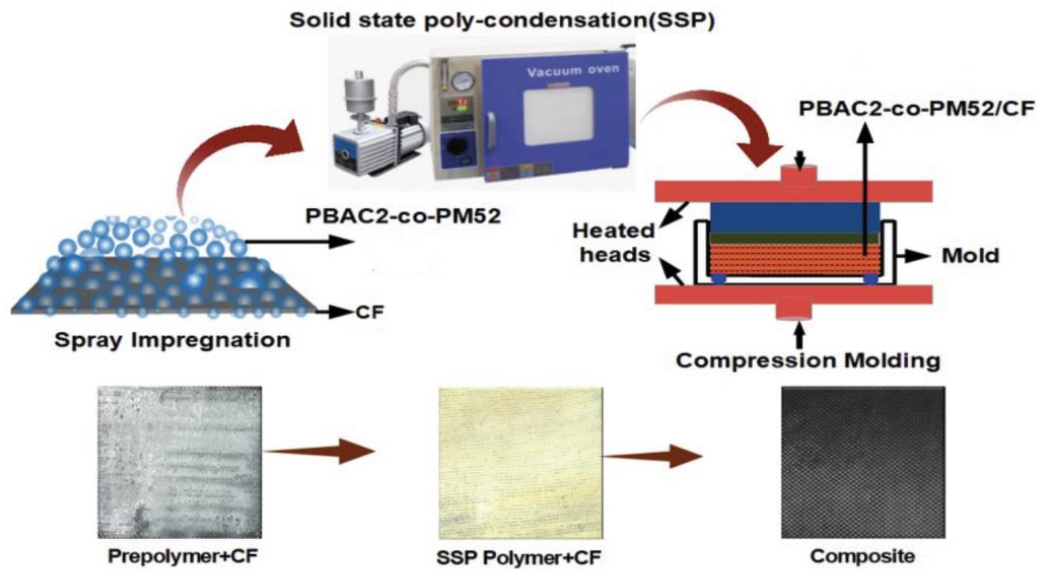


Figure 18. PBAC2-co-PM52/CF composite fabrication cycle as per the red arrows

5. Analysis

Morphologies of PBAC2-co-PM52/CF composites were observed using a scanning electron microscope (SEM) (HITACHI S-300N, Japan) with an acceleration voltage of 15–18 kV while metalloscopy images were obtained using Olympus BX41M-LED microscope (Japan). Tensile tests were performed using a computer controlled Instron universal testing machine. Tensile strength, modulus, strain at break and flexural strength values of the composites were determined at a constant crosshead speed of 5 mm/min. Dynamic mechanical analysis (DMA) tests were carried out on a thermal dynamic mechanical analyzer (TA Q800, USA) using three-point bending mode. The samples were tested at a frequency of 1.0 Hz and a heating rate of 10°C/min, for a temperature range of 25–250°C. Interlaminar shear strength (ILSS) of composites were determined on a universal testing machine (LABSANS LD26.105, China) following ASTM D7264 standards. Five parallel measurements were conducted and averaged for each final result reported. Error bars indicated the standard deviation.

6. Results and discussion

Influence of process parameters on PBAC2-co-PM52/CF composite tensile strength

To understand the mechanical performance of the fabricated composites, difference mechanical properties were studied and the results reported. Figure 4 show the influence of processing parameters on the tensile strength at break of the prepared PBAC2-co-PM52/CF composites and the values are summarized in Table 1. The results show that consolidation times of 10 and 20 minutes at constant temperature (315°C) and pressure (2.5 MPa) resulted in PBAC2-co-PM52/CF composites having the same tensile strength at break as summarized in Table 1.

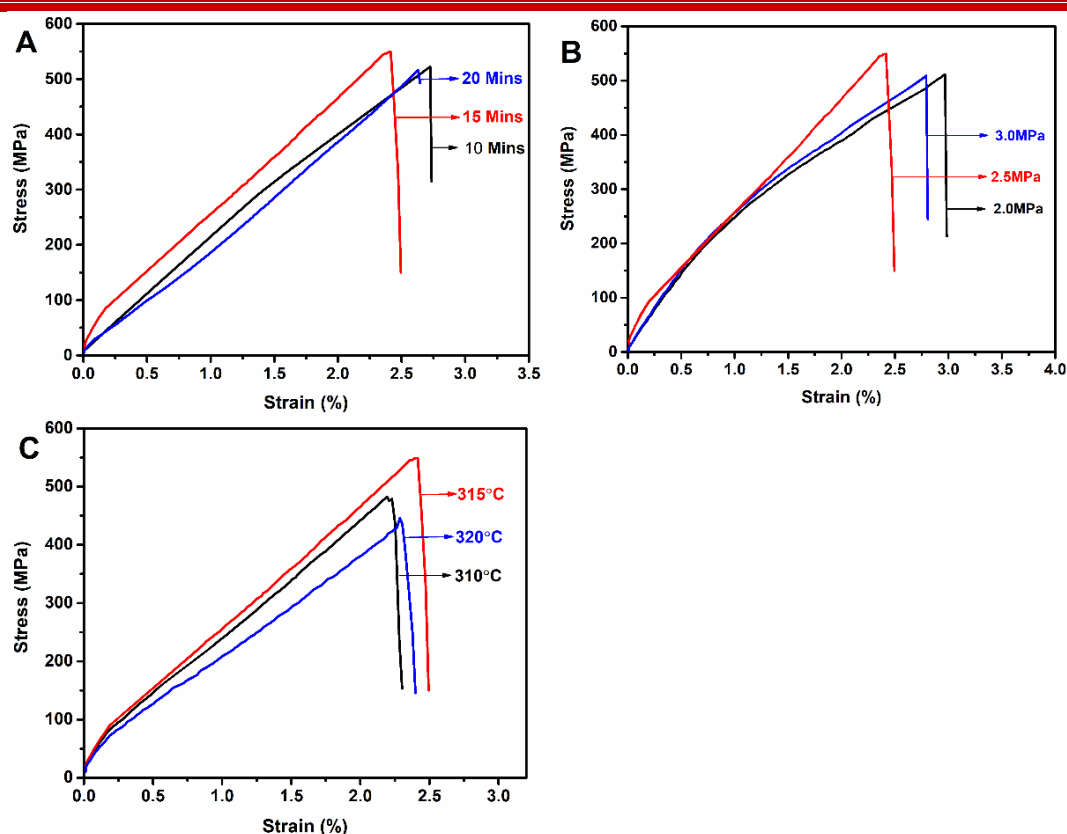


Figure Error! No text of specified style in document.. Tensile properties of PBAC2-co-PM52/CF prepared at different processing (a) time at 315 °C, 2.5 MPa; (b) pressure at 315 °C, 15 minutes; (c) temperature for 15 minutes, 2.5 MPa

When the processing pressure and time were held at 2.5 MPa and 15 minutes, respectively, a processing temperature of 315°C resulted in composites with the highest tensile strength at break of the three fabrication temperatures explored. It is worth noting that under constant consolidation temperature and time of 315°C and 15 minutes, respectively, the resultant composite's tensile strength at break was almost the same within a margin of error at consolidation pressure of 2.5(511±18 MPa) and 3.0 MPa(507±21 MPa), respectively. However, the strain at break of the composite was found to be highest at consolidation pressure of 2.0 MPa(3.0±0.1%), reduced at 2.5Mpa (2.4±0.3%) and increased again at 3.0Mpa (2.7±0.2%) at processing time and temperature of 15 minutes and 315°C. However, with the changes in processing parameter, the strains at break were almost the same with a margin of error.

Table 1. Summary of mechanical properties of PBAC2-co-PM52/CF composite prepared at different consolidation conditions

Entry	Moulding time (Mins)	Moulding pressure (MPa)	Moulding temperature (°C)	Tensile strength at break (MPa)	Strain at break (%)	Flexural strength at break (MPa)	Interlaminar shear strength (MPa)
1	10	2.5	315	519±28	2.7±0.2	448±22	62.1±3.1
2	20	2.5	315	519±26	2.6±0.3	472±24	66.7±3.3
3	15	2	315	511±18	3.0 ±0.1	452±23	61.2±3.0
4	15	3	315	507±21	2.7±0.2	465±23	64.6±3.2
5	15	2.5	310	481±20	2.2±0.3	446±22	63.5±3.1
6	15	2.5	315	551±24	2.4±0.3	482±24	68.3±3.4
7	15	2.5	320	444±28	2.3±0.4	450±23	65.2±3.3

The results also showed minimal variation in the resultant tensile properties of the composites at the consolidation pressures studied as seen in Figure 4b. These results indicate that a combination of the three process parameters (315°C, 15 minutes and 2.5 MPa) led to good penetration of PBAC2-co-PM52 into the CF bundles thus good wet out of the fibers which promoted efficient load transfer from the matrix to the reinforcing fibers resulting in improved mechanical properties of the resultant composites as seen in Figure 4c (551 MPa) as summarized in entry 6 of Table 1. This inference is further supported by the SEM micrograph shown in Figure 8 which indicate appreciable interface between the matrix and CF.

Influence of process parameters on composite flexural properties

The flexural properties of PBAC2-co-PM52/CF composites were also analyzed and presented in Figure 5 and summarized in Table 1. The analysis revealed that the flexural strength at failure of the samples prepared under 315 °C and 2.5 MPa (Figure 5A) were 472±24 MPa, (482±24 MPa) and 448±22 MPa at consolidation time of 20, 15 and 10 minutes, respectively. These results depict that the flexural strengths were the same with a small margin of error at consolidation times of 15 and 20 minutes which implies that preparation of the composites at consolidation times above 15 minutes didn't impart any changes in the composites flexural strength. Therefore, good wet out of the carbon fibers was achieved with 15 minutes of consolidation thus the higher flexural strength of the composite.

Similarly, upon increasing processing pressure at constant temperature and time of 315 °C and 15 minutes (Figure 5B), the flexural strength were 452±23 MPa at consolidation pressure of 2.0 MPa, 482±24 MPa at consolidation pressure of 2.5 MPa and 465±23 MPa after consolidation at 3.0 MPa indicating that the flexural strengths were almost the same. Further, increasing processing temperature at constant pressure and time of 2.5 MPa and 15 minutes (Figure 5C), was found to result in almost the same values of flexural strengths. Since increasing the process temperature directly increases the flowability of thermoplastic polymers, it was inferred that increased flow of the resin into the carbon fiber bundles was optimal at 315

°C, above which the resin was driven out of the carbon fiber interstices leading to a low resin fraction in the composite. Further, increasing the consolidation pressure leads to bundling of the carbon fibers during processing of the composites, these two factors could have resulted in non-uniformity of the composite and thus the reported slight variation in mechanical properties. It was therefore inferred that fabrication of the composite at 315 °C under consolidation pressure of 2.5 MPa for 15 minutes yielded the highest flexural strength (approximately 482 ± 24 MPa) in the current study. This could be explained through a high volume of the resin having remained well adhered within the fiber bundles as depicted in the SEM micrographs in Figure 8.

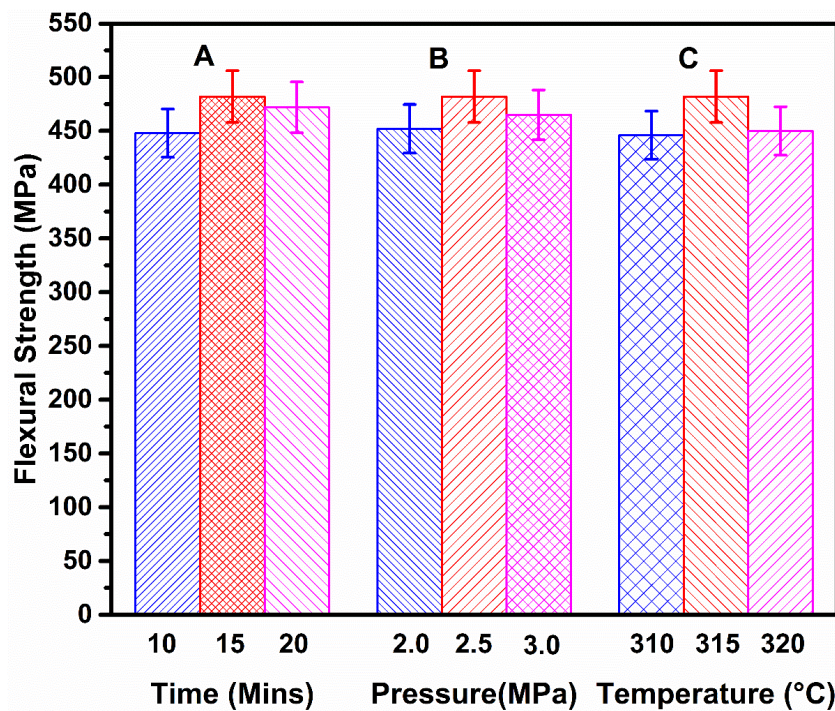


Figure 5. Flexural strength of composites fabricated under varying processing (a) time at 315 °C, 2.5 MPa; (b) pressure at 315 °C, 15 minutes; (c) temperature at 2.5 MPa, 15 Minutes

Influence of process parameters on composite interlinear shear strength

The interlaminar shear strength (ILSS) of PBAC2-co-PM52/CF composites were also studied and presented in Figure 6 and summarized in Table 1. Upon varying the consolidation time from 10 to 20 minutes at constant temperature (315 °C) and pressure (2.5 MPa), the ILSS values were found to be 62.1 ± 3.1 , 66.7 ± 3.3 and 68.3 ± 3.4 MPa after 10, 15 and 20 minutes of consolidation, respectively (Figure 6A), as shown in Table 1 indicating that the ILSS values of the composites were almost the same in the error range at 15 and 20 minutes of consolidation. Similarly, when the processing temperature and time were held at 315 °C and 15 minutes (Figure 6B), the ILSS values of the prepared composite were 61.2 ± 3.0 ,

68.3±3.4 and 64.6±3.2 MPa after consolidation at pressures of 2.0, 2.5 and 3.0 MPa, respectively, indicating no changes in ILSS at consolidation pressure of above 2.5MPa.

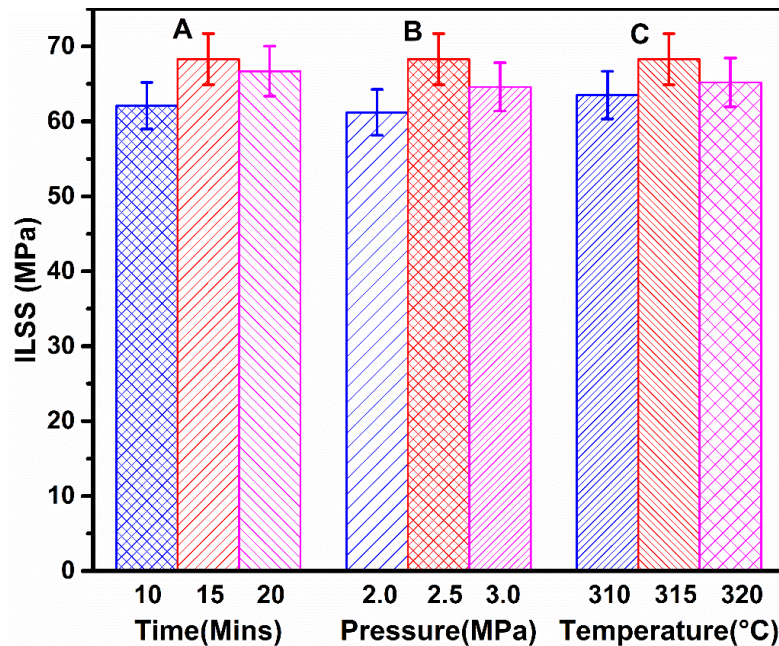


Figure 6. Interlaminar shear strength (ILSS) of composite prepared under varying processing (a) time at 315 °C and 2.5 MPa; (b) pressure at 315 °C and 15 minutes; (c) temperature at 2.5 MPa and 15 minutes

Further, under increasing process temperature (Figure 6C) at constant pressure of 2.5 MPa and 15 minutes of consolidation, the ILSS values were of 63.5±3.1, 68.3±3.4 and 65.2±3.3 MPa at 310, 315 and 320 °C, respectively. These results indicate that the three consolidation parameters (time, pressure and temperature) had little influence on the ILSS results of the composites above 2.5 MPa, 315 °C and 15 minutes of consolidation. Under these compression molding parameters (315 °C, 2.5 MPa and 15 minutes) a composite having an ILSS of about 68.3±3.4 MPa was fabricated. These processing parameters resulted in the highest tensile stress at break, flexural and strain at break values and are therefore were considered optimal for this initial work on in-situ spray impregnated PBAC2-co-PM52/CF composites. This is because, at 310 °C, the flowability of the resin into the carbon fiber bundles was not high enough for good wet-out, this increased at 315 °C leading to composites having high ILSS. At 320 °C, the flowability of the resin was so high and most of the lot of resin was squeezed out of the carbon fibers during compression molding resulting in composites with low ILSS.

Dynamic mechanical analysis

The results of DMA test of the fabricated PBAC2-co-PM52/CF composites revealed a high storage modulus as a function of temperature traced in DMA as shown in Figure 7. At temperatures above glass transition temperature of PBAC2-co-PM52 (T_g , ~150°C), the composite had high storage modulus, which

indicates that, these composites are well suited for high temperature application because the T_g , is ideally considered as the upper limit for structural application of polymeric composites (Goertzen & Kessler, 2007).

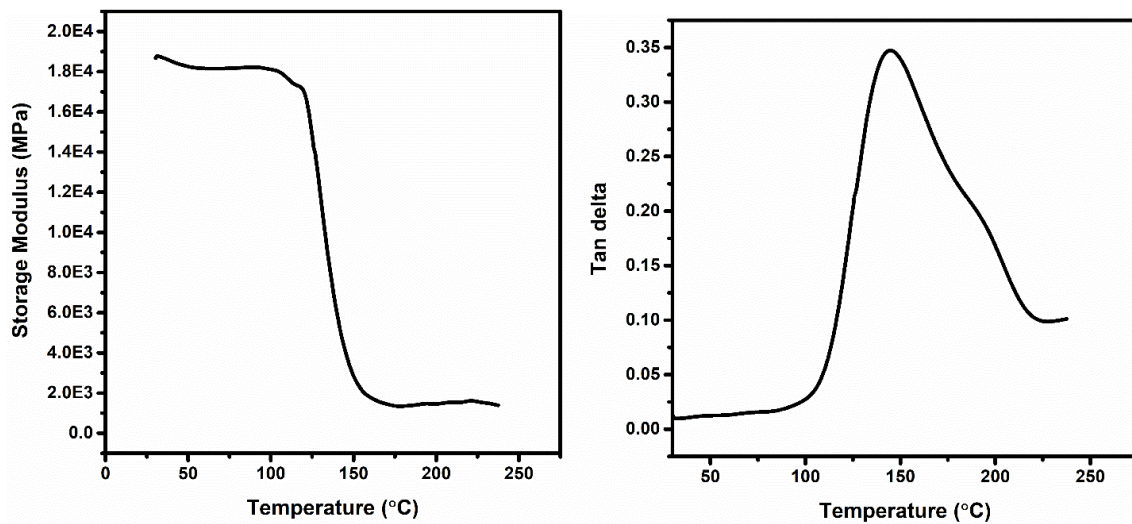


Figure 7. The storage modulus and Tan delta for PBAC2-co-PM52/CF composite processed at 315 °C, 15 minutes and 2.5 MPa

Fiber matrix interface

Fiber reinforced composites exhibit properties which are superior to those of their pure components. However, the mechanical performance of composites depend on the interface between the fiber and the matrix. Good interfacial adhesion promotes load transfer from the matrix to reinforcement, and is a core requirement for the exploitation of the reinforcement properties. To this end, the cracked surfaces of PBAC2-co-PM52/CF composites were observed under SEM to elucidate the existence of an interface between the fiber reinforcements and the matrix material as it contributes to the overall mechanical behavior and capabilities of the composite materials. The SEM micrographs shown in Figure 8 revealed a good adhesion between the resin which was determined from the fibers being well coated and uniformly distributed within the resin seen in the micrographs.

The arrows on the SEM indicate the good adhesion between the fibers and the matrix as well as some of the noticeable faults in the fabricated composite including de-bonding, matrix cracking and some minimal voids. The arrows also show adhesion between the fibers and the matrix as well as some fibers well embedded in the matrix.

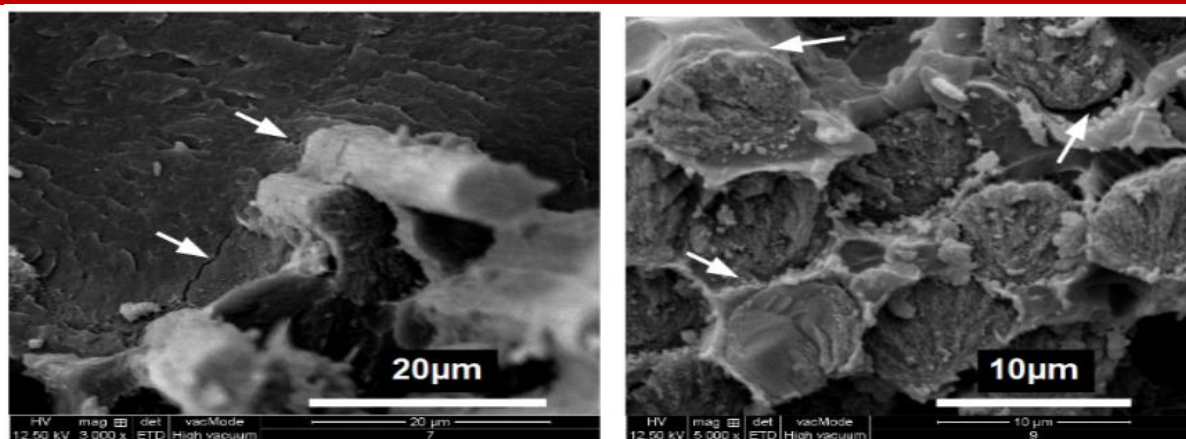


Figure 8. SEM micrographs of PBAC2-co-PM52/CF composite processed at 315 °C, 15 minutes and 2.5 MPa (Cross-sectional section at 3000X and 5000X)

The mechanical properties of prepared PBAC2-co-PM52-CF composites were compared with literature data for PA6-CF composite (Botelho, Rezende, & Lauke, 2003; Pillay et al., 2009) and the results presented in Table 2. It was found that, PBAC2-co-PM52/CF composites had higher tensile strength, strain as well ILSS than PA6/CF composite but its flexural strength was higher than that of the composite prepared in the current study. The high ILSS values of the composites prepared in this study predict good interface between the fibers and the resins which is supported by the SEM micrographs in Figure 8.

Table 2. Comparison of the mechanical properties of PA52/CF, PBAC2-co-PM52/CF and PA6/CF composites

Property	Composite	
	PBAC2-co-PM52/CF ^b	PA6/CF[22, 31]
Tensile strength (MPa)	551.0±24	410±32
Strain (%)	2.4±0.3	0.8
Flexural strength (MPa)	482±24	642
ILSS(MPa)	68.3±3.4	27.0

Prepared at ^b (315 °C, 15 minutes and 2.5 MPa)

7. Conclusion

PBAC2-co-PM52/CF composites were prepared successfully after spray impregnation and SSP. The results indicated that;

- I. The prepared composites had appreciable tensile strength (551.0±24), flexural strength as well as ILSS. These predicts a good adhesion of the PBAC2-co-PM52 to the CF as seen from the cross-section SEM micrographs while DMA studies revealed a high glass transition temperature for the

prepared composites. Since the resin used for fabrication of composites in this study had a T_g above 100 °C (i.e. 150 °C),

- II. It is safe to say that the prepared composites are well suited for high temperature application because it registered high storage modulus at or below its T_g above which the mechanical properties of the prepared composites would be expected to deteriorate sharply, indicating that the prepared polyoxamide resins have high, well aligned polymer chains with low mobility.
- III. Considering that no other surface modification was carried out other than removal of the surface coatings on the carbon fibers, the mechanical properties as well as the cross-sectional SEM views are a strong basis for consideration of spray in-situ impregnation of carbon fibers with polyoxamide resins. However, more work on PBAC2-co-PM52/CF composites need to be carried out to optimize the process.

References

- Botelho, E. C., Rezende, M. C., & Lauke, B. (2003). Mechanical behavior of carbon fiber reinforced polyamide composites. *Composites Science and Technology*, 63(13), 1843–1855.
- Casas, M. T., Armelin, E., Alemán, C., & Puiggali, J. (2002). On the crystalline structure of even polyoxalamides. *Macromolecules*, 35(23), 8781–8787.
- Chang, H. J., & Vogl, O. (1977a). Regular copolyamides. I. A facile method for the preparation of diamine-oxamides. *Journal of Polymer Science: Polymer Chemistry Edition*, 15(2), 311–322. doi:10.1002/pol.1977.170150205
- Chang, H. J., & Vogl, O. (1977b). Regular copolyamides. II. Preparation and characterization of regular aliphatic copolyoxamides. *Journal of Polymer Science: Polymer Chemistry Edition*, 15(5), 1043–1060. doi:10.1002/pol.1977.170150503
- Chatani, Y., Ueda, Y., Tadokoro, H., Deits, W., & Vogl, O. (1978). Structure of Poly(hexamethylene oxamide) [Nylon 62]. *Macromolecules*, 11(4), 636–638. doi:10.1021/ma60064a003
- Dickstein, W., & Vogl, O. (1984). Regular copolyamides. IX. Some aliphatic aromatic copolyoxamides. *J. Macromol. Sci., Chem.*, A21(6–7), 847–857. doi:10.1080/00222338408077247
- Franco, L., Subirana, J. A., & Puiggali, J. (1998). Structure and Morphology of Odd Polyoxamides [Nylon 9,2]. A New Example of Hydrogen-Bonding Interactions in Two Different Directions. *Macromolecules*, 31(12), 3912–3924. doi:10.1021/ma971599z
- Gaymans, R. J., Venkatraman, V. S., & Schuijjer, J. (1984). Preparation and Some Properties of Nylon-4,2. *Journal of Polymer Science: Polymer Chemistry Edition*, 22(6), 1373–1382.
- Gibson, A. G., & Manson, J. A. (1992). Impregnation technology for thermoplastic matrix composites. *Composites Manufacturing*, 3(4), 223–233.

- Goertzen, W. K., & Kessler, M. R. (2007). Dynamic mechanical analysis of carbon/epoxy composites for structural pipeline repair. *Composites Part B: Engineering*, 38(1), 1–9.
- Grossman, S., & Vogl, O. (1980). Regular copolyamides by solution and liquid-liquid interfacial polymerization. *Org. Coat. Plast. Chem.*, 42, 116–121.
- Kurachi, Koichiro, Hanaoka, Y., Maeda, S., & Okushita, H. (2012). JP Patent 2012072200A. Ube Industries, Ltd., Japan.
- Kurachi, Kouichiro. (2011). C1 chemistry-derived high performance polymers. Focus on polyoxamide. *Purasuchikkusu Eji*, 57(1), 72–76.
- Maeda, S., Kurachi, K., Okushita, H., Hanaoka, Y., Yabu, N., & Nakagawa, T. (2012). WO 2012036303A1. UBE Industries, Ltd., Japan.
- Manson, J.-A. (2012). HIVOCOMP: large-scale use of carbon composites in the automotive industry. *Reinforced Plastics*, 56(6), 44–46.
- Mutua, F. N., Gao, Y., Yang, T., Zhu, B., & He, Y. (2018). Preparation and characterization of poly(2-methyl-1,5-pentamethylene oxamide) (PM52) polymer. *Polymers for Advanced Technologies*, 29(6). doi:10.1002/pat.4266
- Mutua, F. N., Yang, T., Gao, Y., Zhu, B., & He, Y. (2018). Preparation, analysis, and isothermal crystallization behavior of poly[1,3-bis(aminomethyl)cyclohexamethylene oxamide]. *Journal of Applied Polymer Science*, 135(23). doi:10.1002/app.46345
- Nakagawa, T., Maeda, S., Nozaki, K., & Yamamoto, T. (2014). Crystal structure of an aliphatic polyoxamide containing methyl side-groups: Poly(2-methyl-1,8-octamethyleneoxamide). *Polymer*, 55(9), 2254–2261. doi:10.1016/j.polymer.2014.03.009
- Nakagawa, T., Nozaki, K., Maeda, S., & Yamamoto, T. (2015). Polymorphism of poly(nonamethyleneoxamide) crystal. *Polymer*, 57, 99–104. doi:10.1016/j.polymer.2014.12.022
- Offringa, A. R. (1996). Thermoplastic composites—rapid processing applications. *Composites Part A: Applied Science and Manufacturing*, 27(4), 329–336.
- Okushita, H., Kurachi, K., & Shimokawa, M. (2008). WO2008123531. Ube Industries, Ltd., Japan.
- Pillay, S., Vaidya, U. K., & Janowski, G. M. (2009). Effects of moisture and UV exposure on liquid molded carbon fabric reinforced nylon 6 composite laminates. *Composites Science and Technology*, 69(6), 839–846.
- Shalaby, S. W., Pearce, E. L. I. M., Fredericks, R. J., & Turi, E. A. (1973). Structure and Thermal Stability of Aliphatic Polyoxamides. *Journal of Polymer Science: Polymer Physics Edition*, 11(1), 1–14.
- Stamatoff, G. S., & Symons, N. K. J. (1966). U.S. Patent 1966, 3,247,168. E. I. du Pont de Nemours & Co. .
- Tanaka, K., Maehata, S., Katayama, T., & Shinohara, M. (2015). *Effect of Hot Water Environment on Tensile Fracture Properties of Carbon Fiber Reinforced Polyoxamide Composites*. In *Key Engineering Materials* (Vol. 627, pp. 177–180). Trans Tech Publ.

- Tanaka, K., Mizuno, S., Honda, H., Katayama, T., & Enoki, S. (2013). Effect of water absorption on the mechanical properties of carbon fiber/polyamide composites. *Journal of Solid Mechanics and Materials Engineering*, 7(5), 520–529.
- Vogl, O., & Knight, A. C. (1968a). Polyoxamides. I. Preparation and characterization of cyclic oxamides. *Macromolecules*, 1(4), 311–315. doi:10.1021/ma60004a006
- Vogl, O., & Knight, A. C. (1968b). Polyoxamides. II. Polymerization of cyclic diamides. *Macromolecules*, 1(4), 315–318. doi:10.1021/ma60004a007
- Wang, J., Nomura, R., & Endo, T. (1997). One-pot syntheses of water-soluble poly(oxamide)s. *Polym. Bull. (Berlin)*, 38(2), 125–132. doi:10.1007/s002890050028

Optimal shell thickness for Overwrapped Composite High-Pressure Vessels

Nathan Numbi Mukala¹

Leonard M Masu²

Patrick K Nziu¹

ORCID: 0000-0002-9900-5295

ORCID: 0000-0002-8544-6321

ORCID: 0000-0002-5899-0700

¹Vaal University of Technology, Faculty of Engineering and Technology, Department of Industrial Engineering & Operational Management and Mechanical Engineering, Vanderbijpark, Andries Potgieter Blvd, 1911, South Africa

² Technical University of Kenya, Faculty of Engineering and the Built Environment, School of Mechanical and Manufacturing Engineering, Department of Mechanical and Mechatronic Engineering, Haile Selassie Avenue, P.O. Box 52428 00200 Nairobi

Abstract

The purpose of this study was to determine the effects of shell thickness on bursting strength in composite pressure vessels using analytical method. The optimal range of fibre thicknesses were therefore determined to achieve improved sustainable composite pressure vessel.

The analytical evaluation was performed using the Tsai-Wu failure criteria to developed analytical equations which were solved with Matlab 2016 software to determine shell thickness. Upon vessel liner variation, a total of 28 generated parts were created on two profiles, in order generation of a vessel resistant to bursting failure. Henceforth, the shell thickness overwrapping the liner, being as well an influential factor to the vessel integrity, was, therefore, analyzed on symmetrical and asymmetrical lamination patterns. The optimal shell thickness range were thereafter determined on a hoop stress threshold approach. Moreover, the optimal range generated in the analytical method were numerically validated, on Abaqus/CAE software, using Hashin failure criteria and therefore have a degree of reassurance on the result.

The generated results on shell thickness, identified the asymmetrical pattern as the desired sequence of lamination. This analytical result validated through numerical approach, yielded a comparable margin of error of 3 %. Based on the set maximum threshold of 119.4 MPa, it was therefore concluded that improvement in strength over the composite structure was recoded for shell thickness on the 3rd model with 125.52 MPa for profiles 1 and 2.

1. Introduction

Pressure vessel being manufactured as container used for holding liquid or gas at an high storing pressure, it is important to emphasize on its structural strength, in prevention of premature failure occurring on a vessel. Therefore, the factors playing major role on its strength characteristic reside in the structural integrity.

Considering the application, many pressure vessels are manufactured with steel and rolled into a cylindrical or spherical storage container (Choi, 2016). Therefore, in prevention of any adversities the steel material endured (excessive pressure leading to bursting), vessels could be made of composites by combination of different constituents. The composite overwrapped pressure vessels will be therefore made of an shell outer layer carry the pressure load and an inner liner layer to contain the liquid from leaking (Nohan & Yapragada, 2000).

Depending on their advantages, numerous fibres are considered as material for shell constituent of the composite. The most used fibre material used in composites is carbon fibre due to its capability to withstand the load acting on it (Hendlmeier, et al., 2019). In addition, the carbon fibre is commonly used as a material for the composite's shell due to its high modulus and high strength properties. moreover, it has a low coefficient of thermal expansion and high fatigue strength. Due to these advantages brought by the carbon fibre, it has been deemed suitable material to have a reliable structural vessel integrity (Alexander, et al., 2013).

Therefore, the generation of an optimal overwrapping composite vessel with shell material made of carbon fibre was designed to have efficient and reliable container resistance to burst strength.

2. Methodology

This study therefore focused on the determination of allowable shell thickness required in the generation of an optimal composite pressure vessel sustainable to bursting failure. A total of 56 geometrical parts were generated for two common industrial profiles designed in the form of a composite pressure vessel. With regard to strength optimization, these generated part profiles were used to determine the required shell thickness laminated in a symmetrical and asymmetrical pattern. The analytical method was carried out using Tsai-Wu failure theory with generated equations solved using MATLAB software version 2016 in order to determine the mean thickness of composite pressure vessel. Afterwards, the analytical method was validated numerically by Finite Element Analysis using Abaqus software version 2016.

This design, therefore, covers the approach adopted in the reinforcement of the cylinder with the capability to resist failure due to bursting. Conversely, the reinforcement could be achieved by increasing the wall thickness to resist the load applied to the body structure. Hence this approach, optimal pressure vessel should lower weight and improve strength comparatively to the stainless steel vessel.

2.1 Determination of suitable range of liner thickness of composite pressure vessel through conversion of the geometric sizes of the selected stainless steel pressure vessels to equivalent composite pressure vessels

With the exception of wall thickness which was to be determined, predefined dimension (D_i , D_o & L) of two industrial vessel profiles were used as designed in the process of determining the impact of shell thickness over composite pressure vessel. The respective magnitudes were taken as shown in Table 1 (Daniel & Ishai, 2006).

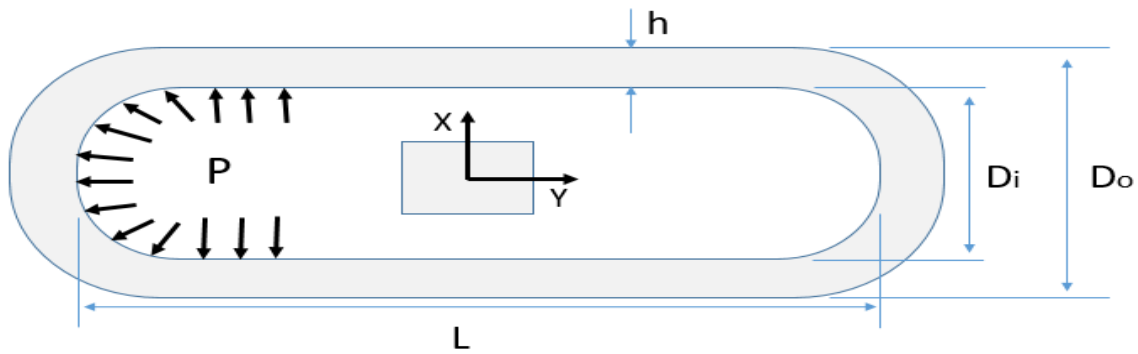


Figure 1: Stainless steel pressure vessel profile

Where:

h = Thickness of stainless-steel pressure vessel

D_i = Inner diameter of stainless-steel pressure vessel

D_o = Outer diameter of stainless-steel pressure vessel

L = Length of stainless-steel pressure vessel

P = Internal pressure

Table 1: Stainless steel pressure vessel profiles (Daniel & Ishai, 2006)

Cross-section description	Profile 1	Profile 2
Vessel length	0.203 m	0.406 m
Inner diameter D_i	200 mm	400 mm
Thickness h	6.7 mm	13.4 mm
Internal pressure	8 MPa	8 MPa

The allowable wall thickness h required to withstand the applied pressure on the two chosen industrial stainless steel profile, were determined with the Von Misses failure theorem of Equation 1 which through derivation lead to the allowable thickness Equation 2 used (Kamal, et al., 2016).

$$\sigma_{max}^2 + \sigma_{min}^2 - \sigma_{max}\sigma_{min} = \left(\frac{S_{yt}}{S}\right)^2 \quad (1)$$

Where:

σ_{max} = Maximum principal stress

σ_{min} = Minimum principal stress

S_{yt} = Tensile yield strength of stainless steel

$$h = \frac{\sqrt{3}PD_iS}{4S_{yt}} \quad (2)$$

Where:

h = Stainless steel allowable wall thickness

P = Internal pressure

D_i = inner diameter of stainless steel pressure vessel

S = Safety factor ($S = 2$)

S_{yt} = Tensile yield strength (207 MPa)

For more clarity in the determination of the vessel wall thickness from Equation 1 to 2, a step-by-step approach from the application of load to the development of the required formula is exhibited in Appendix A.

Table 2: Properties of stainless steel (Daniel & Ishai, 2006)

Properties	Value
Young's modulus, E	193 GPa
Density, ρ	7750 kg/m ³
Poisson's ratio, ν	0.27
Tensile yield strength, S_{yt}	207 MPa
Tensile ultimate strength, S_{ut}	586 MPa

In the conversion of the selected stainless steel pressure vessels to equivalent composite pressure vessels, Equation 2 and Table 2 were used to determine the allowable thickness for the two profiles, being 0.0067 m and 0.0134 m being the reference. Hence, with the liner taken as a variable factor of the study, the determined thicknesses were halved to have a structural vessel composed of liner and shell as displayed in Figure 2.

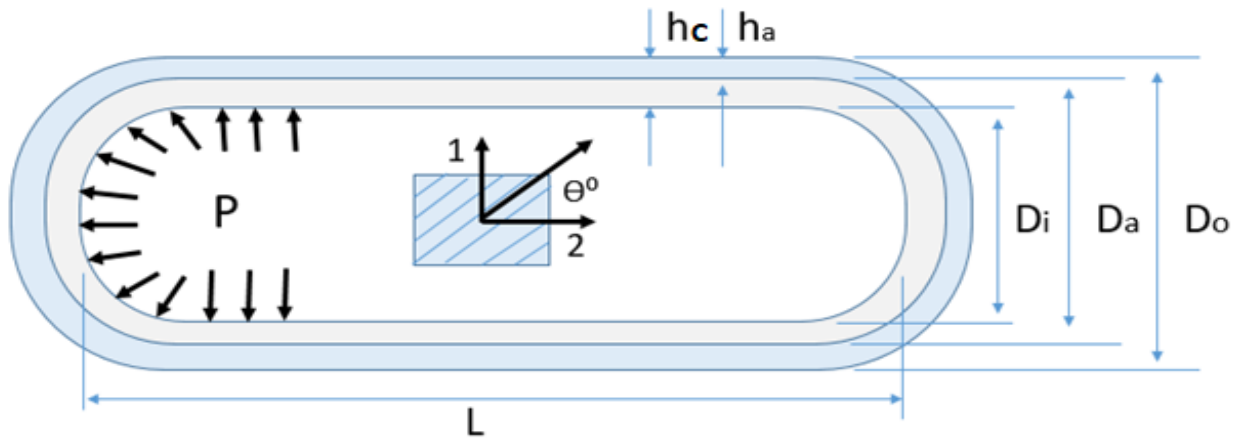


Figure 2: Composite pressure vessel profile

Where:

h_c = Thickness of composite pressure vessel

h_a = Carbon fibre shell thickness

D_i = Inner diameter of composite pressure vessel

D_a = Inner diameter of carbon fibre shell

D_o = Outer diameter of carbon fibre shell

Θ^0 = fibre angle orientation

P = internal pressure

The size variation of the liner ranged from 0.00335 m to 0.00670 m for profile 1 and 0.0067 m to 0.0134 m for profile 2, with a respective increment of 0.000558 m and 0.001117 m determined with equation 4 (Sonnen., 2004).

$$i = \frac{h_{max} - h_{min}}{n - 1} \quad (4)$$

Where

i = Increment

h_{max} = Maximum liner thickness

h_{min} = Minimum liner thickness

n = Number of parts

A 28 geometrical part profiles were therefore generated for the determination of an optimal shell thickness analyzed on a on symmetrical and asymmetrical patterns for both profiles as illustrated in table 3.

Table 3: Liner geometrical thickness for shell portion of composite pressure vessel's shell

Part Number	Orientation angle (°)	Profile 1 (mm)		Profile 2 (mm)	
		Symmetrical	Asymmetrical	Symmetrical	Asymmetrical
1	55	3.350	3.350	6.700	6.700
2	55	3.908	3.908	7.817	7.817
3	55	4.467	4.467	8.933	8.933
4	55	5.025	5.025	10.050	10.050
5	55	5.583	5.583	11.167	11.167
6	55	6.142	6.142	12.283	12.283
7	55	6.700	6.700	13.400	13.400

2.2 Determination of shell thickness of composite pressure vessels

The following steps were used in determination of shell thickness required as lamination layer for a reliable composite pressure vessel with strength properties resistant to bursting failure.

2.5.1 Analytical method

The idea of incorporating shell over a metallic liner was done to reduce the risk of bursting failure by rendering the vessel strong enough to offer resistance, with the weight factor considered. Therefore, the structural integrity was determined using the Von-Mises failure theorem for a common industrial stainless steel vessel exposed to a pressure of 8 MPa. The two considered profiles found structural resistance at wall thicknesses of 0.0134 m and 0.0067 m, respectively. Half of the determining wall thickness was regarded as a liner for the exhibition of the advantages resulting from weight saving and strength by shelling the liner with the fibre. This was done with an emphasis on the fact that this portion, when not shell reinforced against bursting, would ultimately fail under the chosen pressure (Assam, et al., 2006). The remaining half portion of the allowable stainless steel thickness was replaced by a fibre shell as reinforcement and used for failure analysis for determination of thickness resistance against bursting failure, as shown in Figure 3 (Farhood, 2017).

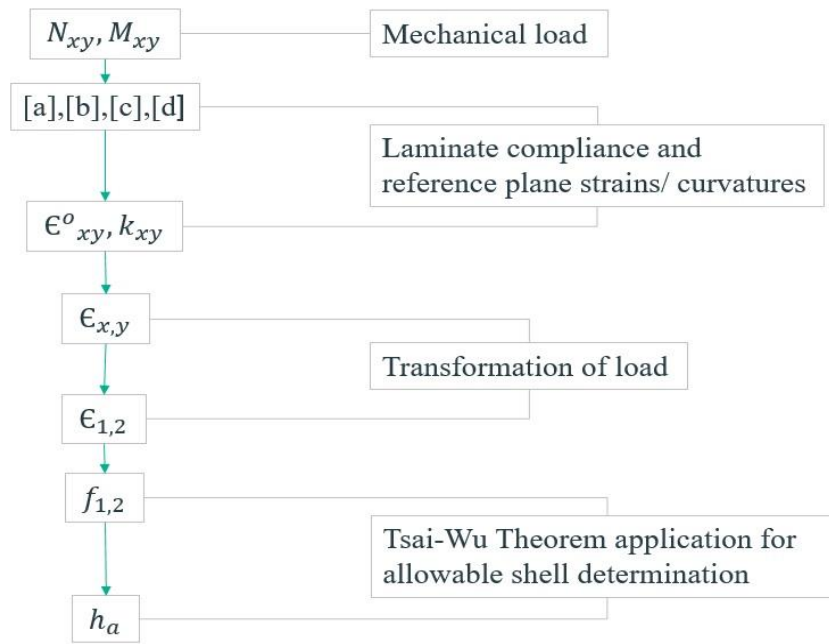


Figure 3: Steps of allowable shell thickness determination (Farhood, 2017).

2.5.1.1 Mechanical loading

Through the process of shell thickness determination, The Tsai Wu theorem was used to derive Equation 17 adopted for the generation of allowable shell thickness overwrapping the liner. The stresses (σ_1 & σ_2) used in this equation were based on the principal axes and generated from a pressure of 8 MPa applied on the internal surface of the vessel. This has been performed to have the effect of the load referred to on the shell operating in the principal axes and for which thickness was determined. (shell material being of a orthotropic nature expressed on the principal axes)

Due to the nature of the composite pressure vessel of isotropic and orthotropic properties applied on the liner and shell, respectively, the applied load propagation was not considered whole for the entire composite. As shown in Figure 4 the stress propagation on a laminated composite of an orthotropic nature was not linear, unlike the strain. Therefore to express the pressure effect on the shell, the stresses ($\sigma_{x,y}$) were to be expressed in terms of strains $\epsilon_{x,y}$ in global axes, which were then converted to the principle axes ($\epsilon_{1,2}$) and ultimately determine the stresses on the shell ($\sigma_{1,2}$).

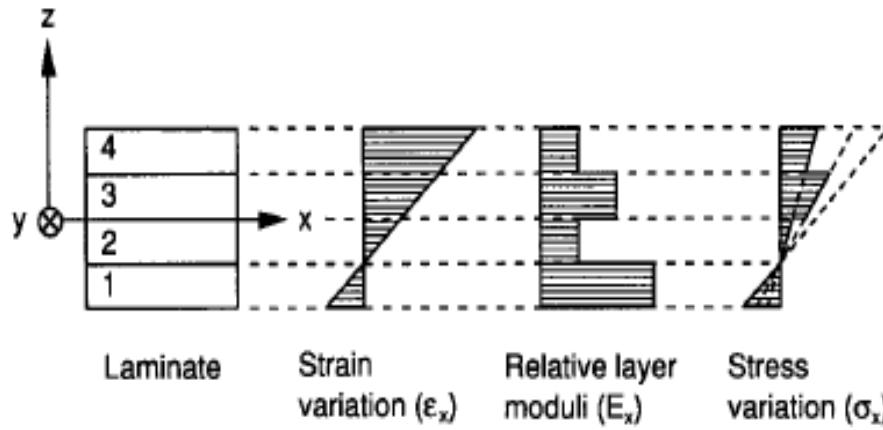


Figure 4: Stress and strain variation on the multidirectional laminate (Frias , et al., 2010)

The force matrix N_{xy} and moment matrix M_{xy} referred on the shell, were determined using Equation 5 (Farhood, 2017). These loads were taken per unit length as the value of ‘h’ represented in the shell thickness to be determined (Pa.m =N/m)

$$N_{xy} = \begin{pmatrix} N_x \\ N_y \\ N_s \end{pmatrix} \quad (5)$$

$$M_{xy} = \begin{pmatrix} M_x \\ M_y \\ M_s \end{pmatrix}$$

Where

$$N_x = \sigma_x h = \frac{pD_i}{4} \quad : \text{Longitudinal force per unit length}$$

$$N_y = \sigma_y h = \frac{pD_i}{2} \quad : \text{Hoop force per unit length} \quad (6)$$

$N_s = M_x = M_y = M_s = 0$: The shear force and moments per unit length are taken as zero (Internal pressure producing shear or bending in the vessel structure)

2.5.1.2 Laminate compliance and reference plain strains/curvatures

Upon determination of applied stresses, the propagation effect (Refer to figure 4) of the mechanical load on the composite was generated through deformation, which for this objective, focused on the shell portion for which thickness was to be determined.

Therefore, the strain deformation effect on the shell portion was determined by first generating the laminate extension compliance matrices with Equation 7. This approach was made due to the fact that stress was not transmission through a composite linearly. Due to the difference in material composition and directional factors, its effect varied from constituent to constituent and from layer to layer.

$$\begin{aligned}
 a &= A^{-1} - \{(-A^{-1}B)d\}(BA^{-1}) \\
 b &= (-A^{-1}B)d \\
 c &= -d(BA^{-1}) \\
 d &= (D - \{BA^{-1}\}B)^{-1}
 \end{aligned}
 \tag{7}$$

Where:

a, b, c, d = laminate compliance stiffness matrices

A= extension compliance matrix

B = coupling stiffness matrix

D = bending stiffness matrix

These laminate extension compliance matrices were used to relate stresses to the deformation of shell portions, with “A” factor relating the load and the strain. The coupling stiffness, B, related the in-plane load to the curvature, whereas the bending stiffness, D, related the moment to the curvature. These matrices were determined using Equation 8, where the expression Q_{xy}^k being the lamination repartition was accounted for on the shell portion per laminate by $h_k - h_{k-1}$ for profiles 1 and 2, from 0.00334 m and 0.0067 m, respectively (refer to Figure 5). These laminate stiffness matrix which for this study were determined for four laminates on both profiles with Equation 9. Therefore, with the consideration of lamination of 4 layers, the sequential pattern was analyzed in symmetrical and asymmetrical pattern with the optimal angle of 55° in expression 9.

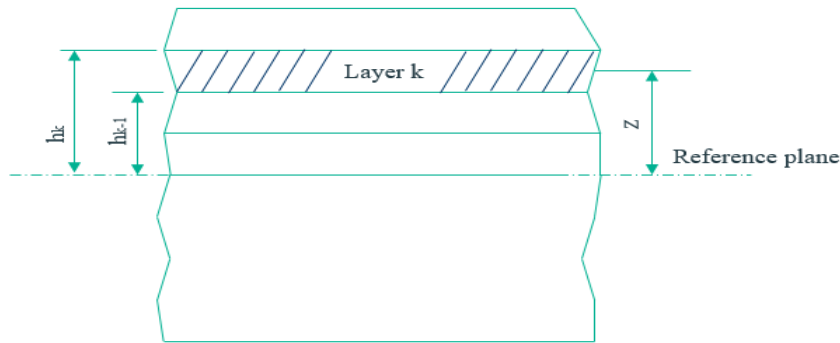
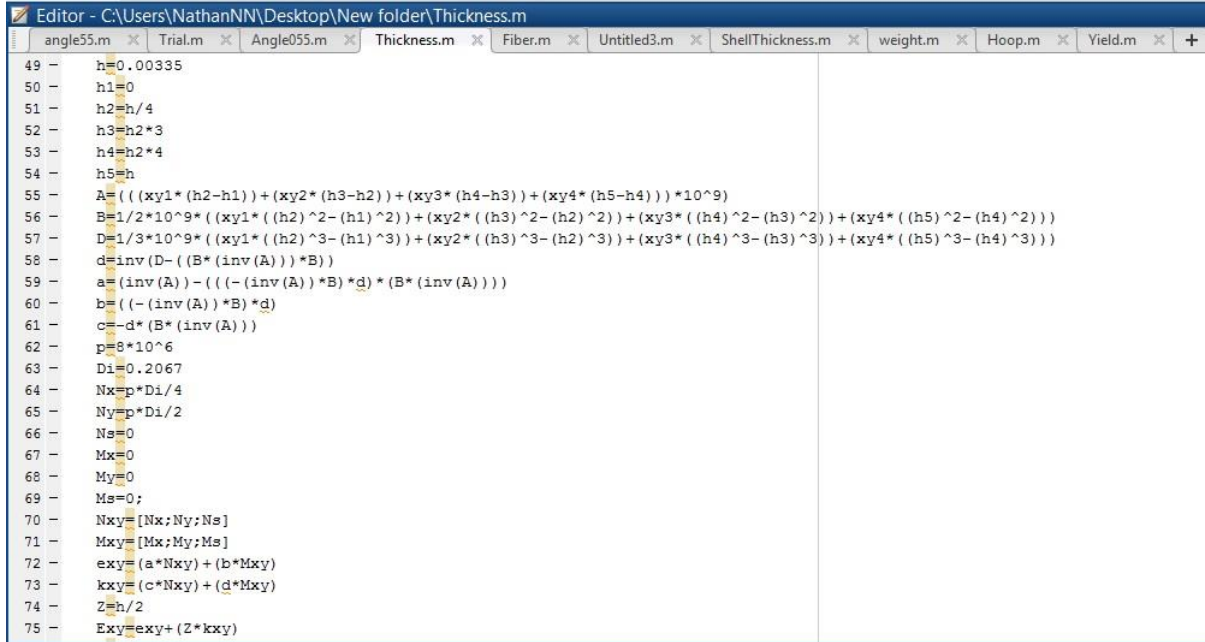


Figure 5: Layer referential (Kamal, et al., 2016)

$$\begin{aligned}
 A &= \sum_{k=1}^i Q_{xy}^k (h_k - h_{k-1}) \\
 B &= \frac{1}{2} \sum_{k=1}^i Q_{xy}^k (h_k^2 - h_{k-1}^2) \\
 D &= \frac{1}{3} \sum_{k=1}^i Q_{xy}^k (h_k^3 - h_{k-1}^3)
 \end{aligned}
 \tag{8}$$

$$[Q]_{xy} = \begin{bmatrix} Q_{xx} & Q_{xy} & Q_{xs} \\ Q_{xy} & Q_{yy} & Q_{ys} \\ Q_{xs} & Q_{ys} & Q_{ss} \end{bmatrix} \quad (9)$$

The equation 9 were solved using Matlab software 2016 version as shown from the codification analysis in Figure 6, and ultimately determine the laminate extension compliance matrices.



```

49 - h=0.00335
50 - h1=0
51 - h2=h/4
52 - h3=h2*3
53 - h4=h2*4
54 - h5=h
55 - A=((xy1*(h2-h1))+(xy2*(h3-h2))+(xy3*(h4-h3))+(xy4*(h5-h4)))*10^9)
56 - B=1/2*10^9*((xy1*((h2)^2-(h1)^2))+(xy2*((h3)^2-(h2)^2))+(xy3*((h4)^2-(h3)^2))+(xy4*((h5)^2-(h4)^2)))
57 - D=1/3*10^9*((xy1*((h2)^3-(h1)^3))+(xy2*((h3)^3-(h2)^3))+(xy3*((h4)^3-(h3)^3))+(xy4*((h5)^3-(h4)^3)))
58 - d=inv(D)-(B*(inv(A))*B)
59 - a=(inv(A))-((-inv(A))*B)*d*(B*(inv(A)))
60 - b=(-(inv(A))*B)*d
61 - c=-d*(B*(inv(A)))
62 - p=8*10^6
63 - Di=0.2067
64 - Nx=p*Di/4
65 - Ny=p*Di/2
66 - Ns=0
67 - Mx=0
68 - My=0
69 - Ms=0;
70 - Nxy=[Nx;Ny;Ns]
71 - Mxy=[Mx;My;Ms]
72 - exy=(a*Nxy)+(b*Mxy)
73 - kxy=(c*Nxy)+(d*Mxy)
74 - Z=h/2
75 - Exy=exy+(Z*kxy)
    
```

Figure 6: Codification analysis of compliance matrices on Matlab software

From Equations 10 and 11, the structural strains of lamination ϵ_{xy} were determined and recorded in elongation (ϵ_{xy}^0) and bending (k_{xy}) generated from the combination of laminate extension and the load relation.

$$\epsilon_{xy}^0 = \begin{Bmatrix} \epsilon_x^0 \\ \epsilon_y^0 \\ \gamma_s^0 \end{Bmatrix} = aN_{xy} + bM_{xy} \quad (10)$$

$$k_{xy} = \begin{Bmatrix} k_x \\ k_y \\ k_s \end{Bmatrix} = cN_{xy} + dM_{xy} \quad (11)$$

$$\begin{Bmatrix} \epsilon_x \\ \epsilon_y \\ \gamma_s \end{Bmatrix} = \begin{Bmatrix} \epsilon_x^0 \\ \epsilon_y^0 \\ \gamma_s^0 \end{Bmatrix} + z \begin{Bmatrix} k_x \\ k_y \\ k_s \end{Bmatrix} \quad (12)$$

Where z is the location or coordinate of the mid-surface of the laminate to the reference plane as seen from Figure 5.

A complete step by step approach of the Matlab codification analysis is included in Appendix B for an insight to this analytical approach.

2.5.1.3 Load transformation

With the strain ϵ_{xy} representing the shell deformation on the global axes, the stress exhibited through fibre laminate was determined in the principal axes due to the orthotropic nature of shell. This strain was first converted from the global to principal axes with the transformation expression of Equation 13, with θ at optimal angle of 55° . The strain application of fibre in the principal axes was therefore given by Equation 14 whereby, the transformation term, T were used in the process of conversion from global to principal axes.

$$T = \begin{bmatrix} C^2 & S^2 & 2CS \\ S^2 & C^2 & -2CS \\ -CS & CS & C^2 - S^2 \end{bmatrix}, C = \cos\theta, S = \sin\theta \quad (13)$$

$$\begin{Bmatrix} \epsilon_1 \\ \epsilon_2 \\ \gamma_6 \end{Bmatrix} = T \begin{Bmatrix} \epsilon_x \\ \epsilon_y \\ \gamma_{xy} \end{Bmatrix} \quad (14)$$

The strain ($\epsilon_{1,2}$) of the composite material in the principal axes were ultimately expressed in form of stresses ($\sigma_{1,2}$) by mean of Equation 15, linking them in the principal axis with Young's modulus and Poisson's ratio of carbon fibre featured in Table 2.

$$\begin{Bmatrix} \sigma_1 \\ \sigma_2 \\ \tau_6 \end{Bmatrix} = \begin{bmatrix} Q_{11} & Q_{12} & 0 \\ Q_{12} & Q_{22} & 0 \\ 0 & 0 & Q_{66} \end{bmatrix} \begin{Bmatrix} \epsilon_1 \\ \epsilon_2 \\ \gamma_6 \end{Bmatrix} \quad (15)$$

Where the stiffness values were calculated by:

$$Q_{11} = \frac{E_1}{1 - \nu_{12}\nu_{21}}, \quad Q_{12} = \frac{\nu_{21}E_1}{1 - \nu_{12}\nu_{21}},$$

$$Q_{22} = \frac{E_2}{1 - \nu_{12}\nu_{21}}, \quad Q_{66} = G_{12} \quad (16)$$

E_1 = Longitudinal modulus

E_2 = Transverse modulus

ν_{12} = In-plane Poisson's ratio

ν_{21} = Out-of-plane Poisson's ratio

G_{12} = In-plane shear modulus

2.5.1.4 Tsai-Wu failure criteria application for allowable shell thickness determination

The allowable shell thickness resistance to bursting failure in the models of profiles 1 and 2 were determined using Equation 17 following analytical procedure using Matlab software as derived in Appendix A, section 4. Equation 18 was derived from Tsai-Wu failure criteria. Upon derivation of this failure criteria, the allowable laminate safety factor was generated as shown in Equation 18 (Mian, et al., 2013). The basic laminate thickness h_0 and the first ply failure theorem were also used to develop Equation 17 with a respective magnitude of 0.02 mm and 2 (Mian, et al., 2013).

$$h_a = \frac{S_{fall}}{S_{fk}} h_0 \quad (17)$$

$$S_{fk} = \frac{-\beta + \sqrt{\beta^2 + 4\alpha}}{2\alpha} \quad (18)$$

Where α and β were calculated by (refer to table 4 for property description):

$$\alpha = f_{11} \sigma_1^2 + f_{22} \sigma_2^2 + f_{66} \tau_6^2 + 2f_{12} \sigma_1 \sigma_2 \quad \beta = f_1 \sigma_1 + f_2 \sigma_2 \quad (19)$$

Where:

$$f_1 = \frac{1}{F_{1t}} - \frac{1}{F_{1c}}, \quad f_2 = \frac{1}{F_{2t}} - \frac{1}{F_{2c}}, \quad f_{11} = \frac{1}{F_{1t}F_{1c}}, \quad f_{22} = \frac{1}{F_{2t}F_{2c}}, \quad (20)$$

$$f_{66} = \frac{1}{F_6^2}, \quad f_{12} = -\frac{1}{2} \sqrt{f_{11}f_{22}}$$

Table 4: Property of carbon fibre (Daniel & Ishai, 2006)

Properties	Value
Density, ρ	1540 kg/m ³
Longitudinal modulus, E_1	147 GPa
Transverse modulus, E_2	10.3 GPa
In-plane shear modulus, G_{12}	7 GPa
Out-of-plane shear modulus, G_{13}	7 GPa
In-plane Poisson's ratio, ν_{12}	0.27
Out-of-plane Poisson's ratio, ν_{23}	0.54
Out-of-plane Poisson's ratio, ν_{13}	0.27
Fibre volume fraction, ν_f	0.0063
Longitudinal tensile strength, F_{1t}	2280 MPa
Transverse tensile strength, F_{2t}	57 MPa
Transverse shear strength, F_5	65 MPa
In-plane shear strength, F_6	71 MPa
Longitudinal compressive strength, F_{1c}	1725 MPa

Transverse compressive strength, F_{2c}	2280 MPa
---	----------

2.5.1.5 Determination of sustainable range of shell thickness

The identification of the best range of shell thickness sustainable enough to resist failure was done with an emphasis on the vessel strength criteria (Stress used as threshold limitation). Therefore, hoop stress being the criteria representing the respective resistance to bursting effect, Equation 21 was used to represent the sustainability of the different composite models. This approach was done to determine the range of optimal composite hoop stresses and compared them to the hoop stress of the stainless steel vessel considered as threshold at 119.4 MPa for profile 1 and 2.

$$\sigma_h = \frac{Et + \frac{v}{2}E_f t_f}{Et + E_f t_f} \frac{pR}{t} \quad (21)$$

The hoop stress of a composite pressure vessel expressed in Equation 21 (Adali & Verijenko, 1995) was used for a composite pressure vessel having an internal pressure of 8 MPa as derived in Appendix A. This stress propagated to a liner layer of thickness t and shell layer of thickness t_f with respective material properties of liner Young's modulus E and Poissons' ratio v , whereas, the carbon fibre Young's modulus was denoted as E_f .

2.5.2 Numerical method

In the validation of shell thickness generated through analytical method, a numerical approach was used to generate the dimension profiles through simulation of the 28 models. The simulation was done using finite element analysis in the Abaqus software.

Since the strength of the composite pressure vessel was the purpose of the study, the verification was based on the capacity of the structure to withstand the required mechanical load. Hence, the use of numerical method allowed the comparison of strength on all generated models of the analytical approach and ultimately determine the error margins. The following eight modelling steps of Abaqus software were followed:

2.5.2.1 Part creation

The required part models for this specific task were created within Abaqus. The creation of the part model was done through the selection of the dialogue box "create part" which allowed the renaming of the part. The modelling space option was kept at 3D with deformable type as the base feature of the shell with extrusion type for the creation of the cylinder vessel. The approximate size was set once more to 600 mm to accommodate the first profile of length 203 mm and diameter 200 mm and second profile of length 406 mm and diameter 400 mm.

2.5.2.2 Property module

The material property assignment was done in Abaqus by selecting property on the module toolbar and clicking on the “create material” option. This time around, the composite property was created for assignment to the four laminates considered in the study and hence, under mechanical elasticity the behavior of “elastic material” was selected. The type of elasticity was once more set to Engineering Constraints with shell fibre properties imparted.

For this task, the liner material was still created with mechanical elasticity set to isotropic with Young’s modulus of 193 GPa and a Poisson’s ratio of 0.27.

In order to create the composite, on the side bar, the “create composite layup” was used. This composite was created with an initial ply set at five layers, to account for the liner and the three laminates ply with element type set as conventional shell. The orientation of the layup was set to discrete (normal and primary axis) with its definition done by editing the surface after clicking on the surface of the composite. The primary axis direction definition was done by clicking on the closest edge of the composite.

The layup was followed by the region selection picked on the surface of the composite. The material created were then assigned to the liner and the laminate layers, with their respective thickness. For instance, in the case of the first model of profile 2 and an asymmetrical pattern of orientation, the liner thickness was set to 6.7 mm and 0.375 mm thickness on each laminate to account for the total shell thickness of 1.5 mm. The direction of constituents was finally imparted in the rotation angle column with 0° for liner and 55° on an asymmetrical pattern for the four laminate.

2.5.2.3 Assembly module

The creation of an instance in the assembly part module was kept at “dependent” (default settings for application of the original part mesh to the entire dependent instances of the part). The entire model was designed as a single composite though made of different constituents, namely: the liner and laminate. Therefore, the whole vessel was, considered as a part in the same coordinate (allowing the meshing of the part only once).

2.5.2.4 Step module

The creation of step also considered the presence of internal pressure, cylinder endcap and boundary conditions, which led to the creation of additional steps that were kept at static general. These steps were to be assigned to the load process and the boundary conditions.

In addition to that, the surfaces on which loading were to be applied were also created through this module under the surface manager of the tool option. Furthermore, the field output request was selected, and the domain set for “composite layup”. Therefore, the output variable was set for stress, invariants and total strain components which were used for analysis at the end of the model.

2.5.2.5 Load module

The mechanical loading on the internal surface of the cylinder was created by selecting “pressure” on the load module and inputting a value of 8 MPa. In addition to that, the presence of an endcap having longitudinal stress of -164.949 MPa, was applied on the both edges of the vessel to simulate the effect of the closed ends.

2.5.2.6 Boundary condition

The displacement/rotation boundary condition was created. This boundary condition was restricted in UR1, UR2 and UR3 for the rotational direction constraint. The longitudinal effect created by the endcap and hoop factor in the displacement along the X, Y and Z axis was kept unrestricted at U1, U2 and U3.

2.5.2.7 Mesh Module

The models of the validating process of thickness determination were meshed at global size kept at 57 default settings to account for the running time as the models designed are of a composite nature.

Meshing was therefore performed with element type selected as shell family and geometrical order under linear full integrated with all element created as per the seeding of the model. A total number of 154 elements were created.

2.5.2.8 Visualization

Figure 7 impart properties and mechanical load effect set upon the composite pressure vessel design of this numerical approach. The result was visualized at 75% average as the default setting with the hoop stress field output request exhibited and compared to the analytical findings.

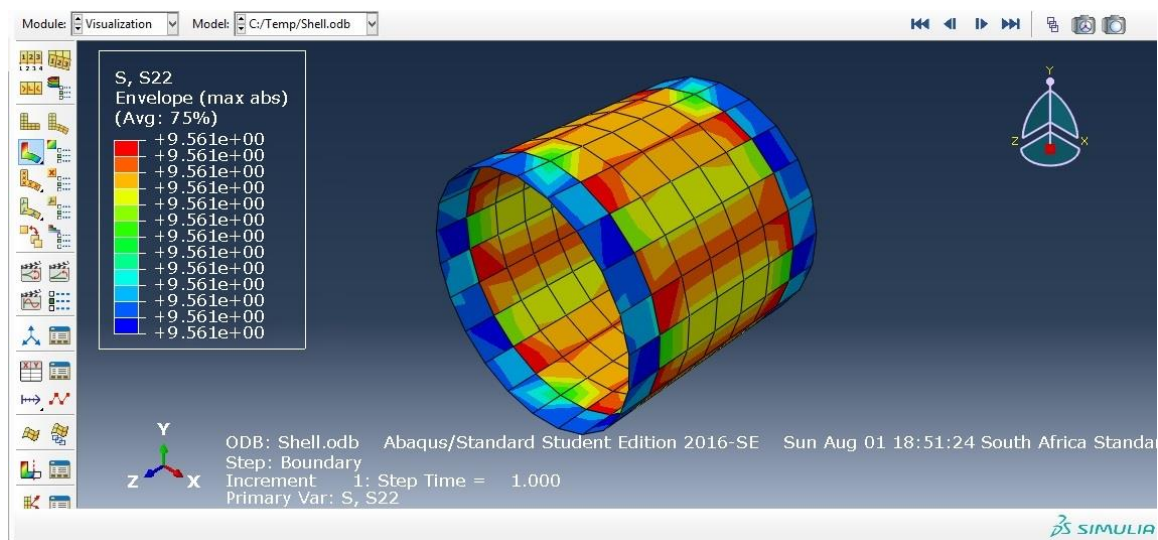


Figure 7: Visualization of hoop stress

3. Results and discussion

This chapter presents the results and discussions on the design of an optimal composite pressure vessel composed of stainless-steel liner and carbon fibre shell as influential factors to the integrity of the structure. The effect of these influential factors and results generated from the previous section, were represented in graphs and tables to emphasize on the sustainability of the composite structural integrity with the aim of resisting bursting failure. These analytical results were discussed and eventually verified through numerical approach of finite element analysis. The ultimate result of fibre and shell thickness that yielded a combined optimal design for which strength improvement was obtained.

3.1 Analyses of shell thickness results

The results obtained from the analytical approach adopted in the fibre and shell thickness determination, were represented in Tables 5 and 6. These results ultimately exhibited the effects of shell incorporation over the metallic liner in the developing a sustainable composite pressure vessel resistant to failure with improved strength compared to a full metallic vessel.

On the other hand, a graphical representation of the fibre and shell thickness based on the hoop strength and the Tsai-Wu theorem was used to determine the maximum, minimum and or peak allowable value required in the analysis of the range used for the combination and generation of a reliable optimal composite pressure vessel.

3.1.2 Allowable shell thickness results

The analytical results on shell thickness of profiles 1 and 2 are shown in Tables 5 and 6. These shell thicknesses have been generated in symmetrical $[+\Theta / - \Theta / - \Theta / + \Theta]$ and asymmetrical $[+\Theta / - \Theta / + \Theta / - \Theta]$ patterns of lamination. In addition, the distinction on the lay-up pattern from lamina to laminate constituting the liner's shell has been made based upon optimal directional of 55° .

The effect of hoop and longitudinal stress created by the internal pressure was considered in the analysis as per Equation 6.

Table 5: Shell thickness of profile 1

Part Number	Orientation (Degree)	Profile 1			
		Symmetrical		Asymmetrical	
		Stainless steel liner	Shell (mm)	Stainless steel liner	Shell (mm)
1	55	3.35	10	3.35	9.3
2	55	3.908	5	3.908	4.6
3	55	4.467	3.3	4.467	3.1
4	55	5.025	2.5	5.025	2.3
5	55	5.583	2	5.583	1.8
6	55	6.142	1.6	6.142	1.5
7	55	6.7	0.7	6.7	0.6

Table 6: Shell thickness of profile 2

Part Number	Orientation (Degree)	Profile 2			
		Symmetrical		Asymmetrical	
		Stainless steel liner (mm)	Shell (mm)	Stainless steel liner (mm)	Shell (mm)
1	55	6.7	20.1	6.7	18.6
2	55	7.817	10	7.817	9.3
3	55	8.933	6.6	8.933	6.1
4	55	10.05	4.9	10.05	4.6
5	55	11.167	3.9	11.167	3.6
6	55	12.283	3.3	12.283	3
7	55	13.4	1	13.4	0.9

3.2 Identification of sustainable shell thickness range

With the two profiles' generated shell thickness, a range of maximum and minimum level was needed to be determined and imparted into the optimization process to yield the optimal composite pressure vessel through factor combinations (liner and shell thickness). Therefore, the optimal shell thicknesses were determined with the aim of strength optimization. The maximum and minimum value of shell thickness given by hoop stress above the threshold determined from the hoop stress of stain less steel vessel, for which improvement needed to be achieved.

3.2.1 Sustainable shell thickness determination

The analysis under shell thickness determination was done using an internal pressure that produced axial and hoop stress, which was used in the determination of the most optimal design of composite made of liner and lamination shell. Therefore, with strength as the driving factors of this study, the hoop stresses (table 7) were taken to have an influential effect on the governing of the bursting failure of the vessel.

Table 7: Hoop stress of profile 1 and 2

	Profile 1		Profile 2	
Parts	Symmetry (MPa)	Asymmetrical (MPa)	Symmetry (MPa)	Asymmetrical (MPa)
1	95.340	98.564	95.121	98.564
2	117.32	121.00	117.31	120.52
3	123.31	125.52	123.32	125.52
4	121.36	123.61	121.91	123.61
5	116.72	118.86	117.24	118.85
6	111.60	112.58	111.12	112.59
7	111.79	112.81	113.85	114.38

From Table 7, it is evident that despite the double factor between profiles, the hoop stress generated for the different models of symmetrical and asymmetrical patterns exhibited similarity in values with a degree of discrepancy of 1 %. The threshold hoop stress generated from the stainless steel vessel of thickness 6.7 mm for the first profile and 13.4 mm for the second profile with the same internal pressure of 8 MPa, was found unchanged for the two profiles with a value of 119.4 MPa (determined with Equation 6).

From Figures 8 and 9, an observation could also be made on the comparison between symmetrical and asymmetrical patterns on the two industrial profiles, based upon the results of hoop stress of the respective

allowable shell thicknesses. It was clearly apparent that the asymmetrical hoop stress generated on both profiles gave better results than the symmetrical hoop stress generated on both profiles with an average of 2% more, making this pattern the most desirable option for a vessel overwrapped with shell layer.

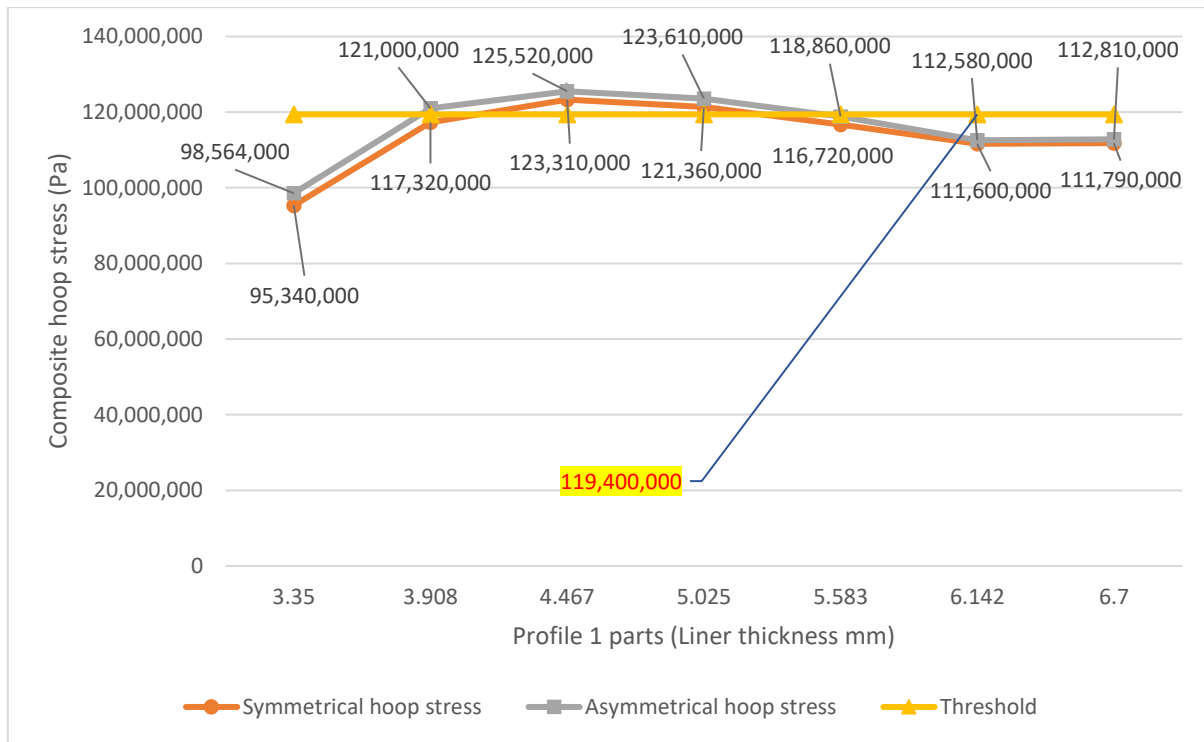


Figure 8: Shell thickness range of profile1

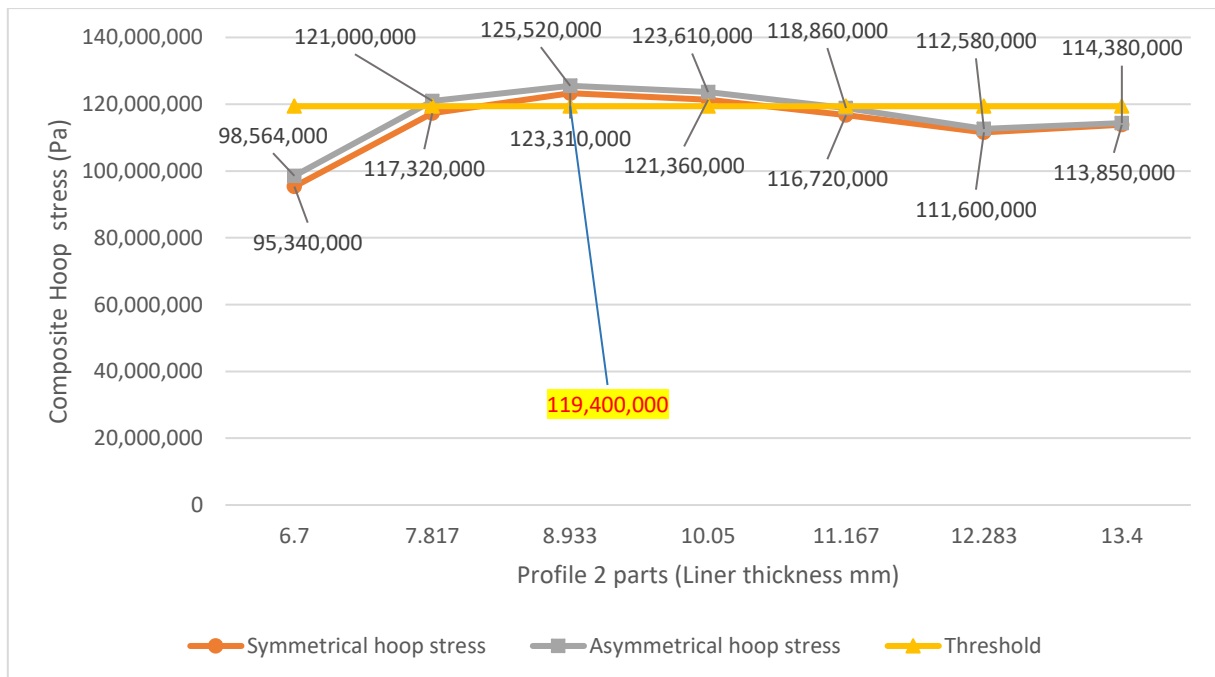


Figure 9: Shell thickness range of profile 2

With the intention of finding the shell thickness that was most optimal for a reliable composite pressure vessel, the same hoop stress exhibited in Figures 7 and 8 were used. These hoop stresses were generated from the respective allowable shell thickness, making the second and third optimal thickness on both profiles, with 3.1 and 2.3 for the first profile and 6.1 and 4.6 m on the second. This was because they represented an improvement from the limit threshold (119.4 MPa) of a whole stainless steel vessel required to handle the same internal pressure as the composite.

3.3 Validation of analytical results with numerical approach

Through design of composite pressure vessel shell thickness were generated through analytical approach which was the reference method. Therefore, to have more credibility on the generated thickness to be used for the optimal design of profiles 1 and 2, validation through numerical approach was done on the result.

3.3.1 Validation of shell thickness results

The analytical results of the generated shell thickness were validated numerically (due to the difference in accuracy) for this task with hoop stress as the influential factor for the composite modes of profiles 1 and 2. The two approaches generated hoop stresses which were compared against each other, as shown in Figures 10 and 11.

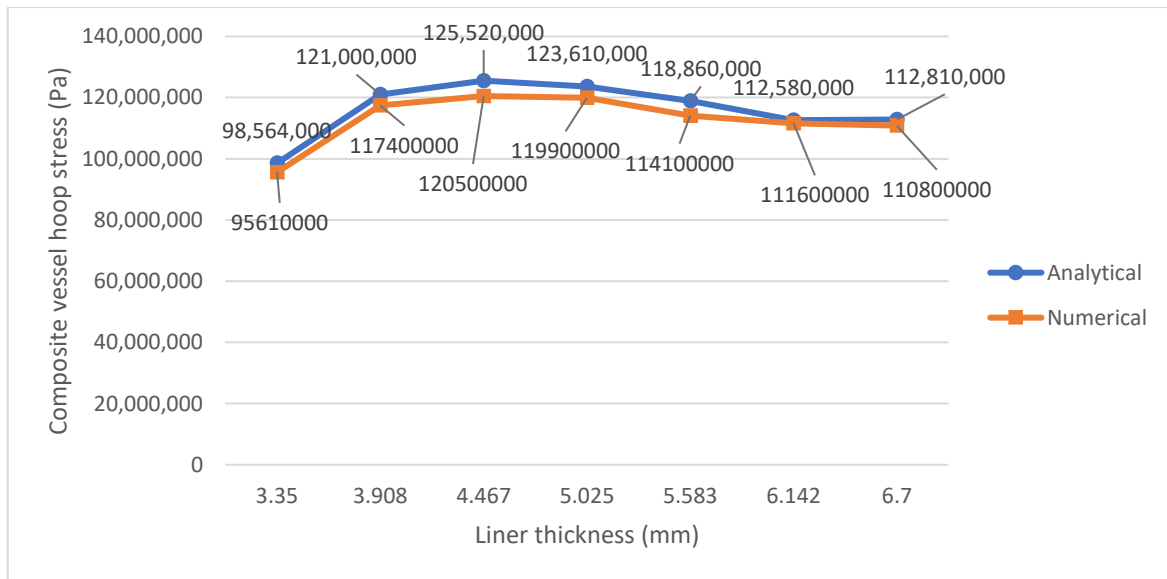


Figure 10: Profile 1 shell approach validation

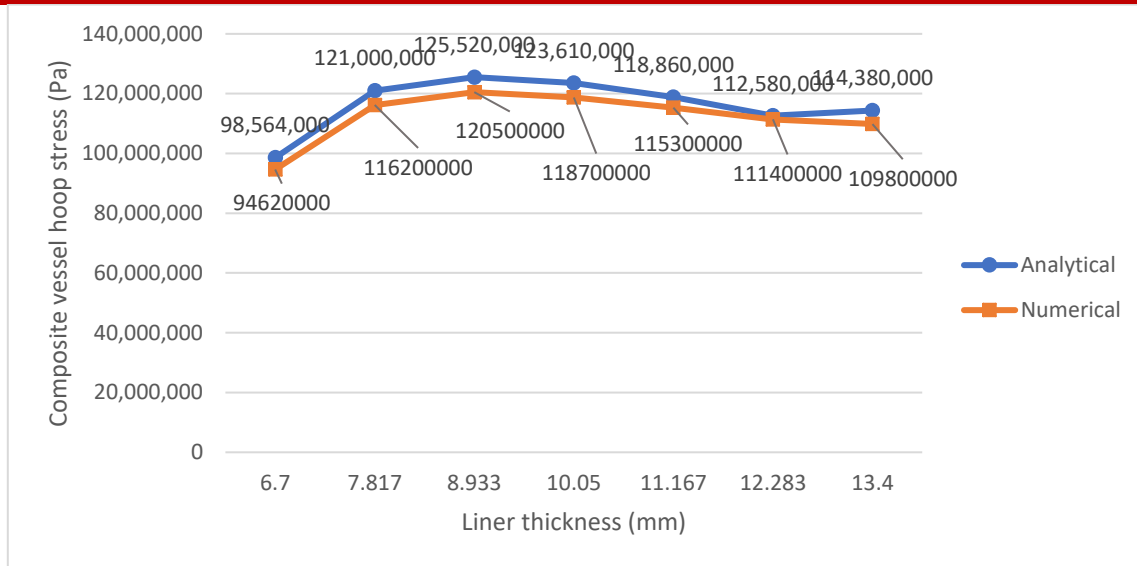


Figure 11: Profile 2 shell approach validation

The graphical comparison exhibited a coherence between the two approaches with a slight deviation of 3% on average, as expressed in Table 8 with the analytical method taken as reference. This percentage was considered acceptable with the analytical hoop stress value increasing to its maximum value at model 3, which then decreased beyond a threshold value of 119.4 MPa taken from hoop stress of stainless vessel of the corresponding size. The representation of the numerical approach has also increased to a maximum value located at the same third model with a slight decrease after that.

Table 8: Error margin over the comparison of analytical to numerical results on shell thickness validation

Profile 1								
Analytical hoop stress (MPa)	98.564	121.000	125.520	123.610	118.860	112.580	112.810	
Numerical hoop stress (MPa)	95.610	117.400	120.500	119.900	114.100	111.600	110.800	
% error margin	2.99%	2.98%	4.00%	3.00%	4.00%	1.00%	1.78%	
Profile 2								
Analytical hoop stress (MPa)	98.564	120.520	125.520	123.610	118.850	112.590	114.380	
Numerical hoop stress (MPa)	94.620	116.200	120.500	118.700	115.300	111.400	109.800	
% error margin	4.00%	3.97%	4.00%	3.97%	3.00%	1.05%	4.00%	

4. Conclusions and recommendations

The conclusions and recommendations were generated based upon this study findings

4.1 Conclusions

1. With symmetrical and asymmetrical patterns considered as orientation of shell lamination, the asymmetrical pattern was considered as the best option of lamination sequence due to the fact that better hoop stress with less material thickness were required from part profile 1 to 7.
2. This analytical findings on shell thickness, validated through numerical approach, were found to have a comparable average margin of error of 3% on both profiles
3. The overwrapped pressure vessel shell models revealed an improvement in strength over the composite structure in comparison to the stainless-steel threshold maximum stress (119.4 MPa). This improvement was recoded on the 3rd models on both profiles with strength of 125.52 MPa.

4.2 Recommendations for future work

1. Based on the literature review, the incorporation of fibre over the pressure vessel to form a composite structure, strong enough to resist bursting, was improved with a laminate pattern in a symmetrical and asymmetrical point of view. Insight on the remaining pattern to yield an optimal vessel still leaves room for further research to see the best lamination option that could be adopted for greater resistance to bursting.

5. Declaration

I Mr. Nathan Numbi Mukala, declare that the work in this article titled “Optimal shell thickness for Overwrapped Composite High-Pressure Vessels ” has been written by me in the department of Mechanical engineering.

References

- Abrate, S., 1998. Impact on composite structures. *Cambridge University Press*, pp. 86-89.
- Adali, S. & Verijenko, V., 1995. Optimization of multilayered composite pressure vessels using exact elasticity solution. *Composite Pressure Vessels* , pp. 203-312.
- Alexander, C. S., Key, C. T. & Schumacher, S. C., 2013. Dynamic Response and Modeling of Carbon Fiber-epoxy Composite Subject to Shock Loading. *Journal of Applied Physics*, pp. 22-114.
- Alexis, A. K., 1999. Composite Pressure Vessel with High Stiffness. *Elsevier science Ltd Composite structure*, Volume 48, pp. 119-127.
- Assam, B.S., Muhammad, M.A. & Mokhtar, M.O.A., 2006. A theoretical and design analysis of the filament-wound. *Composite Pressure Vessels*, Volume 40, pp. 73-86.

- Choi, H. I., 2016. Low-velocity impact response analysis of composite pressure vessel considering stiffness change due to cylinder stress. *Composite Structures*, Volume 160, pp. 491-502.
- Daniel, I. M. & Ishai, O., 2006. Engineering mechanics of composite materials. *Second Edition Oxford University Press*, pp. 34-67.
- Farhood NH, K. S., 2017. Burst pressure investigation of filament wound type IV composite pressure vessel. *American Institute of Physics Conference Proceedings*, pp. 56-68.
- Frias , C. et al., 2010. Manufacturing and testing composite overwrapped pressure vessels with embedded sensors. *Mater des*, pp. 406-421.
- Gentileau, B., Villalonga, F., Nony, H. & Galiano, H., 2015. A probabilistic damage behavior law for comosite material dedicated to composite pressure vessel. *International Journal Hydrogen Energy*, Volume 13193-13205, p. 40.
- Gentilleau, B., Magneville, B. & Villalonga, S., 2011. Modeling, parameters identification and experimental validation of composite materials behavior law used in 700 bar type IV hydrogen high pressure storage vessel. *International Journal Hydrogen Energy*, pp. 456-478.
- Guiheneuf, V., Bouvier, M. & Jean-marie, A., 2018. Modeling and simulation of a composite high pressure vessel made of sustainable and renewable alternative fibers. *International Journal of Hydrogen Energy*, pp. 970-978.
- Hannus, S. & Majak, J., 2003. Orientational design of anisotropic materials using the Hill and Tsai-Wu strength criteria. *Mechanics of composite Materials*, Volume 39, pp. 6-28.
- Hashin, Z., 1980. Failure criteria for unidirectional fiber composite. *Journal of Applied Mechanics*, pp. 329-334.
- Hendlmeier, A; Marinovic, L; Al-Assafi, S; Stojcevski, F; Henderson, L C, 2019. Sizing effects on the interfacial shear strength of a carbon fiber reinforced two-componet thermoplastic polymer. *Composites Part A: Applied Science and Manufacturing*, p. 127-134
- Hereil, P. L., Mespoulet, J. & Plassard, F., 2015. Hypervelocity impact of aluminum projectiles against pressurized alumunum-composite vessel. *Procedia Engineering*, Volume 103, pp. 181-188.
- Kamal, K., Sayed,T. & Elbutch,A., 2016. Analytical and finite element modelling of pressure vessel for seawater reverse osmosis desalination plant. *Desalination*, Volume 397, pp. 126-139.
- Mian, H. H., Wang, G. & Dar, U. A., 2013. Optimization of composite material system and lay-up to achieve minimum weight pressure vessel. *Application of Composite Mater*, pp. 873-889.

Nohan, R. & Yaprakpragada, R., 2000. Composite Pressure Vessel. *Research in Engineering and Technology*, pp. 2-18.

Sonnen, M., Laval, C. & Seifert, A., 2004. Computerized calculation of composite laminates and structures. *Theory and Reality Material*, pp. 56-67.

Taghavian, S. H., Zabihpoor, M. & Jam, J. E., 2010. Developemnt of new method for design of stiffened composite pressue vessel using lattice structures,. *science of engineering composite mater*, pp. 175-182.

Appendix

Appendix A: Equations used in study

1 Derivation of stainless steel thickness from Von-Mises theorem.

Form the x and y axis the stress of the axial and hoop nature is as follow:

$$\sigma_x = \frac{PD_i}{4h}$$

$$\sigma_y = \frac{PD_i}{2h}$$

From use of von-Mises formula for pressure vessel made of stainless steel given as follow:

$$\sigma_{max}^2 + \sigma_{min}^2 - \sigma_{max}\sigma_{min} = \left(\frac{Syt}{S}\right)^2$$

The σ_{max} and σ_{min} are principal stress generated form the axial and hoop stress as below

$$\sigma_{max} = \frac{\sigma_x + \sigma_y}{2} + \tau_{max}$$

$$\sigma_{min} = \frac{\sigma_x + \sigma_y}{2} - \tau_{max}$$

$$\tau_{max} = \sqrt{\left(\frac{\sigma_x - \sigma_y}{2}\right)^2 + \tau^2}, \tau=0$$

$$\left(\frac{\sigma_x + \sigma_y}{2} + \frac{\sigma_x - \sigma_y}{2}\right)^2 + \left(\frac{\sigma_x + \sigma_y}{2} - \frac{\sigma_x - \sigma_y}{2}\right)^2 - \left[\left(\frac{\sigma_x + \sigma_y}{2}\right)^2 - \left(\frac{\sigma_x - \sigma_y}{2}\right)^2\right] = \left(\frac{Syt}{S}\right)^2$$

$$\left(\frac{\sigma_x + \sigma_y}{2}\right)^2 + \frac{(\sigma_x + \sigma_y)(\sigma_x - \sigma_y)}{2} + \left(\frac{\sigma_x - \sigma_y}{2}\right)^2 + \left(\frac{\sigma_x + \sigma_y}{2}\right)^2 - \frac{(\sigma_x + \sigma_y)(\sigma_x - \sigma_y)}{2} + \left(\frac{\sigma_x + \sigma_y}{2}\right)^2 - \left(\frac{\sigma_x - \sigma_y}{2}\right)^2 +$$

$$\left(\frac{\sigma_x - \sigma_y}{2}\right)^2 = \left(\frac{Syt}{S}\right)^2$$

$$\left(\frac{\sigma_x + \sigma_y}{2}\right)^2 + 3\left(\frac{\sigma_x - \sigma_y}{2}\right)^2 = \left(\frac{S_{yt}}{S}\right)^2$$

From initial equations the axial and hoop stress can be replaced in the expression above and yield the thickness as follow:

$$\frac{\left(\frac{PD}{4h} + \frac{PD}{2h}\right)^2}{4} + 3\frac{\left(\frac{PD}{4h} - \frac{PD}{2h}\right)^2}{4} = \left(\frac{S_{yt}}{S}\right)^2$$

$$\frac{\left(\frac{PD+2PD}{4h}\right)^2}{4} + 3\frac{\left(\frac{PD-2PD}{4h}\right)^2}{4} = \left(\frac{S_{yt}}{S}\right)^2$$

$$\frac{\left(\frac{3PD}{4h}\right)^2}{4} + 3\frac{\left(\frac{-PD}{4h}\right)^2}{4} = \left(\frac{S_{yt}}{S}\right)^2$$

$$\frac{\frac{9P^2D^2}{4h^2} + \frac{3P^2D^2}{4h^2}}{4} = \left(\frac{S_{yt}}{S}\right)^2$$

$$\frac{12P^2D^2}{64h^2} = \left(\frac{S_{yt}}{S}\right)^2$$

$$\frac{3P^2D^2}{16h^2} = \left(\frac{S_{yt}}{S}\right)^2$$

$$\frac{(\sqrt{3})^2 P^2 D^2}{4^2 h^2} = \left(\frac{S_{yt}}{S}\right)^2$$

$$\frac{\sqrt{3}PD}{4h} = \frac{S_{yt}}{S}$$

$$h = \frac{\sqrt{3}PDS}{4S_{yt}} \quad (\text{Kamal, et al., 2016})$$

Appendix B: Codification analysis of shell thickness


```

Editor - C:\Users\NathanNN\Desktop\New folder\Thickness.m
angle55.m x Trial.m x Angle055.m x Thickness.m x Fiber.m x Untitled3.m x ShellThickness.m
1 - E1=147
2 - E2=10.3
3 - V12=0.27
4 - V21=0.02
5 - Q66=7.2
6 - Q11=E1/(1-(V12*V21))
7 - Q12=V21*E1/(1-(V12*V21))
8 - Q22=E2/(1-(V12*V21))
9 - O1=55
10 - O2=-55
11 - O3=55
12 - O4=-55;
13 - C1=cosd(O1)
14 - S1=sind(O1)
15 - C2=cosd(O2)
16 - S2=sind(O2)
17 - C3=cosd(O3)
18 - S3=sind(O3)
19 - C4=cosd(O4)
20 - S4=sind(O4)

```

```

Editor - C:\Users\NathanNN\Desktop\New folder\Thickness.m
angle55.m x Trial.m x Angle055.m x Thickness.m x Fiber.m x Untitled3.m x ShellThickness.m
21 - Qxx1=(Q11*C1^4)+(Q22*S1^4)+2*(Q12+(2*Q66))*(S1^2)*(C1^2)
22 - Qxx2=(Q11*C2^4)+(Q22*S2^4)+2*(Q12+(2*Q66))*(S2^2)*(C2^2)
23 - Qxx3=(Q11*C3^4)+(Q22*S3^4)+2*(Q12+(2*Q66))*(S3^2)*(C3^2)
24 - Qxx4=(Q11*C4^4)+(Q22*S4^4)+2*(Q12+(2*Q66))*(S4^2)*(C4^2)
25 - Qxy1=((Q11+Q22-(4*Q66))*(S1^2)*(C1^2)+(Q12*((S1^2)+(C1^4)))
26 - Qxy2=((Q11+Q22-(4*Q66))*(S2^2)*(C2^2)+(Q12*((S2^2)+(C2^4)))
27 - Qxy3=((Q11+Q22-(4*Q66))*(S3^2)*(C3^2)+(Q12*((S3^2)+(C3^4)))
28 - Qxy4=((Q11+Q22-(4*Q66))*(S4^2)*(C4^2)+(Q12*((S4^2)+(C4^4)))
29 - Qyy1=(Q11*S1^4)+(Q22*C1^4)+(2*(Q12+(2*Q66))*S1^2*C1^2)
30 - Qyy2=(Q11*S2^4)+(Q22*C2^4)+(2*(Q12+(2*Q66))*S2^2*C2^2)
31 - Qyy3=(Q11*S3^4)+(Q22*C3^4)+(2*(Q12+(2*Q66))*S3^2*C3^2)
32 - Qyy4=(Q11*S4^4)+(Q22*C4^4)+(2*(Q12+(2*Q66))*S4^2*C4^2)
33 - Qxs1=((Q11-Q12-(2*Q66))*C1^3*S1)-((Q22-Q12-(2*Q66))*S1^3*C1)
34 - Qxs2=((Q11-Q12-(2*Q66))*C2^3*S2)-((Q22-Q12-(2*Q66))*S2^3*C2)
35 - Qxs3=((Q11-Q12-(2*Q66))*C3^3*S3)-((Q22-Q12-(2*Q66))*S3^3*C3)
36 - Qxs4=((Q11-Q12-(2*Q66))*C4^3*S4)-((Q22-Q12-(2*Q66))*S4^3*C4)
37 - Qys1=((Q11-Q12-(2*Q66))*S1^3*C1)-((Q22-Q12-(2*Q66))*C1^3*S1)
38 - Qys2=((Q11-Q12-(2*Q66))*S2^3*C2)-((Q22-Q12-(2*Q66))*C2^3*S2)
39 - Qys3=((Q11-Q12-(2*Q66))*S3^3*C3)-((Q22-Q12-(2*Q66))*C3^3*S3)
40 - Qys4=((Q11-Q12-(2*Q66))*S4^3*C4)-((Q22-Q12-(2*Q66))*C4^3*S4)
41 - Qss1=((Q11+Q22-(2*Q12)-(2*Q66))*S1^2*C1^2)+(Q66*(S1^4+C1^4))
42 - Qss2=((Q11+Q22-(2*Q12)-(2*Q66))*S2^2*C2^2)+(Q66*(S2^4+C2^4))
43 - Qss3=((Q11+Q22-(2*Q12)-(2*Q66))*S3^2*C3^2)+(Q66*(S3^4+C3^4))
44 - Qss4=((Q11+Q22-(2*Q12)-(2*Q66))*S4^2*C4^2)+(Q66*(S4^4+C4^4))
45 - xy1=[Qxx1 Qxy1 Qxs1;Qxy1 Qyy1 Qys1;Qxs1 Qys1 Qss1]
46 - xv2=[Qxx2 Qxy2 Qxs2;Qxy2 Qyy2 Qys2;Qxs2 Qys2 Qss2]

```

```

Editor - C:\Users\NathanNN\Desktop\New folder\Thickness.m
angle55.m x Trial.m x Angle055.m x Thickness.m x Fiber.m x Untitled3.m x ShellThickness.m x weight.m x Hoop.m x
49 - h=0.00335
50 - h1=0
51 - h2=h/4
52 - h3=h2*3
53 - h4=h2*4
54 - h5=h
55 - A=((xy1*(h2-h1))+(xy2*(h3-h2))+(xy3*(h4-h3))+(xy4*(h5-h4)))*10^9
56 - B=1/2*10^9*(xy1*((h2)^2-(h1)^2))+(xy2*((h3)^2-(h2)^2))+(xy3*((h4)^2-(h3)^2))+(xy4*((h5)^2-(h4)^2))
57 - D=1/3*10^9*(xy1*((h2)^3-(h1)^3))+(xy2*((h3)^3-(h2)^3))+(xy3*((h4)^3-(h3)^3))+(xy4*((h5)^3-(h4)^3))
58 - d=inv(D-(B*(inv(A))*B))
59 - a=(inv(A))-((-inv(A))*B)*d*(B*(inv(A)))
60 - b=(-inv(A))*B*d
61 - c=-d*(B*(inv(A)))
62 - p=8*10^6
63 - Di=0.2067
64 - Nx=p*Di/4
65 - Ny=p*Di/2
66 - Ns=0
67 - Mx=0
68 - My=0
69 - Ms=0;
70 - Nxy=[Nx;Ny;Ns]
71 - Mxy=[Mx;My;Ms]
72 - exy=(a*Nxy)+(b*Mxy)
73 - kxy=(c*Nxy)+(d*Mxy)
74 - Z=h/2

```

```

Editor - C:\Users\NathanNN\Desktop\New folder\Thickness.m
angle55.m x Trial.m x Angle055.m x Thickness.m x Fiber.m x Untitled3.m x ShellThickness.m x weight.m x
75 - Exy=exy+(Z*kxy)
76 - T=[C2^2 S2^2 (2*C2*S2);S2^2 C2^2 (-2*C2*S2);(-C2*S2) (C2*S2) (C2^2-S2^2)]
77 - E12=T*Exy
78 - Q=[Q11 Q12 0;Q12 Q22 0;0 0 Q66]*10^9
79 - G12=Q*E12
80 - F1t=2280*10^6
81 - F2t=57*10^6
82 - F6=71*10^6
83 - F1c=1440*10^6
84 - F2c=228*10^6
85 - f1=(1/F1t)-(1/F1c)
86 - f2=(1/F2t)-(1/F2c)
87 - f11=1/(F1t*F1c)
88 - f22=1/(F2t*F2c)
89 - f66=1/(F6^2)
90 - f12=-sqrt(f11*f22)/2
91 - G1=G12(1,1)
92 - G2=G12(2,1)
93 - t6=G12(3,1)
94 - AA=(f11*G1^2)+(f22*G2^2)+(f66*t6^2)+(2*f12*G1*G2)
95 - BB=(f1*G1)+(f2*G2)
96 - S=(-BB+(sqrt(BB^2+(4*AA))))/(2*AA)
97 - Sf=2
98 - ha=Sf*0.002/S
99
100

```

Hybrid Modulation Scheme for System Performance Evaluation and Energy Efficiency Measurement in 5G Technology

Bertille Auyane Ngouessy ep Ovono¹, Temidayo Otunniyi², Marcel O Odhiambo³

Faculty of Engineering, Vaal University of Technology, Gauteng, South Africa

¹bertie.ovono@gmail.com, ²temidayoo@vut.ac.za, ³ohanga.marcel@mut.ac.za

Abstract

The alarming growing rates of data traffic in mobile communication systems demand high utilization of high spectrum bands. This expected tremendous increase of mobile traffic from 5G technology has an impact on power consumption. Because of the problem of energy consumption in 5G, many multicarrier modulation schemes are being studied as a part of the 5G physical layer solution to meet the requirement of 5G which aims for low latency and complexity. However, the multicarrier suffers from a high peak to average power ratio which affects the energy efficiency. In this paper, a hybrid modulation scheme called Spatial Modulation Orthogonal Frequency Division Multiplexing Access (SM-CE-OFDMA) based on constant-envelope is suggested. This proposed approach compared the components of the hybrid by examining the performance evaluation parameters such as peak-to-average power ratio (PAPR), signal-to-noise ratio (SNR), and bit error rate (BER). According to the parameters mentioned, a high PAPR affects energy efficiency. The simulation results showed that the SM-CE-OFDMA outperformed the conventional OFDMA and CE-OFDMA in terms of BER performance. The results showed that CE-OFDMA has lower PAPR than conventional OFDMA and almost similar amount with SM-CE-OFDMA. So, with SM-CE-OFDMA significantly reduce PAPR. Hence, the simulation results showed that simulated BER of SM-CE-OFDMA decreased as the SNR increased, consequently the energy efficiency also increased. Therefore, SM-CE-OFDMA indicated improved energy efficiency compared to conventional CE-OFDMA with the PAPR of about 0.04dB. It was found that MATLAB simulation results demonstrated that the hybrid SM-CE-OFDMA could achieve good performance and energy efficiency in 5G wireless communication.

Keywords—5G technology; PAPR, SNR, BER, Energy Efficiency, Hybrid modulation scheme, Constant Envelope, Spatial Modulation Orthogonal Frequency Division Multiplexing Access.

1. INTRODUCTION

The alarming growing rates of data traffic in mobile communication system demand high utilization of high spectrum band. This expected tremendous increase of mobile traffic from 5G technology has an impact on energy efficiency. Since, many users are involved in the spectrum demand; multicarrier modulation schemes such as OFDMA are being explored [1].

The OFDMA based on OFDM is a higher order modulation scheme used in the air interface stage of 5G New Radio (5G NR), which allows for mobile connectivity [2]. OFDMA consists of dividing the entire frequency spectrum into several sub-bands consisting of a set of orthogonal subcarriers. Then each team of subcarrier is allotted to individual node for transmission simultaneously [2]. However, for conceptualizing the OFDMA system is a challenge. The main issue is for lessening the peak to average power ratio (PAPR). The PAPR problem requires a linear PA operation that is less energy efficient than a saturated or Type-C operation. Energy efficiency is a critical communication design parameter that affects output transmit power and therefore detection sensitivity. So, for the efficiency of the system PAPR has to be reduced [3].

The high peak to average power (PAPR) defined as the ratio between the maximum power of the signal and its average power is the major drawback in multicarrier. modulation schemes. This PAPR. The PAPR is mathematically expression as follows in Equation (1):

$$PAPR = \frac{\max |x[t]|^2}{\frac{1}{N_c} \sum_{n=0}^{N_c-1} |x[t]|^2} \quad (1)$$

Where the time samples of an OFDM symbol are represented by the values $x[t]$, $n = 0, \dots, N_c - 1$.

$$PAPR(dB) = 10 \log_{10} PAPR$$

The crest factor (CF), which is $CF = PAPR$, is another measure for determining envelope variation and is appressed as:

$$CF = \sqrt{PAPR} \quad (2)$$

To reduce the PAPR, a constant envelope is introduced. Constant envelope signals are suitable for wireless applications because they are less distorted in high power amplifiers [4]. Consequently, amplifier changes the amplitude of the signal. Increasing the power of a signal means increasing its amplitude. Non-linear amplifiers change the amplitude of a signal by varying the amount according to the momentary amplitude of the signal. As the amplitude of the signal changes, non-linear amplification occurs and the signal is distorted [5].

Various constant envelope Techniques have been widely suggested in the literature.

2. RELATED WORK

Several researchers have worked on multicarrier schemes to overcome the PAPR issue.

In [6,7] the information-carrying message signal is converted into a constant envelope waveform using phase modulation.

In [8] the authors debated on OFDM waveform used to phase modulate the carrier in CE-OFDM.

In [9] the authors made use of CE-OFDM to reduce the blanking errors due to PAPR associate to OFDM.

In [10] CE-OFDM associate with blanking tool outperform the OFDM-based system in terms of the blanking error probability. In addition, it showed that the proposed system could achieve a gain in output SNR of up to 6 dB relative to the traditional OFDM scheme.

In [11] Uludag investigated on CE- OFDM and SC-FDMA under AWGN, Rayleigh Fading, and Ricean Fading channels in the purpose of increasing the capacity in 5G, however, 5G was not yet explored. In this wireless communication system only 4 users were taken. This approach was found not to be so effective if the number of users increased. So, based on Uludag's future requirement work. This is what motivated the introduction of this work base on spatial modulation.

Spatial modulation is a modulation schemes uses to offer low system complexity, improve data rate and better error performance in correlated channel environments. It also exploits properties of randomness and uniqueness of the wireless communication channel [12]. It combines with OFDMA easily due to the fact that OFDMA seamlessly incorporates another rate boosting technology so called Multiple-Input Multiple-Output (MIMO) since spatial modulation is an advanced MIMO. SM has the propriety to reduce inter-carrier interferences (ICI) in OFDMA while maintaining the high spectral efficiency in both. Hybridizing both SM and OFDMA which allows to efficiently use the advantages presented in both modulation which are to improve transmission speed while keeping low complexity. SM-OFDMA is a 3D (Three- dimension) through which the data can be encoded and decoded and utilizes indices transmitting antennas and active subcarriers. This modulation scheme at the receiver has the ability to eliminates synchronization between transmitting antenna and inter-channel interference while maintaining the spectral efficiency when applied on OFDMA transmission. The Spatial modulation divides the block information bitstream into two transmissions components, a unique antenna number selected from a set of symbols and transmitting antennas selected from the signal constellation diagram [13].

3. PROPOSED HYBRID MODULATION SCHEME

For the purpose of this study, it is suggested that the spatial modulation be combined CE- OFDMA. The transceivers block diagram of the simulated of the proposed hybrid are respectively shown in Figure 1 and Figure 2.

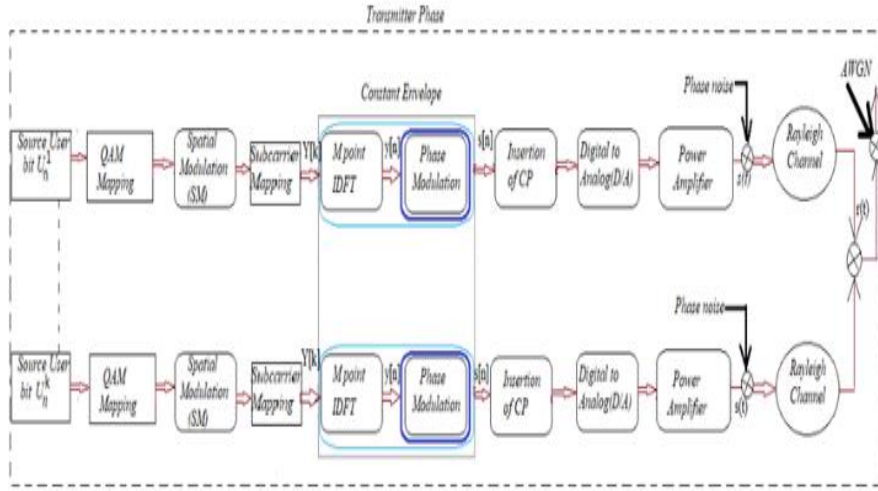


Figure 19: SM-CEOFDMA Transmitter Block diagram

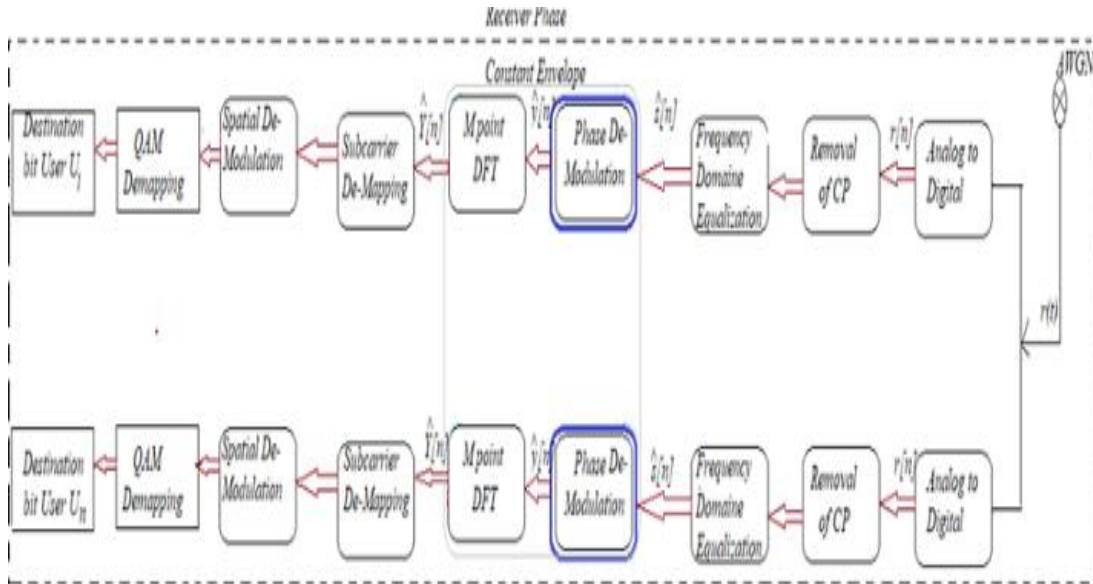


Figure 2: SM-CE-OFDMA Receiver Block diagram

Spatial modulation (SM) was applied to CE-OFDMA transmission. First, SM was considered with $M_t = 4$ and $M_r = 4$ denoting respectively transmit and receive antennas, in which a selected constellation 16QAM was applied. N_p is the overall number of bitstream data conveyed by the SM transmission of all SM-CE-OFDMA of every symbol. The remaining antennas were deactivated, the total N_p data carried were divided into two T cluster and the selected M bits were sent in every single subcarrier of the transmission by the index of OFDMA modulators.

At the transmitter, each source user bits containing U_n symbols are created separately. The source user bits first go through a chosen constellation precisely quadrature amplitude modulation (QAM), a group of input bits are mapped to spatial modulation where the number of transmit antennas is denoted M_t and M_r symbolizing the number of receive antennas. In SM only one enabled transmitter antenna is used at any

signaling time instance for data transmission. The spatial and signal constellation diagram, each one of them carry their own set information. The spatial constellation diagram has the same length as the number of N_t transmit antenna, whereas the signal constellation diagram has a size indicated by M . The input block size of η_{si} bits is partitioned, wherein $\eta_{si} = \log_2 M_t M$ being the number of bits consistent with the image. Each block is divided into components of $\log_2 N_t$ bits and $\log_2 M$ bits. The primary phase turns on, one of the transmit antennas denoted by N_{tiv} . The residual bits are utilised to decide a symbol inside signal constellation diagram, and the dynamic receive antennas pass on this symbol that is denoted by the mean of $x_l, l = 1, 2, \dots, M$. The send signal is expressed via a vector $X_{tiv,l} = [x_1, x_2, \dots, x_{N_t}]^T$, of which the t_{tiv}^{th} element incorporates x_l while others receive no power meaning they are assigned zero. After spatial modulation the user data block with N symbols of block $\mathbf{X} = [X_0, X_2, \dots, X_{N-1}]^T$ is routed through subcarrier mapping block for each user of M accessible subcarriers. The rate of SM system is given by:

$$R_{SM} = \log_2(N_t M) \quad (3)$$

with $N_t = 4$ and $M = 4$ Then the symbols are mapped to $M(M > N)$ orthogonal subcarriers and converted to a time domain complex signal sequence using an M -point Inverse Discrete Fourier Transform (IDFT), which is mathematically represented by Equation (4).

$$x[n] = \sum_{k=0}^{N_{dft}-1} X(k) e^{\frac{j2\pi nk}{N_{dft}}} \quad n = 0, 1, \dots, N_{dft} - 1 \quad (4)$$

$X(k)$ is the complex containing the frequency spectrum DFT, while the discrete and periodic k runs from 0 to $N-1$, and $k = 0$ to $N/2$. The block diagram shows that IDFT precede the phase modulation block and these two blocks makes the constant envelope. Table 1: 4 x 4 Spatial modulation scheme mapping matrix illustrates the mapping of the suggested approach.

Table 1: 4 x 4 Spatial modulation scheme mapping matrix

4 x 4 Spatial modulation mapping with $N_t=4, M=4$		
Source Bits symbols	Antenna number	Transmit
0000	T_x1	$3+3j$
0001	T_x1	$1+3j$
0010	T_x1	$-3+3j$
0011	T_x1	$-1+3j$
0100	T_x2	$3+j$
0101	T_x2	$1+j$

0110	T_x2	-3+j
0111	T_x2	-1+j
1000	T_x3	3-3j
1001	T_x3	1-3j
1010	T_x3	-3-3j
1011	T_x3	-1-3j
1100	T_x4	3+j
1101	T_x4	1-j
1110	T_x4	-3-j
1111	T_x4	-1-j

The peak to average power ratio (PAPR) for various spreading codes can be limited by:

For the uplink by the Equation (5)

$$PAPR \leq \frac{2 \max_{l=L} \left\{ \sum_{l=0}^{L-1} c_l^{(k)} e^{\frac{j2\pi l t}{T_s}} \right\}}{l=L} \quad (5)$$

Where L denotes the oversampling factor, which determines the maximum number of active users K and the chip rate of the serial spreading code $c_l^{(k)} = e^{-j2\pi l k/L}$

At the receiver shown in Figure 2 is made up of NRF chains that perform frequency domain equalization on the analog to digital baseband signal after the cyclic prefix is removed. The frequency domain equalization ((FDE)signal is then fed into the phase modulator, which is made up of the arctangent calculator, if present, a phase unwrapped. The unwrapped may avoid the phase unwrapped associated with arctangent calculation. Its use, however, is not always recommended. The un-wrapper addresses the wrapping issues just for high signal-to-noise ratio (SNR) values, while, for low SNR, phase unwrapping error may cause execution corruption.

At the receiver signal, the baseband is given by Equation (6).

$$\begin{aligned} r(t) &= \int_0^{\tau_{max}} h(\tau, t) s(-\tau + t) d\tau + w(t) \\ &= \int_0^{\tau_{max}} h(\tau) s[(t - \tau)] d\tau + w(t) \end{aligned} \quad (6)$$

Where the channel impulse response is represented by $h(\tau, t)$ with its maximum propagation delay τ_{max} while $w(t)$ symbolises the complex valued Gaussian noise. Assuming that the channel is static over the block interval $T_{scp} \leq t < T$, therefore $h(\tau, t) \approx h(\tau)$. After the constant envelope block, the insertion of the cycle prefix (CP) makes the linear convolution with the circular convolution equivalent to the channel impulse response. Thus, by selecting $N_{scp} \geq L$, the receive samples $r(n)$ obtained after the signal has passed through the analog to digital converter are equivalently represented by linear (*) or circular convolution (*), Where L is the length of channel impulse response.

$$r(n) = s_n * h_n + w_n, \quad n = -N_{scp}, \dots, N_{dft-1} \text{ step1} = s_n \otimes h_n + w_n, \quad n = 0, \dots, N_{dft-1} \text{ step2} \quad (7)$$

step1 in equation (7) denotes the linear convolution between the transmitted signal samples and channel. While *step2* in equation (7) represents the circular convolution.

Here w_n denotes the complex zero mean White Gaussian Noise process. Since w_n is white, it is a fixed irregular cycle with a level power spectral density (PSD) at all frequencies. It is customary to assume its PSD as: $\frac{N_0}{2} \quad -\infty < f < \infty$.

Due to that the power of the white process is limitless and the hypothesis of Wiener-Khinchine states that the autocorrelation function of the AWGN is:

$$R(\tau) \triangleq E\{(w_n)w_n(t-\tau)\} = \int_{-\infty}^{\infty} N(f)e^{j2\pi f\tau}df = \int_{-\infty}^{\infty} \frac{N_0}{2} e^{j2\pi f\tau}df = \frac{N_0}{2} \delta(\tau) \quad (8)$$

Where $\delta(\tau)$ denotes the Dirac delta function. In equation (9) $\{[S_n, H_n]\}$ represent the discrete Fourier transforms of $\{[s_n, h_n]\}$. After analog to digital converter, the cyclic prefix removal process is done, and the frequency domain equalization equalizes the residual samples.

This frequency domain equalization \hat{s}_n flip-flops the channel effect perfectly and its output is given by the Equation (9):

$$\hat{s}_n = IDFT\{R_k C_k\} = s_n \otimes C_n \quad (9)$$

Where C_k is the equalizer correction term which helps reducing ISI and the effect of the noise addition in the system, and is calculated cordially to the kind of FDE, while s_n is the received signal; the improving of the constant associate to the equalizer while using minimum mean square error (MMSE) equalizer a mathematical Equation (10) is derived as follows:

$$C_k = \frac{H_k^*}{|H_k|^2 + \frac{1}{SNR}} \quad (10)$$

Where the signal to noise ratio is denoted SNR. Succeeding by the application of the time domain on the phase demodulator which is composed of the finite impulse filter. The finite impulse filter is utilized for the enhancement the performance of phase demodulator, the usage of arctangent $\arg(\cdot)$ is for the withdrawal of the signal's phase.

4. SIMULATION AND DISCUSSION OF RESULTS

Peak to average power has always been a major problem in multicarrier modulation single or hybridized. So, it is advisable that these techniques be correctly modelled. The flow chart of the prototype simulation is shown in Figure 3 and Table 2 define parameters were used for to develop SM-CE-OFDMA.

Table 2: Parameters of the simulation

<i>Specification</i>	<i>Parameters</i>
System channel	Uplink physical channel
System bandwidth	5MHz
Modulation Scheme	16QAM
CP	170
Input block size	63
Transmitter IDFT size	512
Subcarrier spacing	15KHz
OFDMA input block size	64 symbols
Noise environment	AWGN
Receiver	MMSE
Frequency Band	450 MHz -6GHz
Spatial modulation configuration	4 x 4
Oversampling	5
Total active users	25

For a total number of 60000 transmitted bits the following performance metrics that were employed:

- (i) Bit Error Rate (BER)
- (ii) Signal to Noise Ratio (SNR)
- (iii) Peak to average power ratio
- (iv) Power spectral density (PSD)

The bit error rate is the ratio of error bits to the total number of bits sent during the time interval.

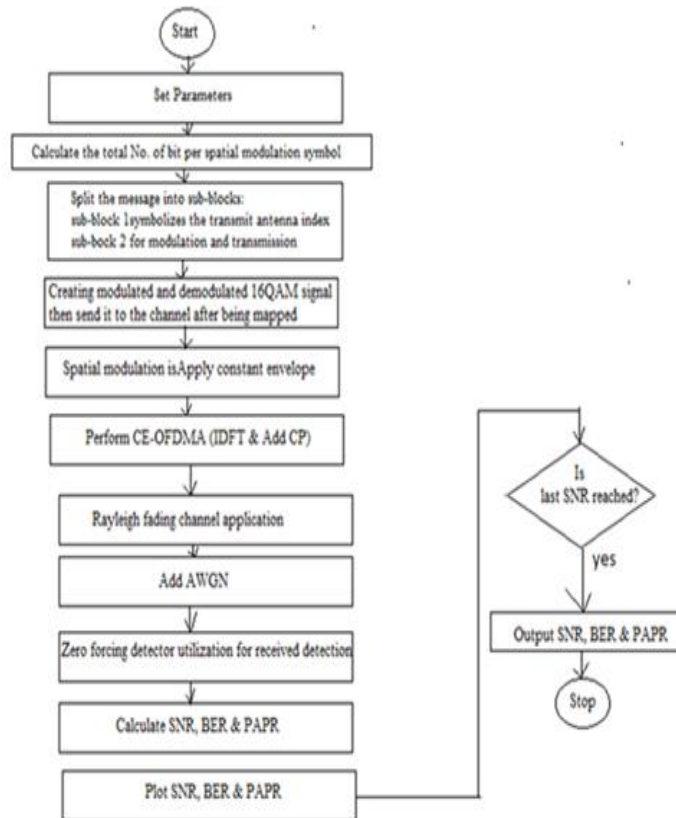


Figure 3: Proposed hybrid flowchart

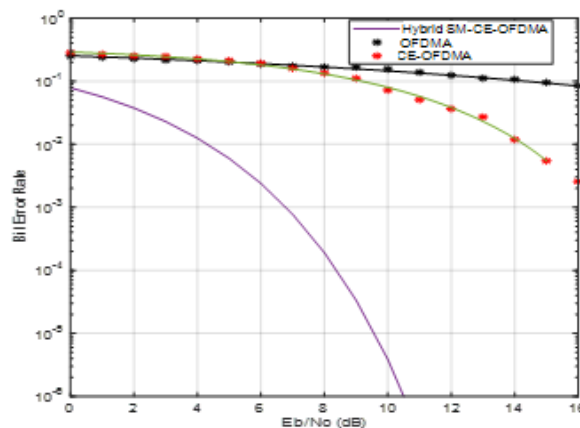


Figure 4: Bit Error Rate vs Eb/No

4.1. Bit error rate and Signal to noise ratio

BER = error bit / number of transmission bits. This BER was used to evaluate the performance of the proposed prototype during data transmission.

The signal-to-noise ratio (SNR) is the decibel ratio of the received signal strength to the noise level and an important parameter for wireless communication. This is related to signal quality and system performance.

When the signal level is significantly higher than the noise level then it achieved a reliable connection. This metrics is measured before the prototype is modulated. For the addition of noise in a corresponding modulated signal E_b/N_0 was converted to SNR.

To analyze the performance of the prototype the bit error rate vs signal to noise ratio were used as shown in Figure 4 and Table 3 for OFDMA, CE-OFDMA and SM-CE-OFDMA by comparing transmitter signal with receiver signal. From Table 3 the observations are made on specific values of SNR.

Table 3: BER vs E_b/N_0

	<i>Hybrid SM- CE- OFDMA(4x4)</i>	<i>OFDMA</i>	<i>CEOFDMA</i>
E_b/N_0 Values (dB)	BER	BER	BER
0	0.095	0.4	0.418
1	0.086	0.3955	0.41
2	0.040	0.395	0.4
3	0.020	0.383	0.398
4	0.009	0.387	0.388
5	0.010	0.361	0.354
6	0.0040	0.342	0.301
7	0.0005	0.33	0.231
8	0.0003	0.261	0.196
9	5.5E-5	0.231	0.150
10	5.5E-6	0.201	0.110
11	-	0.162	0.081
12	-	0.135	0.055
13	-	0.123	0.0195
14	-	0.1	0.009
15	-	0.094	0.0017
16	-	0.094	0.00094

At SNR = 0 dB, the BER value of hybrid SM-CE-OFDMA is about 0.095 while OFDMA and CE-OFDMA give respectively 0.4 and 0.418 value of BER.

At SNR = 1 dB, the BER of hybrid SM-CE-OFDMA is equal to 0.086 while OFDMA and CE-OFDMA respectively have 0.3955 and 0.418.

At SNR = 2 dB, the BER of hybrid SM-CE-OFDMA is equal 0.04 while OFDMA and CE-OFDMA respectively have 0.453 and 0.41.

At SNR = 3 dB, hybrid SM-CE-OFDMA has a BER value of 0.020 and for the same SNR the BER of OFDMA is 0.383 while the BER value of CE-OFDMA is 0.398

At SNR = 4 dB, the BER value of hybrid SM-CE-OFDMA is about 0.009 while OFDMA and CE-OFDMA respectively have the BER equal to 0.387 and 0.388.

At SNR = 5 dB, hybrid SM-CE-OFDMA has a BER value of 0.015 while the BER of OFDMA and CE-OFDMA respectively are 0.361 and 0.354.

At SNR = 6 dB, the BER value of hybrid SM-CE-OFDMA is about 0.004 while OFDMA and prototype CE-OFDMA give respectively 0.342 and 0.301 at the same SNR.

At SNR = 7 dB, hybrid SM-CE-OFDMA has a BER value of 0.0005 while the BER of OFDMA and CE-OFDMA respectively are 0.33 and 0.231.

At SNR = 8 dB, hybrid SM-CE-OFDMA has a BER value of 0.0003 and for the same SNR the BER of OFDMA is 0.261 while the BER value of CE-OFDMA is 0.196.

At SNR = 9 dB, the BER value of hybrid SM-CE-OFDMA is about 5.5×10^{-5} while OFDMA and CE-OFDMA give respectively 0.231 and 0.151 at the same SNR.

At SNR = 10 dB, hybrid SM-CE-OFDMA has a BER value of 5.5×10^{-6} and for the same SNR the BER of OFDMA is 0.201 while the BER value of CE-OFDMA is 0.110. From SNR = 0 dB to SNR = 10 dB, it was observed that hybrid SM-CE-OFDMA achieve better BER performance compared to OFDMA and CE-OFDMA.

At SNR = 11 dB, the BER value of OFDMA at same SNR is 0.162 and the BER value of CE-OFDMA is 0.081.

At SNR = 12 dB, OFDMA has a BER value of 0.135 and for the same SNR the BER of CE-OFDMA is 0.055.

At SNR = 13 dB, the BER value of OFDMA is about 0.123 while prototype CE-OFDMA gives 0.0195 at the same SNR.

At SNR = 14 dB, OFDMA has a BER value of 0.1 and for the same SNR the BER of CE-OFDMA is 0.009.

At SNR = 15 dB, OFDMA has a BER value of 0.094 and for the same SNR the BER of CE-OFDMA is 0.0017.

At SNR = 16 dB, OFDMA has a BER value of 0.094 and for the same SNR the BER of CE-OFDMA is 0.00094.

From the simulation results of Figure 4 and Table 3, it can be said that if the SNR increases the BER minimized.

Figure 4 and Table 3 respectively plotted BER vs SNR and displayed the performance results of the hybrid SM-CE-OFDMA, CE-OFDMA and OFDMA. Initially the observation made was that the BER of all the schemes compared decreases with the increase in SNR. This observation verifies the inverse relationship that exists between SNR and BER. The performance was evaluated by comparing the BER to SNR, with

low BER indicating a high SNR. Universally SNR denotes the signal quality, whereas BER denotes signal error rate.

Figure 4 and Table 3 showed that hybrid SM-CE-OFDMA outperformed CE-OFDMA and hybrid SM-CE-OFDMA from low SNR scenario when the nonlinear amplifier is utilised because SM-CE-OFDMA suffers from threshold effect. OFDMA has a high PAPR which affects easily its signal by the nonlinear components. A nonlinearly distorted signal loses orthogonality, then introduces errors and degrades system's performance. Note that, it is critical in OFDMA to maintain the linear relationship between message and amplifier of the transmitted signal by using linear class of the type A or AB amplifiers which are inefficient in term of power. Furthermore, spectral leakage occurs. Nonlinearities are caused by the power amplifier (PA) at the transmitter. Power backoff is required to avoid PA distortion of the transmitted signal.

The envelope of CE-OFDMA modulated signals remains constant which the phase is changed by the message signals. Message signals are transmitted in OFDMA by varying the amplitude of the two carriers. Hybrid SM-CE-OFDMA inherits the same properties of CE-OFDMA, so both systems offer many advantages over OFDMA. It was also observed that OFDMA presented almost a flattened performance along the simulation while and hybrid SM-CE-OFDMA displayed better performance. A higher signal-to-noise ratio (SNR) indicated the strength of the signal compared to the noise levels, authorizing higher data rates and fewer packets of retransmission. This results in higher throughputs. Since throughput is an indicator of system performance, the higher the throughput the better the performance.

In terms of PAPR, hybrid SM-CE-OFDMA and CE-OFDMA have an advantage over OFDMA. PAPR for SM-CE-OFDMA is 0 dB. In addition, no power backoff is required; it is set to 0 dB. As a result, unlike OFDMA, CE-OFDMA and hybrid SM-CE-OFDMA are less affected by nonlinearities, allowing the PA to operate at its optimum saturation point. At this point, the average transmit power and efficiency of PA are maximized. Therefore, hybrid SM-CE-OFDMA systems are advantageous for power amplifiers. Thus, it can be said that hybrid SM-CE-OFDMA system that is suitable for power amplifiers. Therefore, the hybrid SM-CE-OFDMA is preferable to OFDMA.

From the results it was observed that the curve of the proposed SM-CE-OFDMA up to 11dB, then from 12dB up to 16 dB the values are out of range, this is due to the modular array of 4x4 utilized. Nevertheless, if the modular arrays increase to 8x8 or 16x16, the transmitted signal strength would likely increase and the signal-to-noise ratio would improve significantly. As a result, a much better performance can be predicted because of the increase in the array size which would further cause the increase in SNR, then large-scale antenna systems (LSAS) are expected to significantly improve wireless communication systems' energy efficiency (EE) and spectrum efficiency (SE). However, many issues remain unresolved

in implementing digital beamforming (BF) structures, including calibration, complexity, and cost. It is important to note that the proposed hybrid did not consider multipath propagation, so no performance trade-offs were observed.

4.2. Peak to Average Power Ratio

A three-fold Figure 5 depicted the PAPR waveform multicarrier hybrid SM-CE-ODMA. It was observed that the first two sections of Figure 5 when added together, displayed multiple constructive and destructive sine waves with lower sinusoids. The upper part of Figure 5 showed that from [0-7], the PAPR appeared to move from negative 0.04 dB to about a positive 0.08 dB, and then at 0.8ms, it reached a peak of about 0.02dB before dropping back to -0.04 dB at 1ms. In the middle part of Figure 5, a high peak was observed at 0.05ms and 1ms of about 0.04dB, while at the interval [0-0.9], the PAPR dropped to 0 dB. Another observation made was that when the top and the middle part were added together, as shown on the bottom part of Figure 4, the PAPR is between 0dB to 0.06dB from [0-1]. From these results, it can be concluded that Figure 5 exhibited almost the same outcomes in all levels by displaying the PAPR values closer to 0 dB. Thus, it showed that the overall PAPR of the hybrid SM-CE-OFDMA allowed the power amplifier to operate near the maximum limits (0 dB). Therefore, the proposed hybrid SM-CE-OFDMA reduced PAPR in 5G technology.

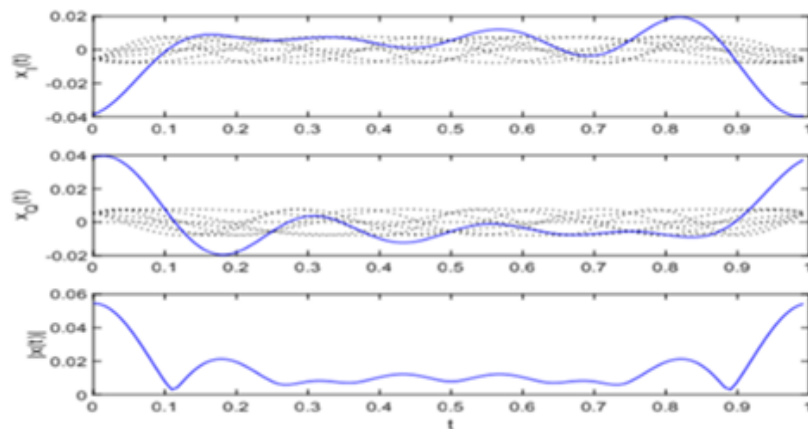


Figure 5: Peak Average Power ratio waveform of SM-CE-OFDMA.

4.3. Power Spectral Density (PSD)

Power spectral density (PSD) is an important function of the power distribution of a signal with respect to frequency. In mobile communications, PSD plays an important role in making the correct radio resource management (RRM) decisions at base stations, especially when it comes to allocating transmission formats, including modulation and bandwidth. If the PSD is unknown at the base station terminal, it may consume more stations, especially when it comes to allocating transmission formats, including modulation and bandwidth. If the PSD is unknown at the base station terminal, it may consume more transmit bandwidth than the maximum user equipment feature. Figure 6 and Figure 7 are periodograms showing

the amount of power that is allocated to each frequency in CE-OFDMA and SM- CE-OFDMA respectively. This power is the power measured before and after the experiments.

Figure 6 shows a periodogram of a normalised peak-to-average power spectrum (in decibels) versus a normalised frequency (in hertz) of measured CE-OFDMA for spectral analysis. From Figure 6 it was also observed that the frequency offered negative and positive values. For a frequency of -2 rad/s, the peak average power was -1,5.dB. Also, for a frequency of -1 rad/s, the average peak power was -0.75 dB. Hence, while Figure 7 showed the normalised peak average power spectrum versus the normalised frequency of the prototype SM-CE-OFDMA when the channels have the same centre frequency band of 4 rad/s, it was observed that the average power of SM-CE-OFDMA was about -2.8 dB at -2 rad/s, and at -1 rad/s, average peak power was about -1.4dB. The simulation results shown in Figure 6 and Figure 7 reveal that the CE-OFDMA symbols have inherently more average power than SM-CE-OFDMA. This result shows the transmit power requirements for the CE-OFDMA and SM-CE-OFDMA symbols described in the previous section of PAPR. Therefore, it was concluded that the proposed hybrid SM-CE-OFDMA is power efficiency.

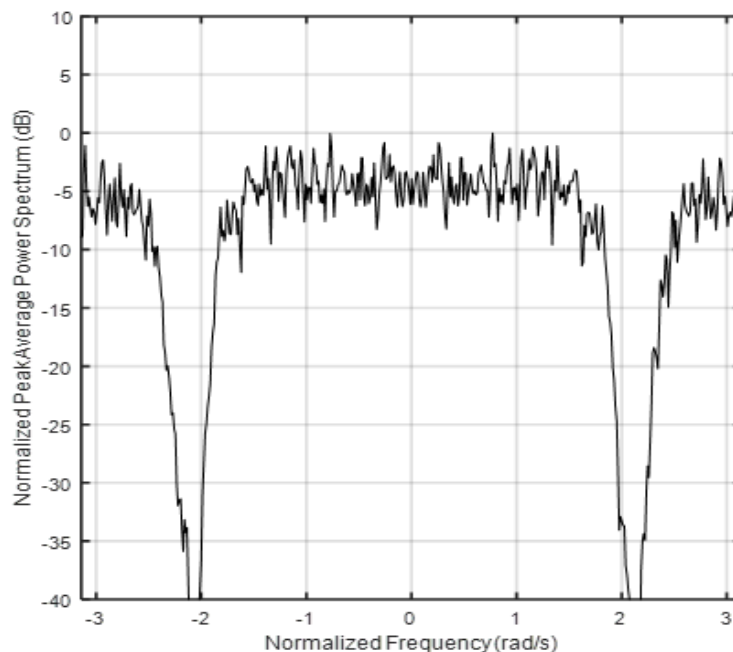


Figure 6: Normalised Peak Average Power Spectrum vs Normalised Frequency of CE-OFDMA

Power spectral density is an important function of the power distribution of a signal with respect to frequency. In mobile communications, PSD plays an important role in making the correct radio resource management (RRM) decisions at base stations, especially when it comes to allocating transmission formats, including modulation and bandwidth.

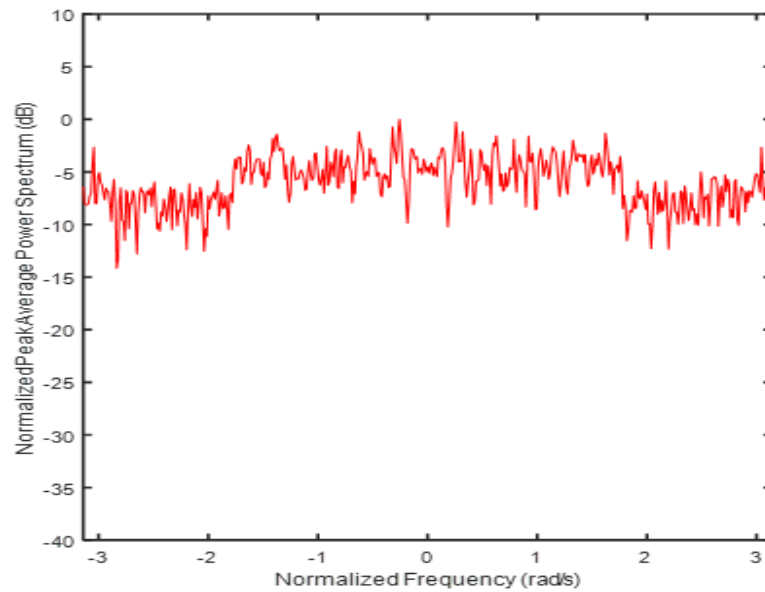


Figure 7: Normalised Peak Average Power Spectrum vs Normalised Frequency of SM-CE-OFDMA

If the PSD is unknown at the base station terminal, it may consume more transmit bandwidth than the maximum user equipment feature. Figure 6 and Figure 7 are periodograms showing the amount of power that is allocated to each frequency in CE-OFDMA and SM- CE-OFDMA respectively. This power is measured before and after the experiments. Figure 6 shows a periodogram of a normalised peak-to-average power spectrum (in decibels) versus a normalised frequency (in hertz) of measured CE-OFDMA for spectral analysis. From Figure 6 it was also observed that the frequency offered negative and positive values. For a frequency of -2 rad/s, the peak average power was - 1,5.dB. Also, for a frequency of -1 rad/s, the average peak power was -0.75 dB. Hence, while Figure 7 showed the normalised peak average power spectrum versus the normalised frequency of the prototype SM-CE-OFDMA when the channels have the same centre frequency band of 4 rad/s, it was observed that the average power of SM-CE-OFDMA was about -2.8 dB at -2 rad/s, and at -1 rad/s, average peak power was about -1.4dB. The simulation results shown in Figure 6 and Figure 7 reveal that the CE-OFDMA symbols have inherently more average power than SM-CE-OFDMA. This result shows the transmit power requirements for the CE-OFDMA and SM-CE-OFDMA symbols described in the previous section of PAPR. Therefore, it was concluded that the proposed hybrid SM-CE-OFDMA is power efficiency.

5. CONCLUSION

The hybrid modulation scheme SM-CEOFDMA was investigated in this work for system performance evaluation and energy efficiency measurement. It was discovered that the SM-CEOFDMA provides better BER. This achieved result was most likely associated with spatial modulation; additionally, its SNR was more efficient and exponentially increased throughout the simulation, demonstrating its reliability of

increasing throughput while decreasing BER. The results showed that increasing SNR significantly increased energy efficiency with very low power transmission. The overall PAPR of the proposed approach SM-CEOFDMA was 0.04dB, indicating that the hybrid modulation scheme increased energy efficiency based on the simulation results. As a result, the proposed scheme outperformed the conventional CE-OFDMA scheme in 5G wireless communication with the PAPR of about 0.04dB while OFDMA and CE-OFDMA respectively have 0.453dB and 0.41dB when SNR= 2dB. Table 3 and Figure 4 illustrate the value comparisons among SM-CEOFDMA, CE-OFDMA, and the standard OFDMA.

REFERENCES

- [1] Jebbar, H., El Hassani, S. and El Abbassi, A., 2018, October. PAPR reduction for 5G waveforms. In 2018 6th international conference on wireless networks and mobile communications (WINCOM) (pp. 1-6). IEEE
- [2] Cisco (2015) Cisco visual networking index: Global mobile data traffic forecast update, 20142019. Cisco, Tech. Rep.
- [3] Zhou, H., Li, B., Yan, Z. and Yang, M., 2017. A channel bonding based QoS-aware OFDMA MAC protocol for the next generation WLAN. *Mobile Networks and Applications*, 22(1), pp.19-29.
- [4] Huang, Y., Hu, S., Ma, S., Luo, Q., Huang, D., Gao, Y. and Shi, R., 2018. Constant envelope OFDM RadCom fusion system. *EURASIP Journal on Wireless Communications and Networking*, 2018(1), pp.1-15.
- [5] Chide, N., Deshmukh, S., Borole, P.B. and Chore, N., 2013. An overview of OFDM variants and their applications. *International Journal of Electronics Communication and Computer Engineering*, 4(2), pp.47-51.
- [6] Balal, Y., Pinchas, M. and Pinhasi, Y., 2016. Constant envelope phase modulation inspired by orthogonal waveforms. *IEEE Communications Letters*, 20(11), pp.2169-2172.
- [7] Thompson, S.C., Ahmed, A.U., Proakis, J.G. and Zeidler, J.R., 2004, October. Constant envelope OFDM phase modulation: spectral containment, signal space properties and performance. In *IEEE MILCOM 2004. Military Communications Conference, 2004.* (Vol. 2, pp. 1129-1135). IEEE.
- [8] Sacchi, C., Cianca, E., Rossi, T. and De Sanctis, M., 2015, June. Analysis and assessment of the effects of phase noise in constant envelope multicarrier satellite transmissions. In *2015 IEEE International Conference on Communications (ICC)* (pp. 922-927). IEEE
- [9] Rabie, K.M., Alsusa, E., Familua, A.D. and Cheng, L., 2015, March. *Constant envelope OFDM*
- [10] transmission over impulsive noise power-line communication channels. In *2015 IEEE International Symposium on Power Line Communications and Its Applications (ISPLC)* (pp. 13-18). IEEE.
- [11] Uludag, E., 2016. Constant-Envelope OFDM and Constant Envelope SC-FDMA (Doctoral dissertation, UC Irvine).
- [12] Agarwal, N., 2019. Spatial Modulation Technique: Achievements and Challenges. In *Computing, Communication and Signal Processing* (pp. 441-448). Springer, Singapore.
- [13] Nusenu, S., 2017. Spatial Modulation Technique For Filtered-OFDM Based Wire-less Transmission. *Advances in Science, Technology and Engineering Systems Journal*, 2, pp.981-986.

Editorial Committee

Name	Category	Country
Eng. Prof. Lawrence Gumbe	Chair	Kenya
Eng. Prof. Leonard Masu	Secretary	Kenya
Eng. Prof. Ayodeji Oluleye	Member	Nigeria
Eng. Dr. Slah Msahli	Member	Tunisia
Eng. Prof. Bernadette W. Sabuni	Member	Kenya
Prof. Anish Kutien	Member	South Africa

Editorial Board

Name	
Chairperson:	Eng. Prof. Lawrence Gumbe
Members:	Eng. Paul Ochola- Secretary
	Eng. Sammy Tangu- Treasurer
	Eng. Erick Ohaga – President, IEK
	Eng. Shammah Kiteme- Honorary Secretary, IEK
	Eng. Prof. Leornard Masu
	Eng. Margaret Ogai
	Eng. Nathaniel Matalanga
	Eng. Dr. Samwel Roy Orenge – Technical Editor

INSTRUCTIONS TO CONTRIBUTORS

The editorial staff of the AJERI requests contributors of articles for publication to observe the following editorial policy and guidelines accessible at <https://www.ikenya.org/> in order to improve communication and to facilitate the editorial process.

Criteria for Article Selection

Priority in the selection of articles for publication is that the articles:

- a. Are written in the English language
- b. Are relevant to the application relevant of engineering and technology research and Innovation
- c. Have not been previously published elsewhere, or, if previously published are supported by a copyright permission
- d. Deals with theoretical, practical and adoptable innovations applicable to engineering and technology
- e. Have a 150 to 250 words abstract, preceding the main body of the article
- f. The abstract should be followed by a list of 4 to 8 "key Words"
- g. Manuscript should be single-spaced under 4,000 words (approximately equivalent to 5-6 pages of A4-size paper)
- h. Are supported by authentic sources, references or bibliography

Rejected/Accepted Articles

- a. As a rule, articles that are not chosen for AJERI publication are not returned unless writer (s) asks for their return and are covered with adequate postage stamps. At the earliest time possible, the writer (s) is advised whether the article is rejected or accepted.
- b. When an article is accepted and requires revision/modification, the details will be indicated in the return reply from the AJERI Editor, in which case such revision/modification must be completed and returned to AJERI within three months from the date of receipt from the Editorial Staff.
- c. Complementary copies: Following the publishing, three successive issues are sent to the author(s)

Procedure for Submission

- a. Articles for publication must be sent to AJERI on the following address:
The Editor
African Journal of Engineering Research and Innovation
P.O Box 41346- 00100
City Square Nairobi Kenya
Tel: +254 (20) 2729326, 0721 729363, (020) 2716922
E-mail: editor@ikenya.org
- b. The article must bear the writer (s) name, title/designation, office/organization, nationality and complete mailing address. In addition, contributors with e-mail addresses are requested to forward the same to the Editor for faster communication.

For any queries, authors are requested to contact by mail (editor@ikenya.org).

PUBLISHER

The Institution of Engineers of Kenya

P.O Box 41346- 00100

City Square Nairobi Kenya

Tel: +254 (20) 2729326, 0721 729363, (020) 2716922

Email: editor@iekenya.org

Website: www.iekenya.org

CONTENTS

Pages

Cost-Effective Telecommunication Technologies for Rural Areas in Developing Countries: A Case Study of South Africa..... **6**

Marcel Ohanga Odhiambo, Weston Mwashita

Optimal Angel and Shell Layers of Overwrapped Composite High-Pressure Vessels: A review of previous studies on composite pressure influenced by angle and shell thickness ... **16**

Nathan Numbi Mukala, Leonard M Masu, Patrick K Nziu

Investigating Effects of Preparation Parameters on Mechanical Performance of PBAC2-co-PM52 Copolyoxamide/Carbon Fiber Reinforced Composites **39**

Fredrick Nzioka Mutua, and Yong He

Optimal shell thickness for Overwrapped Composite High-Pressure Vessels **54**

Nathan Numbi Mukala, Leonard M Masu, Patrick K Nziu

Hybrid Modulation Scheme for System Performance Evaluation and Energy Efficiency Measurement in 5G Technology..... **81**

Bertille Auyane Ngouessy ep Ovono, Temidayo Otunniyi , Marcel O Odhiambo